POLITECNICO DI MILANO

DEPARTMENT OF MECHANICAL ENGINEERING

DOCTORAL PROGRAMME IN MECHANICAL ENGINEERING

SURFACE NANOCRYSTALLIZATION BY SEVERE SHOT PEENING; FROM CONCEPT TO APPLICATION

Doctoral Dissertation of

Seyyed Mostafa Hassani Gangaraj

Supervisor:

Prof. Mario Guagliano

Tutor:

Prof. Roberto Viganò

Coordinator:

Prof. Bianca Maria Colosimo

Year 2013-Cycle XXVI

Dedication

To my lovely family

Acknowledgement

First and foremost I offer my sincerest gratitude to my advisor, **Prof. Mario Guagliano** for his infinite support, valuable advice and continuous encouragement; without which this thesis would not have been completed or written. In fact, I owe my interest in shot peening to his significant contribution to the field as I remember very well when I first became familiar with his work during my master studies. He helped me in different aspects of my life during the years far from home, to smoothly make the cultural transition too. I appreciate **Mario** so much, for encouraging and supporting me to spend almost a year abroad to explore different points of view and learn new perspectives.

I owe my sincere gratitude to **Prof. Christopher A. Schuh**, head of department of material science and engineering at Massachusetts Institute of Technology. It was such a distinct honor to work under his supervision and with his research group during my stay at MIT. I am deeply thankful to **Chris** for his immense knowledge, critical comments and his level of stimulation that made me able to add a novel perspective to my PhD research.

I am deeply thankful to **Eng. Andrea Ghidini** from Lucchini RS S.p.A. for his generous support, sharing ideas and kind-great efforts in specimen preparation and execution of rotating bending fatigue tests. My great appreciation goes to **Eng. Michele Bandini**, for his generous contribution and execution of shot peening in Peen Service srl. I am deeply grateful to **Prof. Marco Boniardi** from department of mechanics at Politecnico di Milano for his generous support and execution of nitriding.

My sincere thank goes to **Dr. Hyon-Jee Lee Voigt** from department of material science and engineering at MIT, for her constant support and friendly advice during my difficult moments. **Hyon-Jee** was such a kind and considerate mentor for me.

Pietro Pellin and **Maurizio Pardi** from Politecnico di Milano deserve special thanks for their help through the XRD measurements, microscopy sample preparations, etc. I would like to extend my acknowledgement to **Dr. Ki Sub Cho** from department of material science and engineering at MIT for his friendly help with TEM observation.

I would like to thank all my friends specially **Dr. Nima Allahverdizadeh** who has been always ready to lend a hand and assist with every type of problems.

The financial support of **Politecnico di Milano** and **Scuola Interpolitecnica** is gratefully acknowledged which gave me the opportunity and encouragement to expand my researches.

I wish I were able to thank my lovely parents **Mohammad** and **Malihe** who loved me with infinite generosity and provided me with the opportunity to be where I am. Without them, none of these would have been even possible. I would like to extend my appreciation to my in-laws **Houshang** and **Maryam** who embraced me into the family and supported me during years.

I would have not been able to get this thesis done if there was not the unyielding support, encouragement, patience, dedication and unwavering love of my wife, **Atieh**. She stood beside me, each single moment throughout these years, as the love of my life, the rock of the family and my best colleague. I owe **Atieh** not only my lovely thanks but also a big scientific thank for her kind assistances, intelligence and critical comments.

Abstract

If one generates a material with high density of defects such that 50% or more of the atoms/molecules are situated in the cores of defect, then this new class of disordered solid would have number of peculiar and outstanding physical, thermal, mechanical and electrical properties. This was the essence of the visionary argument made in late 80s that eventually led to the advent of nanocrystalline (NC) materials. Of fundamentally different properties with respect to the polycrystalline counterpart, high strength, enhanced super-plasticity at lower temperatures and higher strain rates, improved tribological properties and improved fatigue behavior could be mentioned.

Various kind of techniques have been developed to synthesize NC materials such as inert gas condensation, mechanical alloying, electro-deposition, crystallization from amorphous material equal channel angular pressing, high pressure torsion, accumulative roll bonding. Synthesizing ideal 3D NC material, however, comes with 2 major obstacles: It is challenging to produce porosity and contamination free NC material of sufficient size for characterization; Transferring into industrial scale is still an open issue in terms of process cost, sample size and material.

Since most material failures including fatigue fracture, fretting fatigue, wear and corrosion are very sensitive to the structure and properties of materials surface, surface nanocrystallization was proposed to be a convenient alternative to bypass the difficulties of synthesizing buck NC component and yet harvesting the advantages of nanostructures in service. The basic idea used to disclose the concept of mechanically induced surface nanocrystallization is that repeated multidirectional plastic deformation caused by high velocity impacting balls generate defects, interfaces, increase dislocation densities and possibly develop new micro-structure like sub-grains and eventually new grain boundaries.

Surface mechanical attrition (sometimes called ultra-sonic shot peening) has been found to successfully generate surface nanocrystallization on different classes of materials. In spite of pieces of evidence, reported in literature, the knowledge cannot be used yet in order to engineer the surface and design for a given structure. The reason is mainly due to lack of a framework enabling to predict and simulate the process of grain refinement during severe peening. Complexities of the process involving many disciplines of mechanical engineering and material science such as contact mechanics, impact, plasticity, dislocation activation and grain refinement hinder the progress towards a comprehensive numerical framework. Moreover, systematic experimental studies on grain refinement during severe peening are still lacking in the field. The importance of such studies is that they could provide in-depth connection between parameters and the resultant structure.

To address the aforementioned call, a systematic study of surface nanocrystallization by severe shot peening was designed in the present work. Air blast shot peening was applied and adopted as it has more flexibility with respect to surface mechanical attrition to be applied on variety of

components. It is also simpler and less expensive. Different coverage was adopted to span different classes of peening i.e. conventional and severe shot peening. Scanning electron microscopy (SEM) and transmission electron microscopy (TEM) observations were conducted to study the grain size refinement and surface nanocrystallization in all treated specimens, from conventional to severe peening. A numerical framework was also proposed in the present work to simulate all aspects of peening, i.e. surface roughness evolution, generation of compressive residual stress and simulation of grain refinement. The first two have been simulated using finite element method. Experimental measurements of surface roughness and residuals stress were used to verify the strength of the finite element simulation. To simulate grain refinement, nonetheless, a dislocation density model was linked to finite element model. The model in fact uses the output of finite element to simulate different dislocation activities such as generation, migration, annihilation and eventually grain refinement. The comparison of dislocation cell size obtained by numerical framework and those measured by TEM observation shows a satisfactory and promising agreement. The numerical framework is indeed the first of its kind to simulate grain refinement by severe peening.

The second line that is followed by the present research is to affirm and to exploit the benefits of nano-structured surface. It has been well known for a long time that kinetics of diffusion phenomena is highly dependent on time. Gas nitriding, as a well-known thermo-chemical surface treatment to increase surface hardness, is not an exception. A clear beneficial effect of nitriding duration on resultant mechanical characteristics has been reported in the literature. Therefore, prolonging nitriding may seem to be the first alternative to obtain a better functionality. It is accompanied, however, by the high energy cost of processing at high temperature. There is yet another alternative based on the fact that diffusion along nano-sized grains is much more enhanced in comparison with the diffusion through coarse grains. This justifies the idea of combination of severe peening and nitriding. Different combination of peening and nitriding were examined in the present work. The treated specimens were characterized by SEM, residual stress measurement using X-ray diffraction (XRD), micro-hardness tests and surface roughness measurement. The specimens were subjected to rotating bending fatigue tests performed at room temperature in order to evaluate fatigue limit as an important design factor. SEM observations of the fractured surfaces were applied to illustrate the failure mechanism. Based on the results nitriding duration can be successfully reduced without losing improvements in mechanical characteristics and fatigue behavior if a suitable prior severe shot peening is performed.

Contents

List of figures

List of tables

Part I Introduction

1 Nanocrystalline materials

1.1 Introduction

Following the visionary argument made by Gleiter [1], that if metals and alloys are made of nanocrystalline structure they would have number of appealing and outstanding physical, mechanical, thermal and electrical properties, nanocrystalline materials have been the subject of widespread research over the past three decades. Nanocrystalline or nanostructured material is a polycrystalline material with a crystallite size of only a few nanometers. These materials fill the gap between amorphous materials without any long-range order and conventional course-grained materials. While there is no universally agreed upon definition, a common definition in the literature is a crystallite or grain size below 100 nm. At the upper limit of this regime, the term ‘‘ultra-fine grain size’’ is also often used which implies grain size lie in the range of 250–1000. Of their outstanding mechanical properties, one could mention high strength, increased resistance to tribological and environmentally-assisted damage, increasing strength and/or ductility with increasing strain rate, and potential for enhanced superplastic deformation at lower temperatures and faster strain rates [2]. NC materials consist of a large volume fraction of defects, interface boundaries, dislocation and grain boundaries. Figure 1-1 shows a schematic two dimensional depiction of nanostructured materials. The atoms in the centers of the crystals are indicated in black. The ones in the grain boundary core regions, represented by white, are including variety of interatomic spacing and not clearly associated with crystalline symmetry.

In section 1.2 various techniques of synthesizing bulk NC materials are described. These approaches can be generally classified into bottom-up and top-down. In section 1.3 mechanical properties of NC material including strength, ductility, strain rate and temperature sensitivity, fatigue, fracture and tribological properties are discussed.

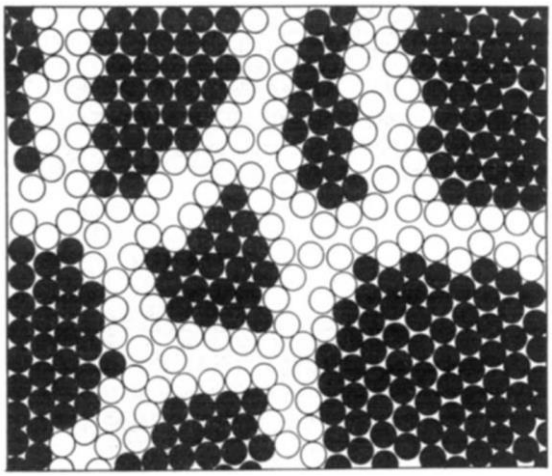

Figure 1-1. Schematic two dimensional depiction of nanostructured materials [1].

1.2 Synthesis

Nanocrystalline materials can be synthesized either by consolidating small clusters or breaking down the polycrystalline bulk material into crystalline units with dimensions of nanometers [3]. These approaches have been classified into bottom-up and top-down. In the bottom-up approach the nanostructure is arranged atom-by-atom, layer-by- layer. In the top-down approach the micro-structure of bulk material is broken down into a nanostructure. The principal synthesis methods are: inert gas condensation, mechanical alloying, electro-deposition, crystallization from amorphous material, severe plastic deformation, cryomilling, plasma synthesis, chemical vapor deposition, pulse electron deposition, sputtering, physical vapor deposition and spark erosion. The five most common methods [3] are described here.

1.2.1 Inert gas condensation

In the inert gas condensation technique [1,4,5], the metal is evaporated inside a chamber using various kinds of heating for instance by resistive heating, radio frequency, heating, sputtering, electron beam heating, laser/plasma heating, or ion sputtering. The chamber is evacuated to a very high vacuum of about 10^7 Torr and then backfilled with a low pressure inert gas like helium. Collision of the evaporated atoms with the gas atoms inside the chamber causes them to lose their kinetic energy and consequently condense in the form of small particles. Convection currents, generated by the heating of the inert gas by the evaporation source and by the cooling of the liquid nitrogen-filled collection device (cold finger) carry the condensed fine powders to the collector device. The deposit is scraped off into a compaction device. Compaction is carried out in two stages: (a) low pressure compacted pellet; (b) high pressure vacuum compaction. The scraping and compaction processes are carried out under ultrahigh vacuum conditions to maintain the cleanliness of the particle surfaces and to minimize the amount of trapped gases. The inert gas condensation method produces equiaxed (3D) crystallites. The crystal size of the powder is typically a few nanometers and the size distribution is narrow. The crystal size is dependent upon the inert gas pressure, the evaporation rate, and the gas composition. Extremely fine particles can be produced by decreasing either the gas pressure in the chamber or the evaporation rate and by using light rather than heavy inert gases (such as Xe). A great deal of the early work on mechanical properties of nanocrystalline materials used the inert gas condensation technique. However, Material prepared with IGC showed a large possibility of contamination and porosity due to insufficient consolidation. Moreover, the manufacturing output was rather small despite relatively high costs of the preparation equipment. There is also the possibility of imperfect bonding between particles, since most of the early work used cold consolidation.

1.2.2 Mechanical alloying

Mechanical alloying is a solid state powder processing technique involving repeated welding, fracturing and re-welding of powder particles in a high energy ball mill. The process has shown to be capable of synthesizing a variety of equilibrium and non-equilibrium alloy phases by grinding of a blended elemental or pre-alloyed powders in devices such as attrition mills, shaker mills and ball mills [6]. Mechanical alloying is accomplished by entrapping and severely deforming the powders between colliding balls or ball and vial; and as a result continuously refining their microstructure to nano scale. Figure 1-2 illustrate a schematic entrapment of the powders between the two colliding balls.

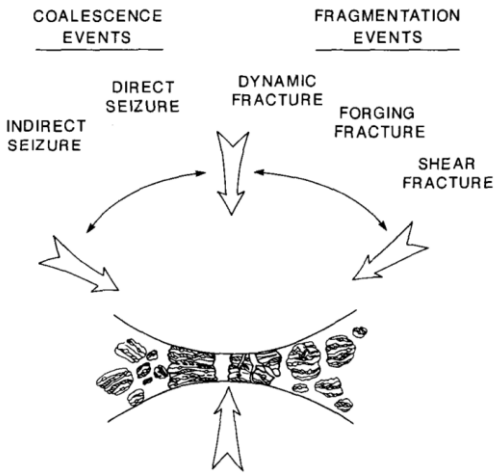

Figure 1-2. Schematic entrapment of the powders between the two colliding balls during mechanical alloying [6].

Nanostructured powder can be obtained in almost any material after sufficient time of milling. Figure 1-3 shows the reduction of grain size with increasing milling for Al, Ni, and Pd powders [7]. Ball milling was performed in a standard laboratory shaker mill (Spex 8000) using hardened steel balls and vial. In the early stages of milling the crystal size decreases rapidly to less than 30 nm for all elements. Further refinement proceeds slowly, and the grain size finally reaches a steady-state value of about 22 nm for Al, 12 nm for Ni, and 7 nm for Pd after 32, 24, and 20 h of milling, respectively. The refinement of the microstructure during ball milling is qualitatively the same for all the elements investigated. Only the final average grain size varies from element to element. The ultimate grain size is inversely proportional with the melting point or the bulk modulus of the specific element whereas the grain size can be reduced to only 22 nm for Al, it decreases to sizes below 10 nm for elements with high melting temperatures or bulk moduli.

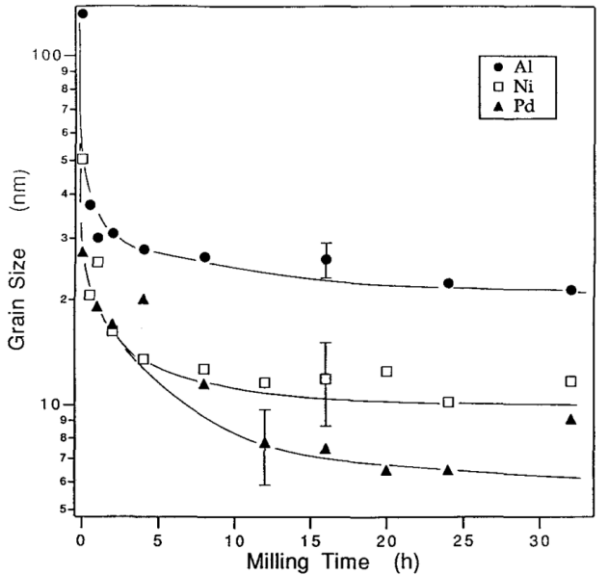

Figure 1-3. Grain size reduction with increasing milling for Al, Ni, and Pd powders [7].

1.2.3 Electro-deposition

Figure 1-4 shows schematically the pulse electrodeposition sequence. As the current spikes, the metal cations are deposited in crystalline and amorphous patches. Figure 1-4 b shows the TEM micrograph of pulse electrodeposited Ni sample. Commercially synthesized (Integran) 5 mm thick plates are available in a range of compositions. Electrodeposition yields grain sizes in the nano-scale when the processing parameters are chosen such that nucleation of new grains is favored rather than growth of existing grains. This could be achieved by using high deposition rates, formation of appropriate complexes in bath, addition of suitable surface active elements to reduce surface diffusion of ad-atoms, etc. This technique can yield porosity-free finished products that do not require subsequent consolidation processing[3].

An electrodeposited Cu sample with a high density of nano-scale growth twins shows an ultrahigh tensile strength, on the order of 1 GPa with a considerable plastic strain, more than 13% [8]. Both the strength and the ductility increase with a decreasing twin lamellae thickness. Post-indentation analyses of electrodeposited indented Cu with nano-scale twins in the transmission electron microscope revealed deformation induced displacement of coherent twin boundaries (CTBs), formation of steps and jogs along CTBs, and blockage of dislocations at CTBs. These processes appear to significantly influence the evolution of thermal activation volume for plastic flow which is some three orders of magnitude smaller than that known for microcrystalline Cu. As a result of the unique properties observed on electrodeposited nanocrystals [9], a number of industrial applications are emerging, For instance, the combination of increased hardness/wear resistance and reduced localized corrosion results in improved protective coating performance. The magnetic and electrical properties make them attractive as

soft magnets for high efficiency transformer, power supply and motor applications. As a result of the enhanced solubility, a wide range of new alloy systems can be synthesized which are not available in conventional form.

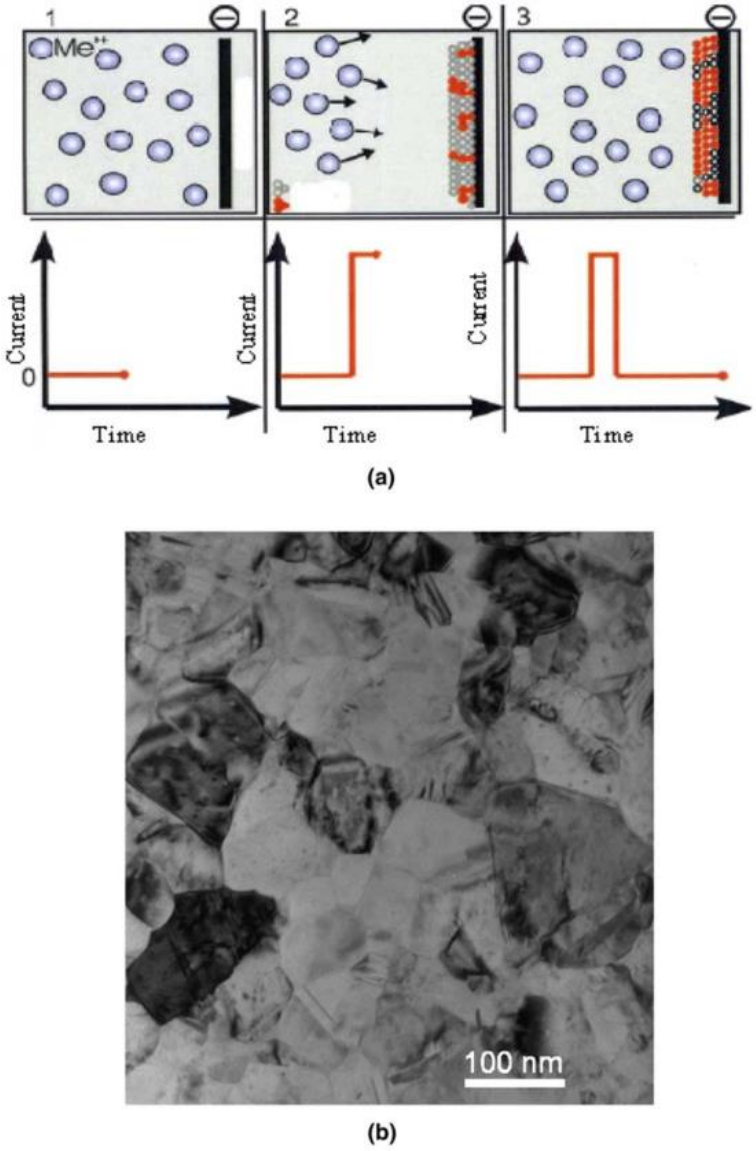

Figure 1-4. Pulsed electrodeposition set-up for synthesizing nanocrystalline materials. (b) Pulsed electrodeposited Ni [3].

1.2.4 Crystallization from amorphous material

Polycrystalline materials with nanometer-sized grains, termed nanocrystalline materials, can be formed by crystallizing completely amorphous solids under proper and optimized heat treatment

conditions in terms of annealing temperature and time, heating rate and etc [10]. The amorphous solids are in thermodynamic metastable states and they transfer into more stable states under appropriate circumstances. The driving force for the crystallization is the difference in the Gibbs free energy between the amorphous and crystalline states. Ni-P alloy with 9 nm crystallites was synthesized by means of crystallization from amorphous alloy [11]. Specific heat capacity and thermal expansion coefficient of the nanocrystalline Ni-P alloy prepared by this method were found to be greater than those of the coarse-grained crystalline alloy by 12.3% and 56.2%, respectively. Transformation of $Co_{33}Zr_{67}$ amorphous alloy to crystalline $CoZr_2$ with grain sizes of a few nanometers was found to be possible under specific thermal treatment in terms of temperature and heating rate [12]. Study on the properties of the nanocrystalline FeBSi alloy prepared using the crystallization method indicated that because of the unusual nature of its grain boundaries the nanocrystalline FeBSi alloy has much greater values of thermal expansion and micro-hardness than those of coarse grain crystalline and amorphous FeBSi alloys with the same composition [13]. TEM images and the selected area diffraction patterns of Ni–25at%W alloys annealed from amorphous atet at 723 K (Figure 1-5a) and 873 K (Figure 1-5b) for 24 h in vacuum show that extremely small sized grains can be crystallized from amorphous materials as shown and how the final nanostructure could be a function of the annealing temperature.

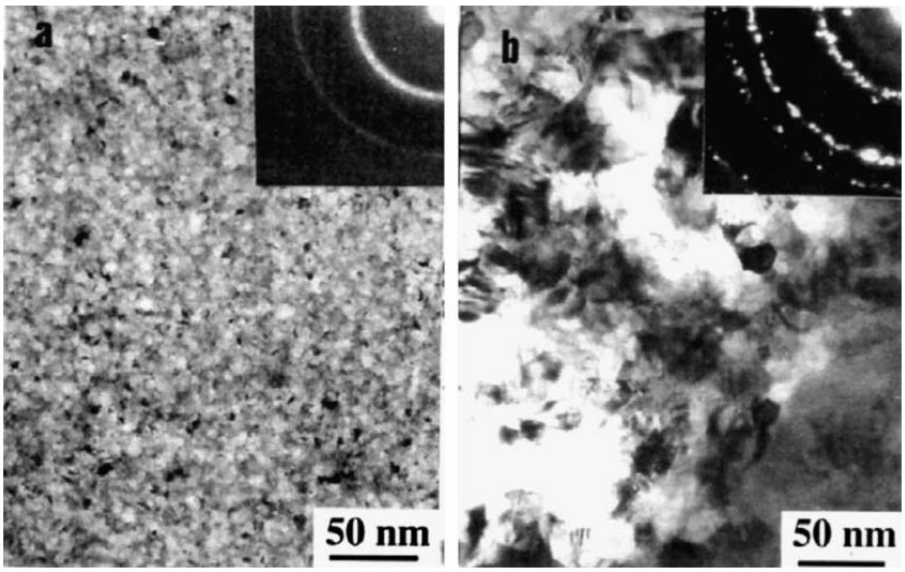

Figure 1-5. TEM images and selected area diffraction patterns in the Ni–25.0at%W alloy annealed from amorphous state at (a) 723K and for (b) 873K for 24 h in vacuum [3].

1.2.5 Severe plastic deformation

Severe plastic deformation is a possible and in fact very effective Avenue for microstructure refinement of metals, a concept that is as old as metalworking itself. Its application dates back to the ancient sword-making. It is defined as any method of metal forming under an extensive hydrostatic pressure that may be used to impose a very high strain on a bulk solid without the introduction of any significant change in the overall dimensions of the sample and having the ability to produce exceptional grain refinement [14]. The principal processing schemes are the following:

1.2.5.1 Equal channel angular pressing

The principle of ECAP is illustrated schematically in Figure 1-6. For the die shown in the illustration, the internal channel is bent through an abrupt angle equal to 90°. The sample, in the form of a rod or bar, is machined to fit within the channel and the die is placed in some form of press so that the sample can be pressed through the die using a plunger. The nature of the imposed deformation is simple shear which occurs as the sample passes through the die as shown schematically [15]. The theoretical shear plane is shown between two adjacent elements within the sample numbered 1 and 2, and these elements are transposed by shear as depicted in the lower part of the diagram. Despite the introduction of a very intense strain as the sample passes through the shear plane, the sample ultimately emerges from the die without experiencing any change in the cross-sectional dimensions. Since the cross-sectional area remains unchanged, the same sample may be pressed repetitively to attain exceptionally high strains. For example, the use of repetitive pressings provides an opportunity to invoke different slip systems on each consecutive pass by simply rotating the samples in different ways between the various passes [16].

1.2.5.2 High pressure torsion

High-pressure torsion refers to the processing of metals whereby samples are subjected to a compressive force and concurrent torsional straining [17]. Surface frictional forces therefore deform the disk by shear so that deformation proceeds under a quasi-hydrostatic pressure. Shear strain is induced during the process and is accumulated by increasing the number or torsional revolutions. Schematic of the process is illustrated in Figure 1-7. High pressure torsion processing leads to an excellent value for the strength of the material, reasonable microstructural homogeneity if the processing is continued through a sufficient number of torsional revolutions and there is a potential for achieving a capability for various attractive features including superplastic forming and hydrogen storage. There are also possibilities such as including the application of HPT processing to bulk and ring samples and the use of HPT for the consolidation of powders.

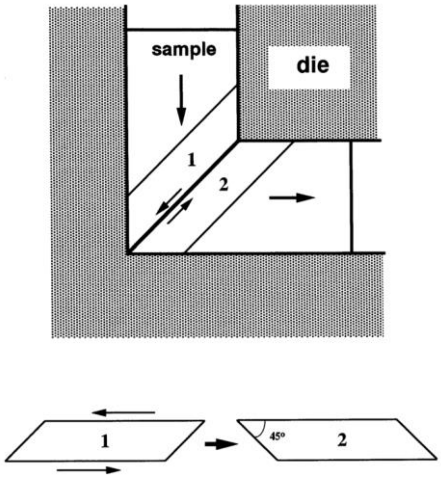

Figure 1-6. The principle of ECAP showing the shearing plane within the die: the elements numbered 1 and 2 are transposed by shear as indicated in the lower part of the illustration [15].

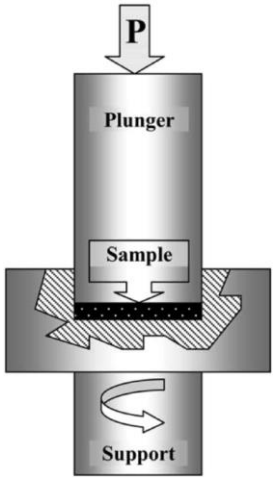

Figure 1-7. Schematic illustration of HPT processing [17].

1.2.5.3 Accumulative roll bonding

As schematically shown in Figure 1-8 stacking of material and conventional roll bonding are repeated during accumulative roll bonding [18]. First a strip is neatly placed on top of another strip. The interfaces of the two strips are surface treated in advance in order to enhance bonding strength. The two layers of materials are jointed together by rolling, as in conventional roll bonding process. Then the length of the rolled material is sectioned into two halves. The sectioned strips are again surface treated, stacked and roll bonded. The whole process is repeated again and again. The process can introduce ultra-high plastic strain and therefore microstructural

refinement without any geometrical change, if the reduction in thickness is maintained to 50% in every rolling pass. The achieved strain is unlimited since repetition times are endless in principle.

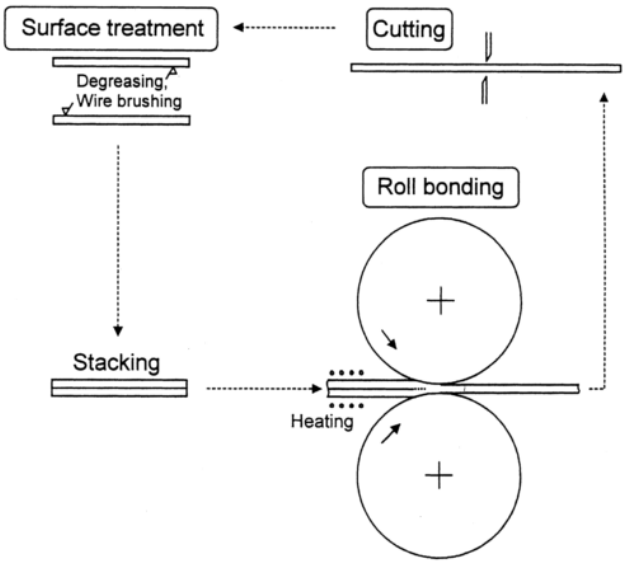

Figure 1-8. Schematic representation of accumulative roll bonding [18].

1.3 Mechanical properties of nanocrystalline material

1.3.1 Strength

The yield strength of polycrystalline metals is generally observed to increase as the grain size decreases according to the empirical Hall–Petch relationship:

$$\sigma_y = \sigma_0 + K_d d^{-1/2} \qquad (1\text{-}1)$$

Where d is the grain diameter, σ_y is the yield strength, and σ_0 and K_d are material dependent constants. A physical basis for this behavior is associated with the difficulty of dislocation movement across grain boundaries and stress concentration due to dislocation pile-up. Based on this equation, metals with nano-scale grains should be much stronger than their coarse-grained counterparts. Indeed, extremely high strength and hardness have been observed in nanocrystalline metals, especially recently using high-quality nanocrystalline samples. The strength and hardness have been found to increase with decreasing grain size. Variation of strength and hardness with grain size for Cu reported in the literature is presented in Figure 1-9 [19]. The hardness of NC Cu with an average grain size of 10 nm can be as high as 3 GPa,

corresponding to a yield strength of 1 GPa, which is more than one order of magnitude higher than that of coarse-grained Cu (50MPa). A similar plot is shown in Figure 1-9 b for the yield strength of various Cu specimens obtained from tensile tests. Clearly, the measured hardness as well as the yield strength follows the traditional H–P relationship, even when the grain size is as small as 10 nm. The mechanisms for the continued H–P strengthening down to10 nm are not fully understood yet, as the traditional picture of dislocation pile- ups is not expected to be applicable to NC grains [20]. Grain boundary-induced strengthening of nanocrystalline Ni–W was found to obey the Hall-Petch relation down to at least 20 nm, followed by a breakdown regime and even apparent weakening [21]. At the finest grain sizes approaching the amorphous limit, this breakdown is accompanied by shear banding as commonly observed in metallic glasses, evidenced both by shear offsets around residual impression sites and discrete discontinuities in the indentation responses.

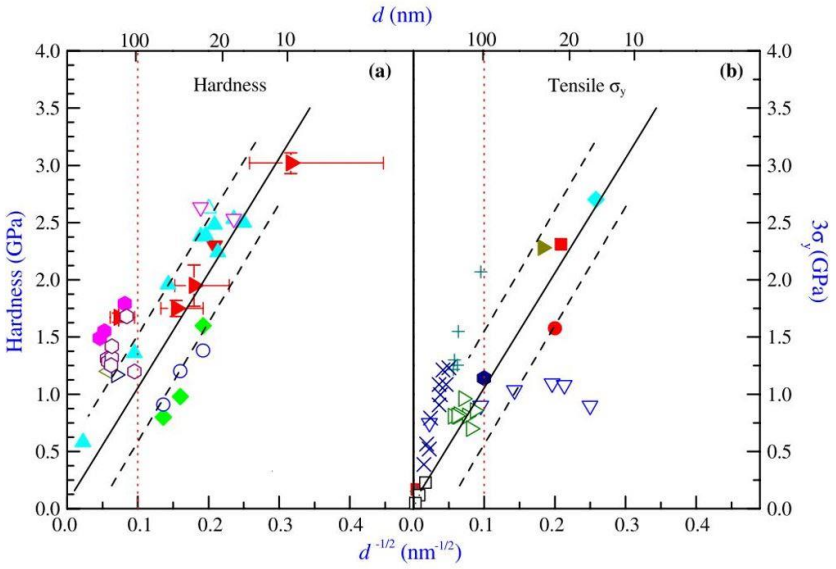

Figure 1-9. Summary of experimental data from the literature on the grain size dependence of strength of Cu specimens [19].

1.3.2 Ductility and fracture

The ductility of a metal is usually defined as the ability to plastically deform without failure, via fracture, under tensile stress. In addition to ultrahigh strength, which is a desired and expected benefit of nanostructuring, reasonably good ductility (tensile elongation 10% or above) is another attribute that NC or NC metals are required to possess in order for them to be practically competitive as new structural materials [20]. In early attempts, high-strength nanocrystalline and ultrafine-grained metals often showed much reduced room-temperature tensile ductility

compared with their coarse-grained counterparts mainly due to processing flaws and artifacts [22]. This is especially true when NC specimens were made by ‘‘two-step’’ processes; that required a consolidation step where large residual stresses, porosity, contamination from gaseous and metallic species as well as the imperfect bonding between particles are inevitable. However, artifact-free bulk nanocrystalline copper samples, synthesized by in situ consolidation through mechanical milling, with a narrow grain size distribution (mean grain size of 23 nm) exhibited tensile yield strength about 11 times higher than that of conventional coarse-grained copper, while retaining a 14% uniform tensile elongation which is much greater than that previously reported for all NC metals of similar grain size [23].

1.3.3 Strain rate and temperature dependency of strength

The strain rate and temperature dependence has been found to be rather strong in NC or NS metals, more so than had been realized previously [20]. In the case of fully dense nanocrystalline Ni the results of two different experimental techniques i.e. depth-sensing indentation and tensile testing revealed that the strain-rate sensitivity is a strong function of grain size. Specifically microcrystalline and ultra-fine crystalline pure Ni, with grain size range of >1 μm and 100–1000 nm, respectively, exhibit essentially rate- independent plastic flow over the range 3×10^{-4} to 3×10^{-1} s^{-1}, whereas nanocrystalline pure Ni with a grain size of approximately 40 nm, exhibited marked rate sensitivity over the same range [24]. The engineering parameter measuring strain-rate sensitivity, m, is commonly defined as

$$m = \frac{\partial \log \sigma}{\partial \log \dot{\varepsilon}} \qquad (1\text{-}2)$$

where σ is the flow stress and $\dot{\varepsilon}$ is the corresponding strain rate. Figure 1-10 summarizes the variation of *m* as a function of grain size, *d*, for Cu samples, based on literature data. Despite some inconsistencies in the absolute values obtained from different research groups or those arising from different sample synthesis methods and different testing methods, there is a consistent and clear trend: the m value increases with a decrease of grain size from the micron to the sub-micrometer scale (m from 0.006 to about 0.02), followed by an obvious ‘‘take-off’’ when the grain sizes are reduced to below a couple of hundred nanometers [20]. In the nanoscale regime, m is much larger than that reported for conventional Cu. The current suggestion is that the highly localized dislocation activity (e.g. dislocation nucleation and/or dislocation depinning) at the GBs leads to an enhanced strain-rate sensitivity for NC metals[20]. There have been arguments that the enhanced strain rate sensitivity in nc/ns metals might play a role in improving strength/ductility properties [25,26].

There is also more pronounced temperature dependence, in NC materials arising from the thermally activated deformation mechanisms controlling the plastic flow. At liquid nitrogen temperature, the yield strength of nanocrystalline Ni and Co increased by as much as 50%–80% over the already-impressive (~1 GPa) room-temperature values [27]. This unusual strength ratio as well as the remarkable magnitude of flow stress, reached (as high as 2.5 GPa), are unexpected for conventional close-packed pure metals. The strong temperature dependence is attributed to the unusually small activation volume measured in strain rate change tests [27].

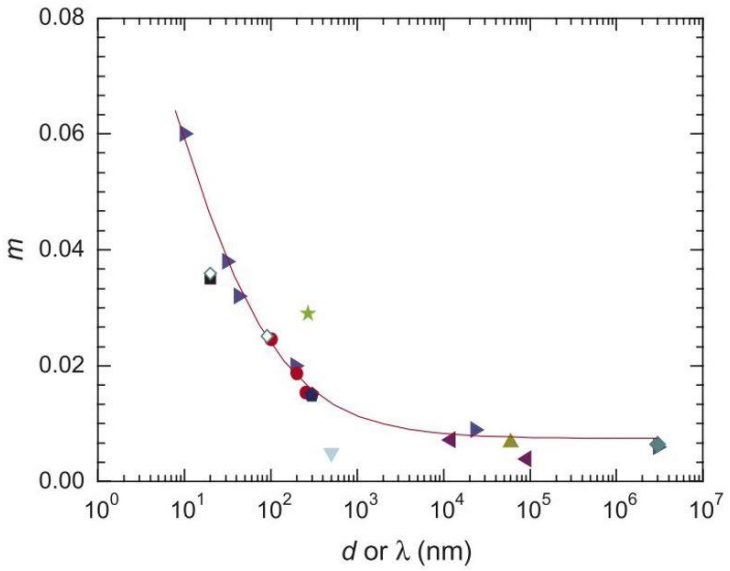

Figure 1-10. room temperature strain rate sensitivity, as a function of grain size, d, for Cu from the literature [20].

1.3.4 Fatigue

NC and UFC regimes can have a substantial effect on total life under stress-controlled fatigue and on fatigue crack growth [28]. Fully dense NC and UFC Ni produced by electrodeposition exhibited substantially higher resistance to stress-controlled fatigue compared to conventional microcrystalline Ni. However, fatigue crack growth results for NC and UFC Ni also appear to indicate that grain refinement in the NC regime can have a deleterious effect on the resistance to subcritical fatigue fracture [28]. To explore the generality of the above trends, systematic experiments were also performed in ultrafine-crystalline pure Ti produced by equal-channel angular pressing where a reduction in grain size was found to cause an increase in fatigue crack growth rates at different tensile load ratios [29]. Grain refinement from the microcrystalline to the ultrafine-crystalline regime by cryomilling of Al alloys also showed a similar response[29]. The micromechanical model proposed in [30] suggested that predominantly crystallographic and

stage I crack growth result in microstructurally tortuous crack paths in coarser grained materials. The crack path is much less tortuous with decreasing grain size which can explain the higher rate of crack growth.

1.3.5 Tribological properties

Ball-on-disc tribometer with cemented tungsten carbide ball as the counterface was used to investigate dry sliding tribological behavior of an electrodeposited nanocrystalline Cu and a conventional coarse-grained Cu [31]. Enhanced wear resistance of copper with the nanocrystalline microstructure was observed relative to the coarse-grained material. The steady-state friction coefficient of the nc Cu was lower than that of the coarse-grained Cu when the load is below 20 N. The wear volume of the nc Cu was always lower than that of the coarse-grained Cu for the applied load range from 5 to 40 N. It was shown that the difference in wear resistance between the nc and the cg Cu decreases as the load increases. The enhancement of the wear properties of the nc Cu was associated with the high hardness and the low work-hardening rate of the nanocrystalline structure, and easily being oxidized of wear debris, which was attributed to grain refinement. Similar results was found the numerical framework established in [32] to evaluate frictional sliding the overall friction coefficient decreased slightly with an increase in yield strength or strain hardening exponent.

1.4 Conclusion

Nanocrystalline materials has been become an attractive avenue of research an application in the last decade. It is because of their outstanding and peculiar properties of which mechanical properties were the focus of this section. Possibility of increasing strength while retaining ductility has been found an interesting observation as the compromise between these two has been always an issue for researchers and engineers. Enhanced wear resistance and carrack initiation improvement by NC materials made them an attractive material for in service application. However, there is still a long way to adopt the various kinds of synthesis summarized here in order to successfully produce porosity/contamination free, NC material of sufficient size and desired shape for industrial application.

2 Shot peening and surface nanocrystallization

2.1 Introduction

Various kinds of synthesis techniques have been developed for producing 3 dimensional bulk nanocrystalline samples, such as what have been summarized in the previous section. With these methods, different bulk NC materials have been successfully prepared that are essential to understand the intrinsic structure and properties of polycrystalline materials with ultrafine grains. Up to the present, at least two major difficulties still exist in synthesizing 3-D NC materials using current techniques [33]:

- It is difficult to synthesize "ideal" 3D NC samples, i.e., that are porosity-free, contamination-free and of sufficient size for conventional property measurements for revealing the intrinsic nanometer-grain-size effect on the structure-property relationship without any external influencing factors.
- Most of the current techniques for synthesizing NC materials are difficult to transfer into industrial-scale applications, due to their limitations in cost, sample size and types of materials.

It is known that material failures occur on the surface, in most cases. Most material failures, including fatigue fracture, fretting fatigue, wear and corrosion, are very sensitive to the structure and properties of the material surface. Optimization of the surface structure and properties may effectively improve the global behavior of the material. With the increasing evidence for NC materials' unique properties, it was proposed to achieve surface modification by generation of a nanocrystalline surface layer so that the overall properties of the material might be significantly improved [34]. This kind of surface modification, called surface nanocrystallization (SNC), will provide a new approach that makes it possible to meet specific structure/property requirements on the surface of the material.

Shot peening is a very promising process able to avoid the disadvantages of bulk nanocrystalline materials synthesis (contamination, porosity, dimensions, etc.) yet able to obtain adequate properties of nano-structured materials. Shot peening as a mechanical process and important parameters to ensure its repeatability are described in section 2.2. Different versions of peening to obtain nanostructured surface are introduced in section 2.3. The involving mechanisms of grain refinement in surface nano-crystallization by peening and existing experimental observations are given in the form of state of the art in section 2.4.

2.2 Shot peening

Shot peening is an approved, well-established type of mechanical surface treatment having the objective of enhancing the resistance of metallic components which are exposed to cyclic loading, wear and corrosion under applies stress [35]. During the process small spherical peening

media (shots) are accelerated in various kinds of peening devices to hit the surface of work piece with energy able to cause plastic deformation, compressive residual stresses and work hardening in the surface layers [36,37]. Therefore, shot peening is able to totally prevent or considerably retard the failure of the mechanical component. Compressive residual stress induced by shot peening is usually introduced as the main advantageous effect of shot peening [38–42]. However, grain distortion and increases microstructural barrier [43] and also surface work hardening of the peened specimen [44] were also affirmed to be able to be introduced as the main advantage of the process. Shot peening is a highly industrialized technique. Therefore, two standard parameters (intensity and coverage) have been introduced in order to ensure repeatability.

2.2.1 Intensity

Determining the impact energy level of a shot stream is one important means of ensuring process repeatability in a shot peening application. During 1940's J. O. Almen [36] developed a standard process to measure the kinetic energy transferred by a shot stream. The measurement of peening intensity is accomplished by determining its effect on standard test strips. The test strip (Almen strip) and a gage (Almen gage) used to measure the strip's curvature have been standardized and specified for the shot peening industries. Standard test strips A, N and C are shown in Figure 2-1 the three letters represent three different thicknesses of strips for different intensity levels. Whereas N strip is for low intensity levels, the A strip is the most common and C is used for very high intensities only. The material used to produce the test strips is an SAE 1070 CRS (cold rolled spring steel) with a standard hardness of 44-50 HRC [35]. Figure 2-1 also shows the Almen gage, which uses four balls to support the strip. It can be used to measure both span wise and chord wise curvature when measuring the curvature of the strip. An Almen strip holder shown in Figure 2-1 is also needed to hold the strip in place while it is exposed to the shot stream. After the strip has been exposed to the shot stream and removed from the holding fixture, the gage stem is placed against the non-peened surface. The measured strip deflection represents a single arc height at the given exposure time or one data point on the graph of Figure 2-2. Intensity is expressed as the arc height of a shot peened test strip at saturation. Saturation is defined as the earliest point of the saturation curve that, if the exposure time is doubled, the arc height increases as 10% or less [35]. In fact, establishing a saturation curve is accomplished by peening a series of Almen strips, using different exposure time, with all other shot peening parameters kept constant. Plotting the arc height on the vertical axis and exposure time on the horizontal axis, the arc heights will define a curve with a general shape as shown in Figure 2-2. Media size, media hardness, media density, shot flow rate, shot velocity, distance and the angle of impingement are the main processing parameters that directly affect the intensity.

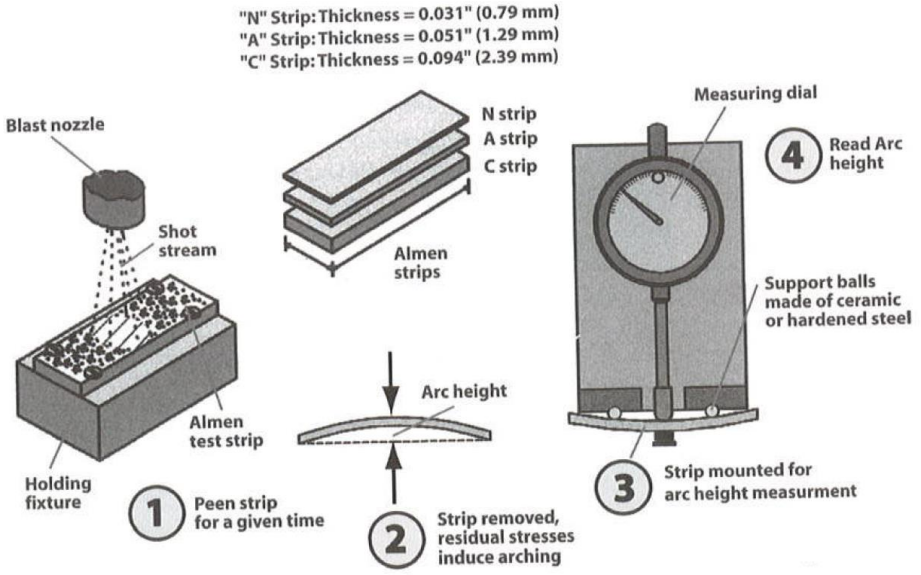

Figure 2-1. The process to obtain a single arc height on a saturation curve [35].

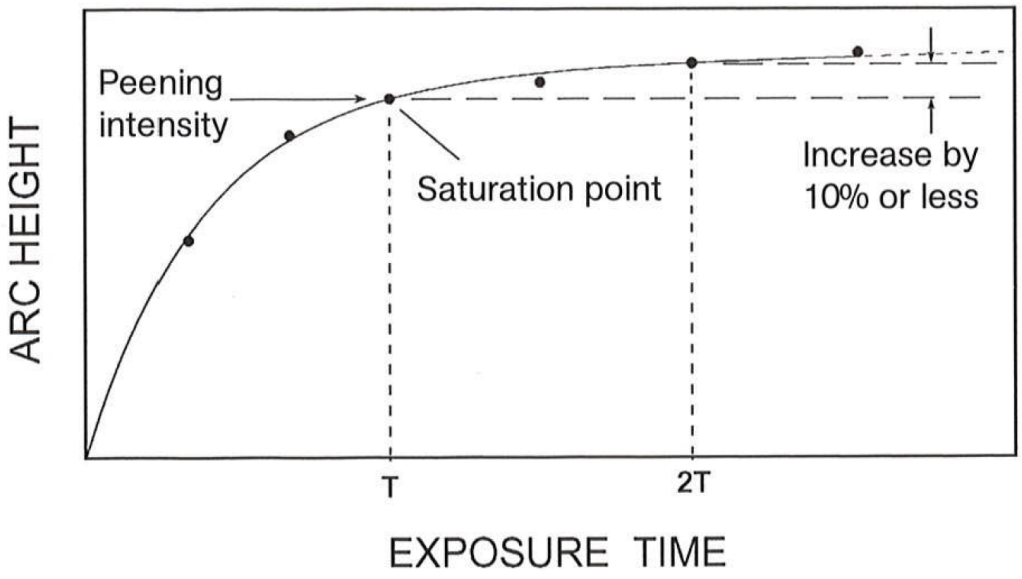

Figure 2-2. Schematic saturation curve [35].

2.2.2 Coverage

The notion of coverage is based on the research work done by Wheelabrator Corporation, an American company based in Mishawaka, Indiana. Coverage is practically the most important measurable variable of the shot peening process. It is defined as the ratio of the area covered by hits and the complete surface treated by shot peening expressed as a percentage. Coverage of

98% is a degree of coverage, which can still be assessed visually. It is considered to be full coverage [45] or 100% coverage, in another word, the minimum coverage needed to get the improvement from the peening process. The corresponding duration of the shot peening process after which this coverage is obtained is frequently called shot peening time t98%. Coverage control is an essential feature of a correctly applied shot peening. The correlation between the coverage and the ratio of the impacted area to the total area was proposed [46] to have and Avrami type [47] behavior. Variation of coverage with peening time is shown in Figure 2-3. In the early stage impressions are likely to occur without overlap so that coverage increases linearly with time. As the surface progressively becomes covered the probability of the overlap increases so that the rate of coverage must decrease. Finally when a large proportion of the area has been covered there remains a smaller and smaller proportion of the area to be covered. The probability of this very small area being covered by a new impression becomes smaller and smaller. Hence the approach to 100% coverage is exponential and 100% coverage is theoretically impossible [46]. Coverage higher than 100% can be obtained by multiplying the time needed to reach 98% coverage. For instance 200% coverage means the time of peening is set to be twice the time needed to attain 98%.

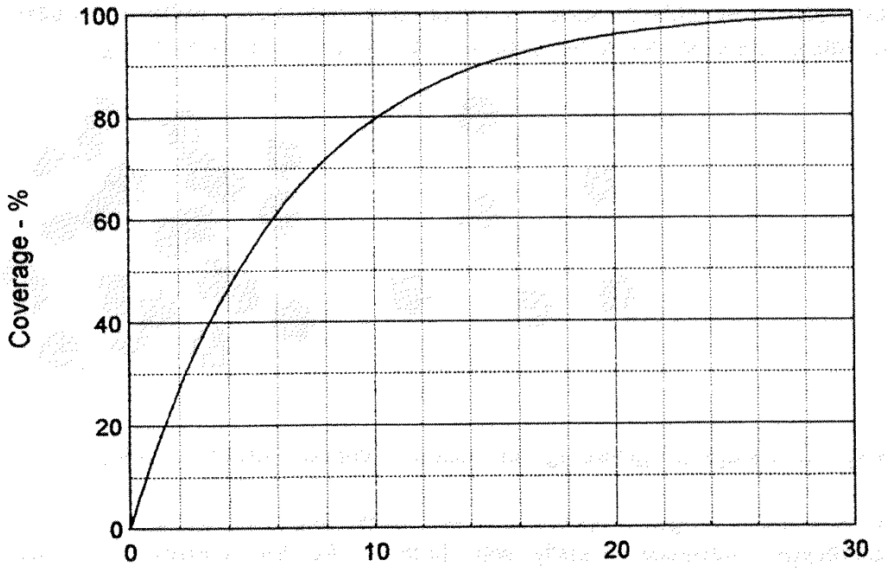

Figure 2-3. Variation of coverage with peening time [46].

2.3 Shot peening processes to obtain surface nanocrystallization

It has not been a long time that shot peening was recognized as a potential process to produce surface nano-crystallization. The common aspect is to use special combinations of peening parameters to multiply the kinetic energy of the shot impacts in order to generate a large number

of defects, dislocations and interfaces (grain boundaries) on the surface layer of treated part and consequently transform its microstructure into ultra-fine grains or nano-structure. Different shot peening processes that can be used to generate surface nanostructures are classified here.

2.3.1 Shot blasting

The main objective of shot blasting or sand blasting is surface cleaning or corrosion removal. However, local plastic deformation in the subsurface layer tends to creation of compressive residual stress. The media size and its geometry are rather random in sand blasting. Media size in blasting is usually smaller than that of conventional shot peening. Sand blasting and subsequent annealing was shown to be able to successfully generate surface nanocrystallization in 304 stainless steel [48,49], brass alloy [50] and pure Ti [51]. The grain size in the surface layer of the blasted stainless steel was in the range of 20 nm and nanocrystalline layer was about 70 μm thick [48,49]. The sandblasted surface layer was heavily plastically deformed and consequently had high density dislocations. After annealing (recovery treatment), the initially formed dislocation network or fine “sub-grains” (~20 nm) changed to nano-sized grains with sharper grain boundaries. In these nano-grains, dislocations had been significantly decreased [49].

2.3.2 Air blast shot peening

Air blast shot peening in a peening process in which shots are acetated by means of compressed air. Figure 2-4 shows the schematic illustration of air blast shot peening. In comparison to the other kinds of peening, air blast shot peening can be characterized by a narrow distribution of impact velocity and mainly perpendicular impacts of media on the treated surface [52]. Nanocrystalline structure characterized by grain size in the range of 10-20 nm and thickness of several μm was successfully produced by performing air blast shot peening on the surface of silicon steel, carbon steel, high strength steel with different ferrite, pearlite, spheroidite and martensite structures [52–56]. The common feature of the all these studies is that high coverage and velocity have been applied to obtain surface nanocrystallization.

2.3.3 Ultrasonic shot peening

In ultrasonic shot peening [33], sometimes also called surface mechanical attrition [57], spherical steel balls with smooth surface are placed in a reflecting chamber that is vibrated by a vibration generator with vibration frequency ranging from 50 to 20 kHz. When the balls are resonated, the sample surface to be treated is impacted by a large number of flying balls over a short period of time. The impact directions are random due to the random flying directions of the balls inside the vibration chamber. As a consequence, the repeated multidirectional impacts at high strain rates onto the sample surface result in severe plastic deformation in the surface layer. Because of the

high possible frequency of the system (20 kHz), the entire surface of the sample to be treated can be peened with a high number of shots in a short period of time. Figure 2-5 shows a schematic illustration of the USSP treatment device. Media used in ultrasonic shot peening is usually larger than air blast shot peening. The size falls in to the range of 1-10 mm. In the case of larger media the process is called high energy shot peening [58]. High energy shot peening is in principal similar to ultrasonic shot peening but with lower frequency. Ultrasonic shot peening was found to be a very successful treatment for surface nanocrystallization in iron [33], low carbon steel [58–60], stainless steel [61–64] copper [65] and Al alloys [66].

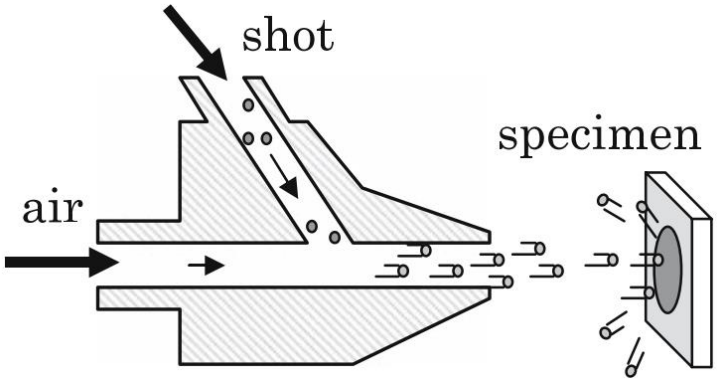

Figure 2-4. Schematic illustration of air blast shot peening [56].

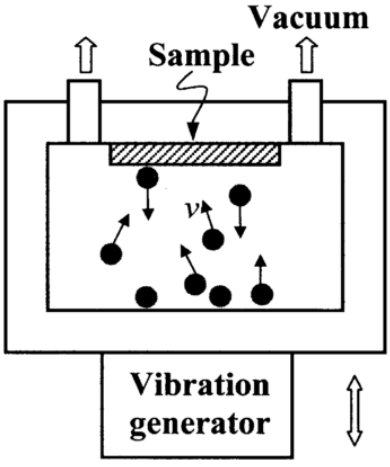

Figure 2-5. Schematic illustrations of the USSP or SMAT treatment set-up [57].

2.4 State of the art

Mechanically induced surface self nanocrystallization involves a grain refinement process with the application of mechanical treatments, often repeated multidirectional plastic deformation due to the contact loading which in turn creates localized severe plastic deformation and grain refinement progressively down to nanometer regime. Figure 2-6 shows the initial stage of nanostructure development by means of mechanical treatments [34]. Under contact loading deformation localized in specific shear bands is crated on the surface of material, which consists of an array of dislocation with high density. The second contact loading in a different direction may activate deformation in other shear band systems. When the action is repeated many times, the initial crystallite might be divided into a large number of sub-grains (or domains) separated by small angle grain boundaries that results from annihilation and recombination of the dislocation arrays. Further mechanical treatments may lead to a change of orientation on the part of the sub-grain with respect to its neighboring grains, eventually becoming completely random. Therefore, a metastable nanocrystalline layer is developed on the surface of the material.

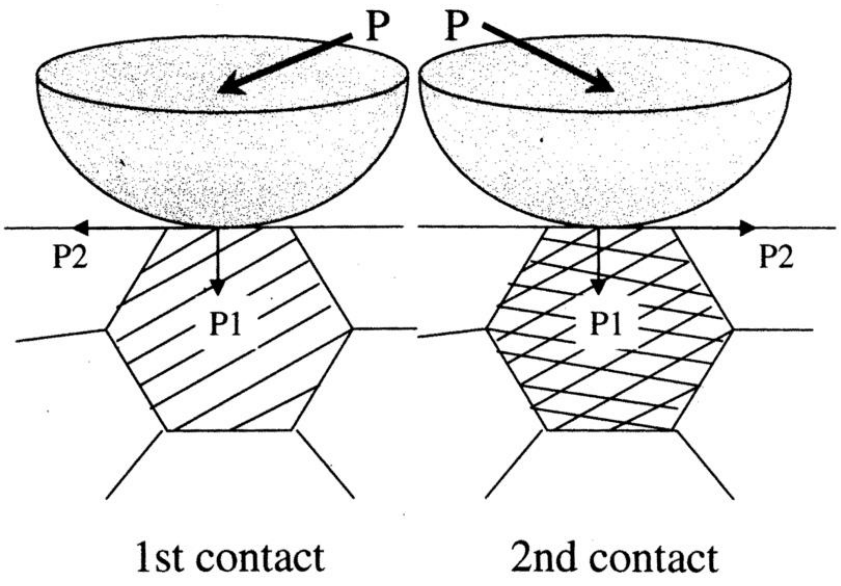

Figure 2-6. Repeated multidirectional plastic deformation leading to different shear bands with a high density of dislocation array [34].

USSP of pure iron plate, using stainless steel shot of 3 mm diameter successfully fabricated nano-crystalline surface layer [33]. The average grain size of the surface layer was found to be about 30 nm when the treatment duration was between 50–450 s. With a longer treatment time (1250 s), the average grain size was increased to about 37 nm. TEM micrographs revealed uniform ultrafine grains that are mostly equiaxed. The mean grain size of the surface was

approximately 10 nm and 16 nm in the samples peened for 450 and 1250 s, respectively. Temperature raise during shot peening for a longer time was expressed as possible reason elevating the stable grain size with which a balance between dislocation generation and its recovery is established. Localization of plastic deformation occurs in multiple shear bands due to differences in multiple loading directions of shots. Rearrangement of dislocations (annihilation or recombination) forms small angle grain boundaries separating individual grains.

XRD measurement showed the average grain size in the surface layer after USSPing of 316L stainless steel using 3 mm diameter shot for 30s is 20 nm [61]. It decreases to 15 nm as the treatment time increase to 90 s and no further refinement was obtained by longer treatments. In fact longer treatments for 270 and 810 s came up with slightly larger average grain size of 17 nm. Multiple-slip evidences were observed near the surface while they were gradually replaced by single slips with an increasing depth. The average grain size in the surface layer was estimated to be 10 and 15 nm for 30 and 810s treatments respectively. Typical microstructures in the subsurface layers include sub-grains or grains with irregular shape, high density of dislocations, nano-scale shear bands and twins. The increase of USP duration does not change significantly the grain size of the top layer, but increases the thickness of the NC structure.

High energy shot peening of a low carbon steel was conducted for 30 to 180 min [58]. High energy shot peening is in principle similar to USSP but with lower frequency (3 kHz for instance as compared with 20 kHz in USSP) and bigger shots (diameter of 8 mm). The average grain size at the top surface layer, calculated by XRD, decreases from 33 nm for 30 min to 23 nm for 90 min. Afterwards it slightly increased to 27 nm for 180 min treatment. In depth measurement of grain size showed a slight increase from 27 nm at the top surface to 46 nm at 20 μm depth and then it encountered a rapid increment to the micrometer regime. TEM observation showed that the shape of nano-crystalline grains is roughly equiaxed. The average grain size in the top surface was approximately 8 nm. Pronounced increment of yield strength without significant reduction of elongation was achieved after HESP for 30 min. For further increasing the treatment time both strength and ductility approached a saturated value.

Later on it was shown that the possible surface nanocrystallization mechanisms could be related to the level of stacking fault energy [67]. TEM cross sectional observation of SMATed iron (high stacking fault energy) revealed that four different sections exist [57]: nanostructured layer, sub-micro-sized regime, micro-sized regime and matrix with plastic deformation evidences. Based on the micro/nano-structural features observed in each section it was proposed that through the course of straining dislocations generate and arrange themselves into various configurations such as dense dislocation walls in specific slip planes, dislocation tangles inside the original grains. By further straining and in order to minimize the total energy of the system annihilation and rearrangement occur by transformation of dislocation walls and tangles into sub-boundaries with small misorientation. With further straining, sub-grain boundaries evolve into high- angle grain boundaries that subdivide the original grains into refined structures.

The prominent feature observed adjacent to nanostructured layer in stainless steel (low stacking fault energy) is formation of planar dislocation array and mechanical micro-twin when strain increases [62,63]. The original coarse grain in this case is sub-divided into lamellar twin matrix alternate block with nanometer-sized thickness. By further straining dislocations inside the lamella arrange themselves into dislocation walls and cut through the thickness of microtwins lamella. Cutting might also occur by twin-twin intersection and form nanometer sized blocks. By accommodating higher misorientation as plastic deformation increases, randomly orientated nanocrystallites are formed.

In the case of SMATed copper (medium stacking fault energy) two different mechanisms of refinement were identified [65]. In the subsurface layer with lower strain arte, dislocation activities form dislocation cells instead of dislocation walls or tangles. The grain refinement is accomplished by transformation of dislocation cell walls to into sub-boundaries with small misorientation. The last stage of refinement is transformation of sub-boundaries into grain boundaries by accumulation of misorientation. In the top surface layer (thickness <25 μm) however, the grain refinement mechanism is pretty much the same as described for low stacking fault energy materials.

The grain refinement process along the depth direction after multiple laser shock peening impacts on 304 stainless steel was described as follows: (i) formation of planar dislocation arrays (PDAs) and stacking faults along multiple directions due to the pile up of dislocation lines; (ii) formation of submicron triangular blocks (or irregularly shaped blocks) by the intersection of mechanical twins (MT–MT) or (MT–PDA or PDA– PDA) along multiple directions; (iii) transformation of MTs into sub-grain boundaries; (iv) evolution by continuous dynamic recrystallization of sub-grain boundaries to refined grain boundaries [68].

The surface NC structure with equiaxed grains of around 20nm was formed in various steels by SP. The thickness of NC layer increased with increasing coverage and remained unchanged (around 40 μm thick) after a certain level of coverage. However, measurement of the grain size after recrystallization at the 10 μm inner position revealed and ever decreasing trend as coverage increases [55].

8 times of a 4 mm diameter steel particle impact with 120 m/s velocity at LN2 temperature induced nano-crystalline layer mainly in the sub-surface of a carbon steel specimen [53]. The NC layer formed after ball drop experiment appears at top surface along the edge of crater and also about 100 μm below the surface at the bottom of the crater [54]. Vicker's indentation revealed that the micro-hardness of the nano-crystalline layer was 9.5 GPa which is substantially higher than the surrounding work-hardened region (4.3 GPa). The fact the nano-crystalline layer was not formed at the top surface was associated to the friction between surface of the specimen and the ball and so the limited deformation occurring there. Air blast shot peening of high strength steel using cast steel shot of less than 50 μm diameter with 120 m/s velocity and high coverage (1000% to 6000%) induced nano-crystalline layer of several microns thick at the top

surface [54]. The nano-crystalline layer was found to be separated from the work-hardened region by clear and sharp boundary. Several reasons including impurities, martensitic transformation, unique deformation mode and common phenomena in deformation irrespective of materials or mode of deformation may contribute simultaneously. However, the evidences are not convincing enough to make the real mechanism clear. It is seen that the area fraction and thickness of the nano-crystalline layer increased with peening time. Minimum amount of strain necessary for nano-crystalline structure to be induced was estimated to be around 7-8. Favorable conditions of formation of NS were introduced to be low temperature deformation, repetitive or cyclic deformation, multidirectional deformation, impurities and/or alloying elements, second phase and hydrostatic pressure. The most important condition of nano-crystallization of steel was mentioned to be imposing a strain larger than about 7. Nano-grained structure and dislocated cell structure region without any intermediate structure was realized in the milled Fe powder was also observed in the air balst shot peened steel specimen. A drastic change of micro-hardness from 7 to 3 GPa at the boundary of these two regions was observed. General microstructural evolutions at various stages of deformation are as follows [54]: At small strains, original grains are subdivided into cells bounded by dislocation walls (called incident dislocation boundaries (IDBs)) with small misorientation. With increasing strain, cell size and cell wall width decrease and geometrically necessary boundaries (GNBs) develop. GNBs are boundaries which separate a group of neighboring cells with same slip system (called a cell block) from those with different slip systems. With further increase in strain, the density of GNBs and the misorientation of GNBs increase. Since the deformation induced high angle boundaries contain high density of dislocations and are distorted elastically, they are called non-equilibrium grain boundaries. The dislocation density inside grains is low in spite of the large strain imposed. When the grains are refined to 10nm range, the microstructure reaches a steady state since further strains are mainly accommodated by grain boundary sliding.

By comparing the microstructure of samples with different coverage [56], it was found that the coverage has significant effect on the feature of nano region, although the depth of deformed layer attain a steady value with coverage greater than 3000%. In the sample with lowest coverage 3000%, only some separated areas like island are formed. When using small shot sizes (0.05 mm), the nano area can be formed in very short treatment times, and the thickness and continuity of the nano-layer is enhanced. On the contrary, the nanocrystalline region is more difficult to synthesize when using large shot particles (0.8 mm), even though the deformed area is much thicker. When collide with sample surface, although bigger particles have higher energy, but the contact area also rise at same time, then the strain rate with bigger particles is smaller than that in the case of smaller particles.

It has been recognized that NC structure cannot be formed by ARB or ECAP in which homogenous deformation occurs. This suggests that deformation with large strain gradient is a critical condition for the formation of nano-crystalline structure. High speed drilling was able to

produce nano-crystalline structure near the surface of drilled hole. The strain gradient necessary to obtain nanocrystalline structure was roughly estimated to be 1.4 μm^{-1} [69].

2.5 Conclusion

Since most material failures including fatigue fracture, fretting fatigue, wear and corrosion are very sensitive to the structure and properties of materials surface, surface nanocrystallization was proposed to be a convenient alternative to bypass the difficulties of synthesizing buck NC component and yet harvesting the advantages of nanostructures in service. The basic idea used to disclose the concept of mechanically induced surface nanocrystallization is that repeated multidirectional plastic deformation caused by high velocity impacting balls localizes high dislocation density in multiple shear bands. Recombination/Rearrangement and Annihilation of the dislocations by the continuation of impacts divide the initial crystallite into a large number of sub-grains (or domains) separated by small angle grain boundaries. Further mechanical treatments may lead to a change in the orientation of the grains with respect to its neighboring grains, making them eventually completely random.

Ultrasonic shot peening (sometimes called surface mechanical attrition) has been found to successfully produce surface nanocrystallization. Air blast shot peening is another kind of peening in which shots are accelerated by means of compressed air. Because of its simplicity, low cost and applicability to variety of targets it is a popular process in industries. If one uses special combinations of peening parameters to multiply the kinetic energy of the shot impacts it is possible to transform its microstructure into ultra-fine grains or nano-structure.

3 Nitriding and its combination with peening

3.1 Introduction

Fatigue strength of mechanical components can be greatly enhanced by generating compressive residual stress, increasing the hardness and reducing the grain size. It is well known that while the use of mechanical treatments is able to generate an effective field of compressive residual stresses and, if severe parameters are used, to cause grain refinement, thermochemical treatments are able to increase the surface hardness. This justifies the interest in developing combined treatments, able to achieve all the just mentioned factors. This is the motivation that, the effect of combination of severe shot peening and nitriding on the fatigue limit and mechanical properties is investigated in this research.

In section 3.2 nitriding is briefly introduced. In section 3.3 the effect of combination of peening and nitriding is discussed based on the existing evidences from literature. In this regard, literature can be some researcher applied shot peening after nitriding and some other studied the reverse process. Potentials and benefits of each are covered in the here.

3.2 Nitriding

Gas nitriding is a case hardening process whereby nitrogen is introduced into the surface of a solid ferrous alloy by holding the metal at a suitable temperature (below Ac1, for ferritic steel) in contact with nitrogenous gas, usually ammonia [70]. The work-piece is heated to the nitriding temperature with ammonia flowing into the retort. The ammonia gas dissociates to nitrogen and hydrogen at the part surface. The nitrogen diffuses into the work-piece in atomic form, and the hydrogen becomes a part of the furnace atmosphere. Schematic drawing in Figure 3-1 illustrates the process. As a result released nitrogen atoms either chemically react with or diffuse between iron atoms and a case hardened surface is generated. The hardened case itself is sub-classified into compound and diffusion layers. Formation of iron nitrides on the immediate surface results in the so-called compound or white layer. Composition of this hard and brittle layer is dependent to nitriding potential and temperature. However, with the conventional processing parameters it is usually a combination of ϒ´ (Fe_4N) and ε ($Fe_{2-3}N$) phases. Beneath the compound layer, nascent nitrogen atoms interstitially diffuse into octahedral interstices of BCC structured iron and the so-called diffusion zone is formed. Precipitation of alloying elements after combination with nitrogen can also take place in the diffusion zone. Typical nitrided case is shown in Figure 3-2. Due to its considerable improvement in wear, corrosion and fatigue resistance, nitriding has become a well-accepted thermo-chemical process which is widely applied for high performance transmission shafts and gears, bearings, extruder screws, forging dies, injectors, crankshafts, camshafts and so on.

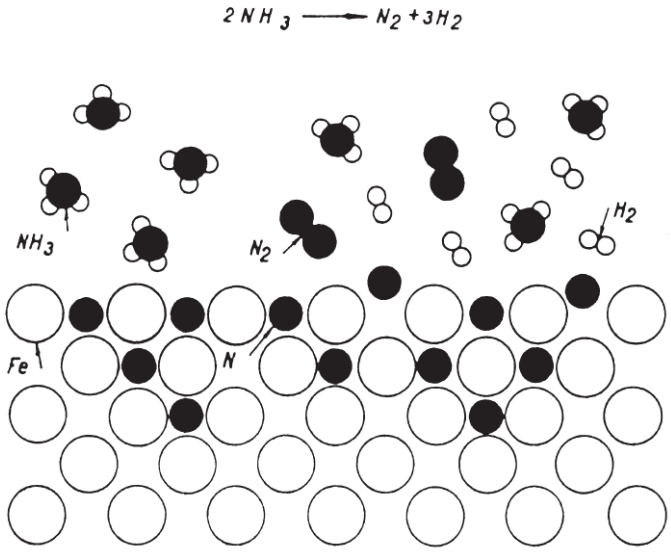

Figure 3-1. Schematic of interstitial diffusion during the nitriding process [71].

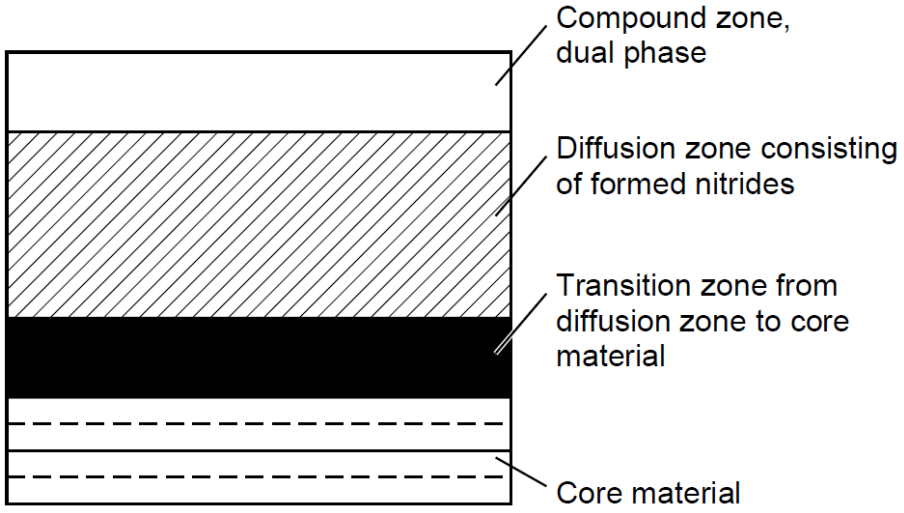

Figure 3-2. Typical nitrided case.

3.3 Combination with peening

While there is a solid background in the literature that both shot peening and nitriding can improve fatigue behaviour, their combination is less investigated. In this regard, literature can be classified into two main groups. Some researcher applied shot peening after nitriding and some other studied the reverse process.

3.3.1 Nitriding followed by shot peening

Freddi et al. [72] performed nitriding on 32CrMoV13 steel specimens and subsequently subjected them to shot peening, varying shot diameter and Almen intensity in two levels. The specimens then were subjected to fatigue test. Slight improvement (5-10%) of fatigue limit depending on peening parameters was reported for combined treatment as compared to nitriding. Croccolo et al. [73] subjected unnotched and notched 32CrMoV13 steel specimens to shot peening after nitriding. No significant enhancement of fatigue limit (only 3%) with respect to the nitrided only specimens was reported for smooth specimens. Rolling contact fatigue property of the same steel was investigated after deep nitriding and following shot peening. Following shot peening could prolong rolling contact fatigue life and make the spalled pit lower and smaller [74]. Contact fatigue test performed on carbo-nitrided only and carbo-nitrided plus shot peened gears made of AISI 4130 steel showed that damage to the gears appears after about the same testing time for both kinds of treatments but in different forms: pitting and spalling for the carbo-nitrided only gears and micro-pitting for the carbo-nitrided and shot peened gears [75]. This combination was not always beneficial. Deterioration of surface durability during sliding rolling contact fatigue behaviour of maraging steel subjected to nitriding and fine particle peening was also reported in the literature [76].

Fernandez Pariente et. al. [44] Investigated the effect of nitriding plus shot peening on fatigue strength of a low alloy steel specimens containing a micro-hole, acting as a pre-crack. The threshold value of stress intensity factor increased from 14.2 $MPa.m^{1/2}$ for nitrided specimen to 25.1 $MPa.m^{1/2}$ for nitrided plus shot peened specimens. Terres et al. investigated the effect of nitriding and the following shot peening on bending fatigue of 42CrMo4 steel. Their result demonstrated that more improvement (35%) for fatigue limit was obtained by nitriding plus shot peening with respect to the nitrided only specimens (8%). This was mentioned to be due to the hardened layer that retarded the initiation of a fatigue crack by constraining the plastic deformation [77].

3.3.2 Shot peening prior to nitriding

The idea here is that by increasing the grain boundary area and dislocation density, enhanced diffusion could be expected in ultra-fine grained and nano-structured surface layers. That is to say that in this case shot peening can be useful only if performed with more severe parameters with respect to the usual ones, thus becoming a severe plastic deformation process.

It was shown that radio frequency plasma nitriding of stainless steel in combination with a pre-treatment by high pressure torsion results in an enhanced thickness of the nitrided layer and increased surface hardness [78]. The reason was mentioned to be the transformation of the coarse grained structure into a very fine grained one as a result of high pressure torsion. The same result was also reported by applying shot peening prior to plasma nitriding of stainless steel [79]. In

addition to dislocation density increment, in this case strain induced transformation of austenite to martensite had beneficial effects to provide faster diffusion. Application of shot peening to produce plastic deformation in a near surface layer of AISI 304 austenite stainless steel before plasma nitriding led to twice thicker nitrided layer than not peened specimens and improved hardness down to a deep region from the surface under the same plasma nitriding condition [80]. Wear resistance and corrosion behaviour of nitrided 316L austenitic steel can be enhanced by employing shot peening before gas nitriding [81].

Tong et al. [82] affirmed the possibility of performing nitriding at lower temperature (300 °C) for pure iron samples by generating nano-structured surface layers through a prior surface mechanical attrition (SMAT). The much depressed nitriding temperature is attributed to enhanced nitrogen diffusion in the nano-crystalline surface layer relative to the coarse grains. It was also found that a SMAT iron sample developed a nitrided layer twice as thick as that on a coarse-grained sample under the same gaseous nitriding conditions [83].

Kikuchi et al. [84] applied fine particle peening prior to gas nitriding of AISI 316 austenitic stainless steel notched specimens. The micro-hardness values for the nitrided only specimens were the same as that of untreated specimen. On the other hand much higher micro-hardness values were achieved by application of fine particle peening prior to nitriding. This hybrid treatment could also improve the fatigue strength as compared to nitriding only. However, the fatigue strength of double treated specimens was not substantially higher than fine particle peened specimens.

3.4 Conclusion

In the light of this literature review, it can be concluded that regarding the fatigue strength there are few studies carried out to clarify the effect of shot peening prior to nitriding. Indeed most of these studies concerned about the capability of this combination to increase nitriding diffusion layer and surface hardness. In the case of performing shot peening after nitriding the published result is somehow controversial. Minor, major and even no considerable improvement has been reported and it is not clear when someone could expect the best. Moreover, the effect of shot peening and nitriding combination on micro-structural changes was not widely investigated. Above all, it is yet not known which sequence of this combination leads to the best results if fatigue behaviour is concerned. It is therefore the purpose of this study to clarify these unexplored aspects of nitriding and shot peening combination.

Part II Experiment

4 Experimental Procedure

4.1 Introduction

The experimental procedure is described in detail in this chapter. In section 4.2 the material used in this study and its manufacturing process are introduced. The details of the used specimens including its geometry and extraction are also presented. Surface treatment including peening (conventional and severe) and nitriding and the processing parameters are described in section 4.3. The processing parameters such as media size, type, velocity, peening intensity, coverage, nitriding time and temperature are presented. Different experimental techniques used to study the effect of surface treatment on micro-structural refinement, mechanical characteristics and fatigue behaviour are given in section 4.4. These include optical, scanning and transmission electron microscopy, micro-hardness measurement, X-ray diffraction measurement of residual stress, roughness measurement and rotation bending fatigue test.

4.2 Material and specimens

4.2.1 Material

The material used in this study was high strength low alloy steel ESKYLOS6959 (equivalent to DIN 35NiCrMoV12-5 or AISI 4340). This class of steel is mostly used in the ground vehicle applications. Its chemical composition is summarized in Table 4-1. Mechanical properties evaluated through tensile test are the following: 878 MPa yield stress, 1010 MPa UTS and 17.7 % elongation.

Table 4-1. Chemical composition of steel grade 1.6959 used in this study (wt %).

C	Mn	Si	Cr	Mo	Ni	V	Fe
0.3-0.4	0.4-0.9	0.15-0.55	1-2	0.35-0.9	2.5-4.5	0.05-0.25	Balance

ESKYLOS6959 is a Chromium-Nickel-Molybdenum and Vanadium special pre-hardened alloyed steel suitable for production of components that are required to tolerate high stress condition while exhibiting good toughness characteristics. The material is obtained through a special ‘super clean’ manufacturing process, which allows an excellent level of micro-purity to be achieved. The manufacturing technology is electro-slag-melting which offers increased toughness, high micro-cleanness level, total isotropy of the material and very low segregation level. ESKYLOS6959 is supplied in the pre-hardened condition in two hardness ranges: 300-360 HB and 360-420 HB. The first range is suitable for the applications where the toughness is the

first aim and the second range is recommended for application where high levels of mechanical stresses and wear resistance are required.

4.2.2 Specimens

Rotating bending fatigue test specimens were machined from a forged 300 mm diameter bar according to the extraction map provided in Figure 4-1. The bar was quenched from 880 °C in water and then tempered at 635 °C for 5 hours. The extraction map was selected in such a way that ensures all specimens are similar in terms of their micro-structure. The specimen geometry is presented in Figure 4-2.

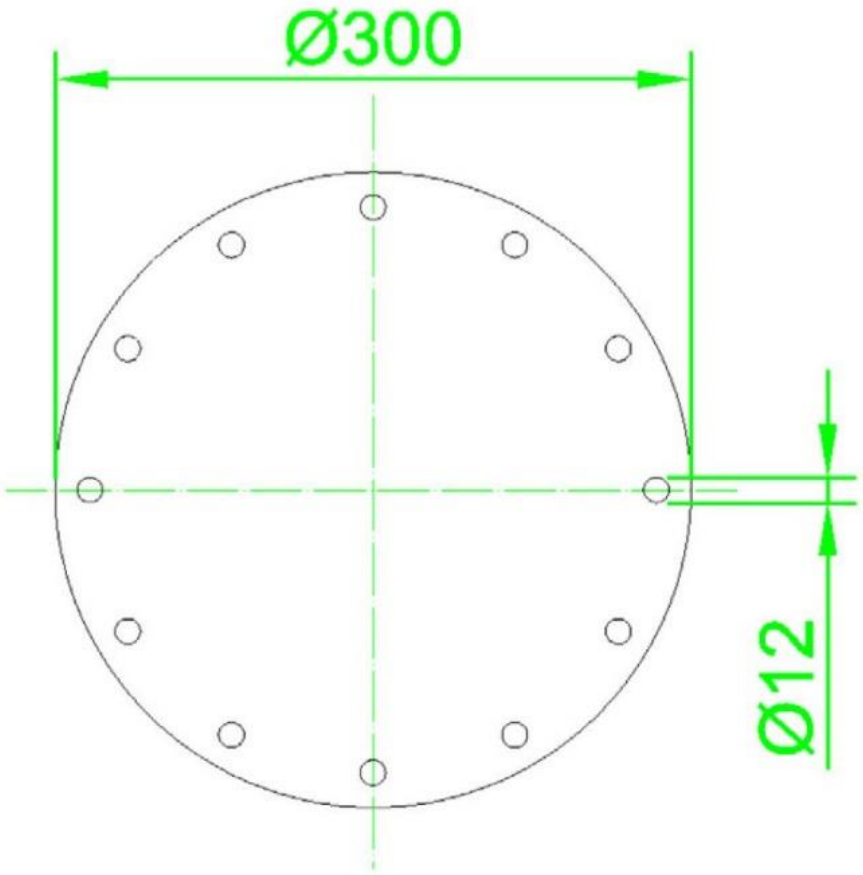

Figure 4-1. Extraction map of rotating bending fatigue specimens.

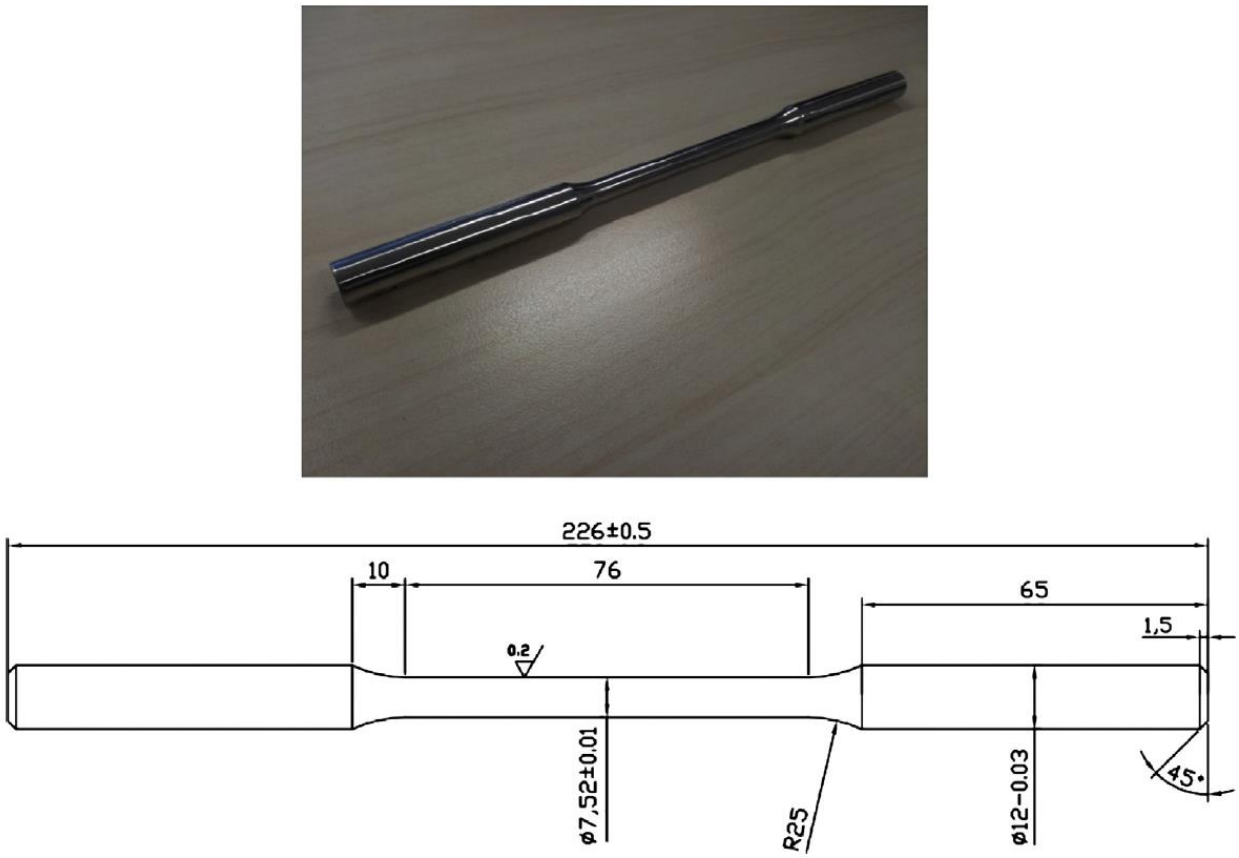

Figure 4-2. The detailed specimen geometry used for rotating bending fatigue test. All dimensions are given in mm.

4.3 Surface treatments

Six batches containing 12 specimens per each batch were prepared to obtain rotating bending fatigue limit in order to compare the effects of various surface treatments on the fatigue behaviour of the studied material. Different batches with corresponding naming conventions are classified in Table 4-2. The first group is as-received. Second and third groups were subjected to nitriding and severe shot peening respectively. Nitriding followed by severe shot peening was applied for the fourth batch. The fifth group was subjected to severe shot peening prior to nitriding. The last group was subjected to severe shot peening and then 50% shortened nitriding.

Table 4-2. Specimens naming convention.

Group Name	Description
AR	As-Received
N	Nitriding

SSP	Severe Shot Peening
N+SSP	Nitriding plus Severe Shot Peening
SSP+N	Severe Shot Peening plus Nitriding
SSP+NS	Severe Shot Peening plus 50% Shortened Nitriding

4.3.1 Severe shot peening

Standard cast steel shot, S230, using an air blast machine was employed to conduct severe shot peening. Based on the general requirement that cast steel shot should conform to, its hardness is in the range of 45-52 HRC [35] or 40-50 HRC [85]. Two lines were followed regarding the peening process. The first is a systematic study to reveal the effect of peening severity on grain refinement. Therefore, different level of coverage was applied to study conventional and severe peening. Specimens were treated by 100%, 200%, 650%, 1000% and 1300% coverage. The shot peening intensity measured on "Almen A" strip was 18A. Velocity of shots before impacting the target surface was 65 m/s. In the second line where combination of severe peening and nitriding was studied, peening was performed with the aforementioned intensity, media, velocity and 1000% coverage.

4.3.2 Nitriding

Gas nitriding was carried out in an industrial unit. Processing temperature and time were 510 °C and 15 h respectively. Nitriding potential was estimated to be 0.0056 $Pa^{-1/2}$. Indeed the standard cycle of nitriding in the industrial unit has been applied in the present study. However, duration was deliberately reduced by 50% for the last group of specimens while keeping temperature and the nitrogenous atmosphere the same.

4.4 Characterization

4.4.1 Micro-structural observation

Cross sections of the samples were prepared by a standard grinding, polishing and etching procedure [86]. Although many different etchants have been developed for Iron and Steels, Nital is the most commonly used [86]. Specimens for micro-graphs have been etched by Nital 2%. Microstructure observations were performed using optical microscopy and also Zeiss EVO50 scanning electron microscopy (SEM) with thermionic source and.

The microstructural evolution of the peened samples was characterized using a JEOL 2010F analytical microscope operated at 200 kV and FEI/Philips XL30 FEG ESEM at 20 kV. The cross-sectional TEM specimens were prepared from a mechanically thinned sample of 10-30 μm

thickness, made after cutting the peened part. In order to prevent the surface edge retention of steel plates, epoxy was used for preservation of deformed layers on the cut surfaces. After mechanical thinning, the glue was eliminated by annealing at 150 °C. The selected steel foils on a Cu grid were then ion-milled using Gatan PIPS with an ion accelerating voltage of 5 kV under an angel from 5°. The SEM observations were also conducted in this part to evaluate the grain refinement. 8% Nital was used as etchant (in this case) to reveal the final microstructure (i.e., lower bainite and/or tempered martensite) with the cell boundaries. All the SEM in this part observations were conducted under a magnification of X2000 for the better statistics. In this study, the microstructural refinement produced by shot peening process was characterized by the cell (and/or grain) size measurement and its evaluation was performed with Heywood's notation [87] (i.e., the diameter of the circle with an equal area of irregularly shaped cell or grain).

4.4.2 Micro-hardness measurement

Measuring hardness using indentation is based on the idea that if a hard object is pressed into the surface of softer material with enough force to produce an indentation, the indentation size will depend on the magnitude of applied force and the hardness of indented material [86]. If test conditions can be accurately controlled and reproduced a hardness number can be easily calculated from the applied load and the projected area of impression.

Micro-hardness measurements have been performed on specimen's section respectively. A diamond Vickers indenter with pyramidal shape was used. An outstanding advantage of the Vickers diamond pyramid hardness test is that one continuous scale is used to test all materials regardless of their hardness [86]. In performing the test, the load must be applied smoothly without impact and held in contact for 10-15 s. after removal of the load both impression diagonal are measured and the average value is used to calculate HV (Vickers hardness) by the following equation:

$$HV = \frac{2L\sin(\alpha/2)}{d^2} = \frac{1.8544L}{d^2} \qquad (4\text{-}1)$$

Where d is the mean diagonal in mm, L is the load in kgf and α is the face angle of the Vickers indenter (136°). In the present work maximum force of 100 gf has been applied. The load was applied gradually at a constant 0.1 Ns^{-1} rate with a dwell time of 15 s. Three measurements were performed at each depth and averaged to account for measurement errors and material's heterogeneity. The resultant data scattering was not more than 10%.

4.4.3 XRD measurement of residual stress

XRD technique is used to determine the distance between crystallographic planes (d-spacing); thus its application is limited to crystalline, poly-crystalline and semi-crystalline materials. When a material is in tension, the d-spacing increases and when a material is in compression the d-spacing decreases [35]. The presence of residual stress in a material produces a shift in the X-ray diffraction peak angular position that is directly measured by detector.

Figure 4-3 shows the diffraction of a monochromatic beam of X-rays at a high diffraction angle (2θ) from the surface of a stressed sample for two orientations of the sample relative to the x-ray beam. The angle ψ, defining the orientation of the sample surface, is the angle between the normal of the surface and the incident and diffracted beam bisector, which is also the angle between the normal to the diffracting lattice planes and the sample surface.

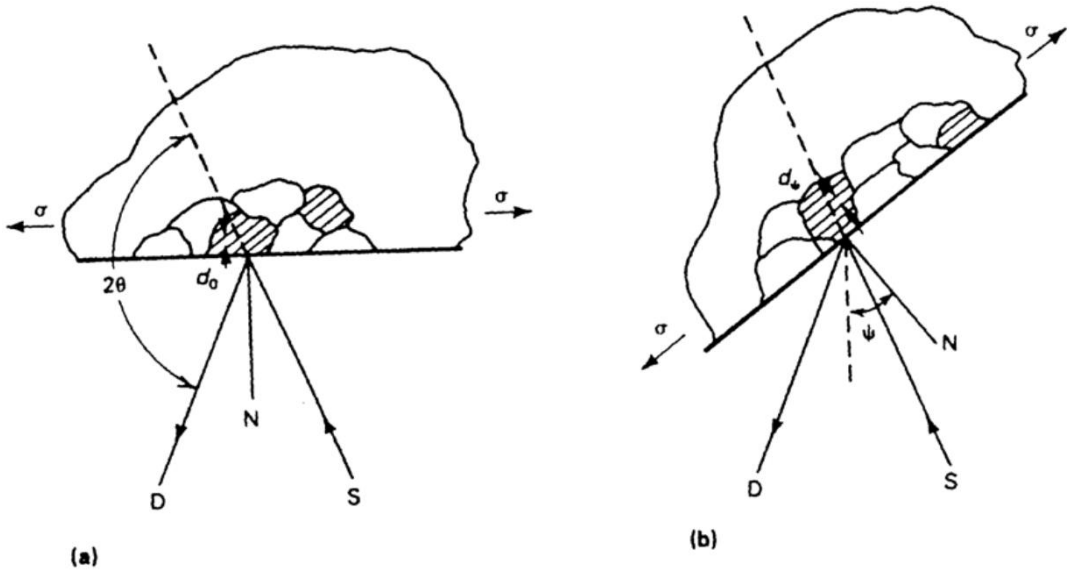

Figure 4-3. (a)ψ = 0. (b) ψ = ψ (sample rotated through some known angle ψ). D, x-ray detector: S, x-ray source; N, normal to the surface [88].

Diffraction occurs at an angle 2θ is defined by Bragg's Law:

$$n\lambda = 2d\sin\theta \qquad (4\text{-}2)$$

Where n is an integer denoting the order of diffraction, λ is the x-ray wavelength, d is the lattice spacing of crystal planes, and θ is the diffraction angle. For the monochromatic x-rays produced

by the metallic target of an x-ray tube (normally chromium for steel), the wavelength is known to 1 part in 10^5. Any change in the lattice spacing, d, results in a corresponding shift in the diffraction angle 2θ.

Figure 4-3 a shows the sample in the $\psi = 0$ orientation. The presence of a tensile stress in the sample results in a Poisson's ratio contraction, reducing the lattice spacing and slightly increasing the diffraction angle, 2θ. If the sample is then rotated through some known angle ψ (Figure 4-3 b), the tensile stress present in the surface increases the lattice spacing over the stress-free state and decreases 2θ. Measuring the change in the angular position of the diffraction peak for at least two orientations of the sample defined by the angle ψ enables calculation of the stress present in the sample surface lying in the plane of diffraction, which contains the incident and diffracted x-ray beams. To measure the stress in different directions at the same point, the sample is rotated about its surface normal to coincide the direction of interest with the diffraction plane.

Because only the elastic strain changes the mean lattice spacing, only elastic strains are measured using x-ray diffraction for the determination of macro-stresses. When the elastic limit is exceeded, further strain results in dislocation motion, disruption of the crystal lattice, and the formation of micro-stresses, but no additional increase in macroscopic stress. Although residual stresses result from non-uniform plastic deformation, all residual macro-stresses remaining after deformation are necessarily elastic. The residual stress determined using X-ray diffraction is the arithmetic average stress in a volume of material defined by the irradiated area, which may vary from square centimeters to square millimeters, and the depth of penetration of the x-ray beam. The linear absorption coefficient of the material for the radiation used governs the depth of penetration, which can vary considerably. However, in iron, nickel, and aluminum-base alloys, 50% of the radiation is diffracted from a layer approximately 0.005 mm deep for the radiations generally used for stress measurement. This shallow depth of penetration allows determination of macro and microscopic residual stresses as functions of depth, with depth resolution approximately 10 to 100 times than possible using other methods.

Although in principle virtually any inter-planar spacing may be used to measure strain in the crystal lattice, availability of the wavelengths produced by commercial X-ray tubes limits the choice to a few possible planes. The choice of a diffraction peak selected for residual stress measurement impacts significantly on the precision of the method. The higher is the diffraction angle, the greater is the precision. Practical techniques generally require diffraction angles, 2θ, greater than 120°.

X-ray diffraction stress measurement is confined to the surface of the sample. Electro-polishing is used to expose new surfaces for subsurface measurement. In the exposed surface layer, a condition of plane stress is assumed to exist. That is, a stress distribution described by principal stresses σ_1 and σ_2 exists in the plane of the surface, and no stress is assumed perpendicular to the surface, $\sigma_3 = 0$. However, a strain component perpendicular to the surface ε_3 exists as a result of the Poisson's ratio contractions caused by the two principal stresses (Figure 4-4).

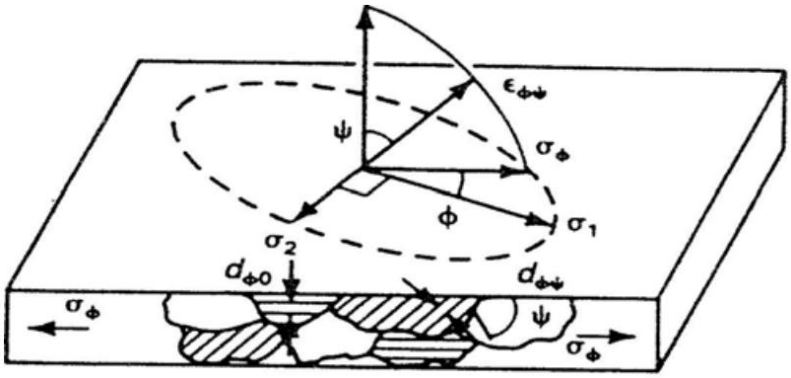

Figure 4-4. Plane-stress elastic model [4].

If $d_{\varphi\psi}$ is the spacing between the lattice planes measured in the direction defined by φ and ψ, the strain can be expressed in terms of changes in the linear dimensions of the crystal lattice:

$$\varepsilon_{\phi\psi} = \frac{\Delta d}{d_0} = \frac{d_{\phi\psi} - d_0}{d_0} \qquad (4\text{-}3)$$

Where d_0 is the stress free lattice spacing. Because of elastic anisotropy, the elastic constants in the (hkl) direction commonly vary significantly from the bulk mechanical values, which are an average over all possible directions in the crystal lattice. Considering plane stress formulation the lattice spacing for any orientation is given:

$$d_{\phi\psi} = \left[\left(\frac{1+\upsilon}{E}\right)_{(hkl)} \sigma_\varphi d_0 \sin^2\psi\right] - \left[\left(\frac{\upsilon}{E}\right)_{hkl} d_0\left(\sigma_1 + \sigma_2\right) + d_0\right] \qquad (4\text{-}4)$$

Equation (4-4) describes the fundamental relationship between lattice spacing and the biaxial stresses in the surface of the sample. The lattice spacing $d_{\varphi\psi}$, is a linear function of $\sin^2\psi$. Stress σ_φ can be obtained by the following equation:

$$\sigma_\phi = \left(\frac{1+\upsilon}{E}\right)_{(hkl)} \frac{1}{d_0}\left(\frac{\partial d_{\varphi\psi}}{\partial \sin^2\psi}\right) \qquad (4\text{-}5)$$

The three most common methods of X-ray diffraction residual stress measurement, the single-angle, two-angle, and $\sin^2\psi$ techniques, assume plane stress at the sample surface and are based on the fundamental relationship between lattice spacing and stress given in equation (4-4). The $\sin^2\psi$ technique has been adapted in the present work. In this method lattice spacing is determined for multiple ψ tilts, a straight line is fitted by least squares regression as for instance shown for a typical shot peened sample in Figure 4-5, and the stress is calculated from the slope of the best fit line using equation (4-5).

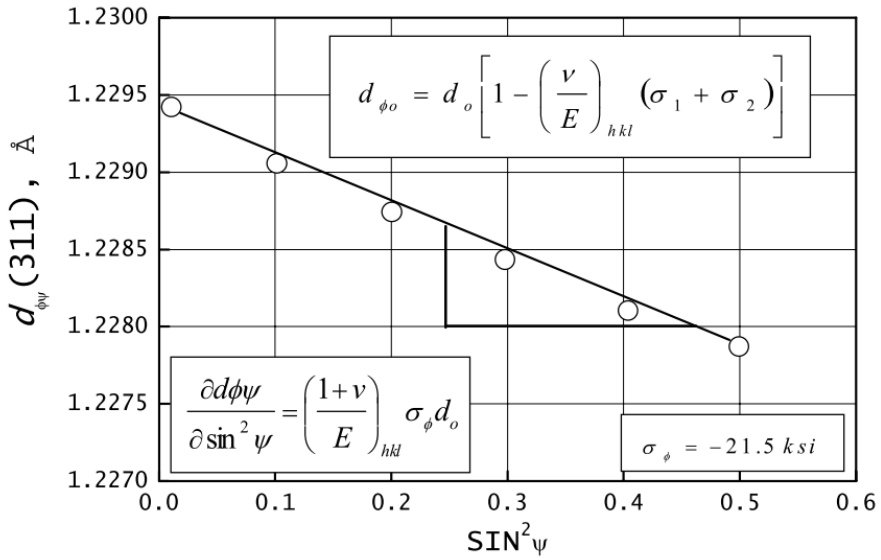

Figure 4-5. A d(311) versus sin2ψ plot for a shot peened 5056-O aluminum alloy having a surface stress of -148 MPa [88].

X-Ray Diffraction analysis of the surface layer in the treated specimens was performed using an AST X-Stress 3000 X-ray diffractometer (radiation Cr Kα, irradiated area 3.14 mm^2, $\sin^2\psi$ method, diffraction angle (2θ) ∼156 scanned between −45 and 45). Figure 4-6 shows the specimen during XRD analysis of residual stress. In depth measurements have been carried out step by step by removing a very thin layer of material (0.01–0.02 mm) using an electro-polishing device in order to obtain the in-depth profile of residual stresses. A solution of Acetic acid (94%) and Perchloric acid (6%) has been used for electro-polishing. On each specimen, material removal has been carried on up to the depth showing insignificant compressive residual stress values. Figure shows the sample under X-ray diffraction set up.

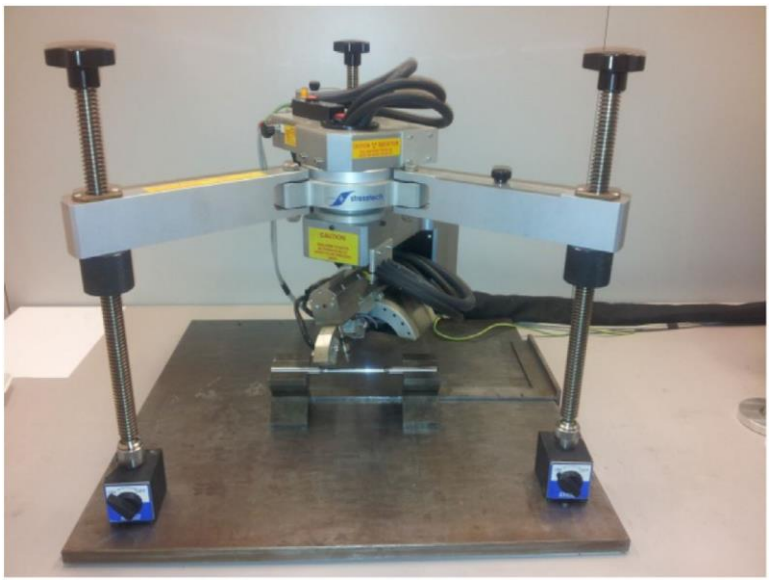

Figure 4-6. Specimen during XRD analysis of residual stress.

4.4.4 Roughness measurement

Surface roughness, often shortened to roughness, is a measure of the texture of a surface. It is quantified by the vertical deviations of a real surface from its ideal form. If these deviations are large, the surface is rough; if they are small the surface is smooth. Roughness is typically considered to be the high frequency, short wavelength component of a measured surface. Roughness plays an important role in determining how a real object will interact with its environment. Rough surfaces usually wear more quickly and have higher friction coefficients than smooth surfaces. Roughness is often a good predictor of the performance of a mechanical component, since irregularities in the surface may form nucleation sites for cracks or corrosion. On the other hand, roughness may promote adhesion.

A Mahr profilometer PGK, that is an electronic contact instrument, equipped with MFW-250 mechanical probe and a stylus with tip radius of 2 μm was used to trace the surface profiles of treated specimens. The acquired signal was then elaborated by Mahr Perthometer Concept 5 software [89] to obtain the standard roughness parameters. Surface roughness data were obtained by performing three measurements along three distinct 0.8 mm long surface axial lines of each individual specimen to consider the variability of surface roughness by location. The final reported experimental surface roughness values in the present work are the mean value of the three performed measurements. Figure 4-7 shows the specimen during surface roughness measurement.

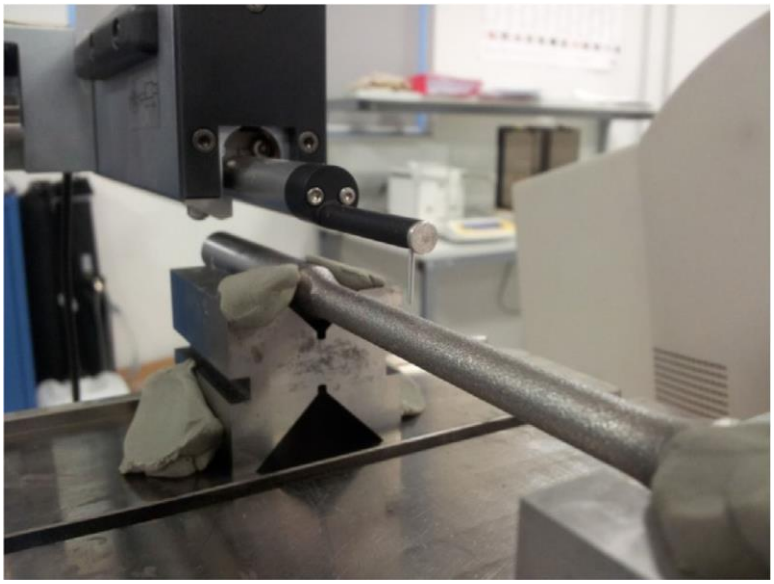

Figure 4-7. The specimen during surface roughness measurement.

A roughness value can either be calculated on a profile (line) or on a surface (area). The profile roughness parameters (R_a, R_q, R_t,...) are more common. The surface roughness parameters of all treated specimens were calculated based on the definition of ISO 4287 [90]:

$$R_a = \frac{1}{n}\sum_{i=1}^{n}|y_i| \qquad (4\text{-}6)$$

$$R_q = \sqrt{\frac{1}{n}\sum_{i=1}^{n}y_i^2} \qquad (4\text{-}7)$$

$$R_t = \max y_i - \min y_i \qquad (4\text{-}8)$$

Each of the above formulas assumes that the roughness profile has been filtered from the raw profile data and the mean line has been calculated. The roughness profile contains n ordered, equally spaced points along the trace, and y_i is the vertical distance from the mean line to the i^{th} data point. Height is assumed to be positive in the up direction, away from the bulk material.

4.4.5 Fatigue test

Approaches to characterizing the fatigue strength of a material must statistically account for the scatter in fatigue data. This scatter is generally due to a variety of factors, some more controllable than the others. Some of the relatively controllable factors include inconsistencies in

surface finish, deviations in specimen alignment, differences in applied loading conditions, and inconsistent residual stresses. These sources of scatter are generally mitigated through proper experimental procedures. However, scatter in fatigue data is still observed due to the random nature of the microstructure of each specimen, which produces slightly different conditions for crack initiation and growth within each specimen. In the high cycle regime, fatigue life is dominated by the crack initiation phase, which is heavily dependent on microstructural phenomenon related to localized conditions. Thus, the scatter in fatigue data tends to be magnified in the high cycle regime. This behavior has been confirmed by numerous researchers through the years [91,92]. Based on these and similar findings, any experiment designed to test fatigue strength in the high cycle regime must account for significant scatter in results. Currently, a variety of test approaches have been used to estimate the fatigue strength of a material. In general, these methods allow a means to deal with the scatter in fatigue data and provide an estimate for the median fatigue strength at a specified number of cycles.

The staircase method was selected as one of the most promising methods for analysis of high cycle fatigue data for several reasons. To start, the test is simple in terms of test protocol. It is also widely used in industry and academia and has been a part of testing guidance for some time. The test has also proven to be extremely accurate in characterizing the mean fatigue strength at a specified number of cycles using very few specimens. Although the analysis methods were developed in the 1950s for explosives testing, there has been a flurry of recent activity from 1998 to the present in exploring the ability of the staircase test to characterize the scatter in fatigue strength.

The staircase (or up-and-down) test was first analyzed by Dixon and Mood in 1948 [93]. They presented a means of analyzing data generated in such a fashion (then called the “up-and-down” method) [93]. Their objective was to analyze results from explosives tests conducted at various heights. Tests were conducted at an initial height h_0, and if the weight exploded then the height for the next test would be lowered by an interval, or it would be raised an interval if the weight did not explode.

In a staircase test, specimens are tested sequentially, with the first specimen tested at an initial stress level, typically the best guess for median fatigue limit estimated from either experience or preliminary S-N data. The stress level for the next specimen is increased or decreased by a given interval depending on whether the first specimen survives or fails. This process is continued until all the specimens allocated for the experiment have been used. Typically, the step size between adjacent stress levels is held constant (approximately equal to the standard deviation of fatigue strength), in which case the statistics of Dixon and Mood may be applied directly to estimate mean and standard deviation of the fatigue strength [94]. Even though the true standard deviation in fatigue strength is one of the unknowns, Dixon notes that it is not too important if the interval is actually incorrect with respect to the true standard deviation by as much as 50%. In fact, tests conducted with non-uniform spacing may be more statistically efficient than uniform spacing;

however, the analysis becomes much more tedious and the equations and tables derived for uniformly spaced tests are no longer useful [95]. In such a constant-step protocol, there are three parameters which the researcher must specify: (1) the starting stress, S_{init}, (2) the step size, s, and (3) the number of specimens, N.

Such a protocol was popularized for the application of fatigue strength testing by Little in the 1970s [96]. Discussion of Dixon-Mood's approach will be couched in fatigue-related terms rather than their original explosives testing terminology. Dixon and Mood noted several advantages for the use of the staircase method. First, the staircase test by its very nature tends to concentrate data near the mean, which increases the accuracy with which the mean can be estimated. Another advantage is the relative simplicity of the statistical analysis of staircase data.

Accordingly, in the present experiments, rotating bending fatigue tests (stress ratio R = −1) have been carried out at room temperature with a nominal frequency of 20 Hz for all batches. Staircase procedure considering 10 MPa as step was followed to elaborate data and to calculate the fatigue limit. Rotating bending fatigue test machine is presented in Figure 4-8.

Figure 4-8. Rotating bending fatigue test machine used in the present work.

Part III Numerical Framework

5 Finite element simulation

5.1 Introduction

Finite element simulation of shot peening is presented in this chapter. While most of the existing models simulate peening for full coverage (100%), the aim of the proposed procedure is to capture the effects peening such as roughness and residual stress evolution during peening from full to higher coverage i.e. conventional to severe peening. Chronological evolution of shot peening finite element simulation is presented in section 5.2. Finite element model of single impact is described in section 5.3. The radius of a single indentation is an important parameter in order to build the multiple impacts peening simulation able to represent a real peening condition. Simulation of real peening process is described in section 5.4.

5.2 Chronological evolution of shot peening FE simulation

“There is still a huge lack of knowledge. We are only just entering the area of mechanics of shot peening.” Al-Hassani used these words at the end of his analytical analysis of a target impinged upon by a single sphere, three decades ago, to emphasize on the complexities of the process involving many disciplines of static and dynamic elasticity and plasticity [97]. At that era shot peening was not known to everyone and also very limited works and researches were available. His simple formulas and those published by Al-Obaid [98,99] were the first relations which correlated depth of plastic zone and residual stress to density of shot, velocity of impact, thickness and hardness of the target.

Noteworthy differences of dent shape and residual stress in static and dynamic indentation test [100] demonstrated that dynamic effects of shot peening cannot be ignored. This issue increases the complication of analytically analyzing the process. Numerical methods such as finite element, thanks to rapid progress of computer power in the last decade, have been efficiently utilized for analyzing of involved process. Simulation of one spherical shot impingement on an elasto-plastic target has been widely used for determination of the shot peening induced residual stress [101–106]. A cube of 7R width (R is the shot radius.), 4R height and 5R breadth [101] and a cylinder of 8R radius and 3R height [106] have been proposed as suitable geometries of an arbitrary target upon which impingement of one shot takes place. Although these single shot impingement models could not simulate a realistic peening, they drew a preliminary good perception of shot velocity and size effects on plastic zone development, its growth and unloading residual stress. Examination of twin spherical indentation using the finite element model proposed by Meguid [107] revealed the significant effect of separation distance between two shots upon residual stress field which in turn introduced multiplicity of shots as a serious topic to be considered in finite element simulations. Situation of a large number of identical shots impinging a metallic target has been envisaged by symmetry cell approach [108]. The dimensions of the proposed symmetry cell were C×C×H where C is one half of separation

distance between adjacent shots and could be considered as representative of the coverage in the peening. Shot peening of the symmetry cell can be regarded as the impingement of identical shots with a symmetry layout inside each row. These rows were further combined in series of four rows that in each impingement upon the target surface one single shot comes into contact with one corner of the symmetry cell. A general realistic residual stress induced by shot peening has been successfully and efficiently calculated [109] by application of the four impacts symmetry cell combined with the idea of averaging the nodal residual stresses at each depth. Using another shot sequence, Majzoobi et al. [110] developed a nine impacts symmetry cell model and studied the variation of in depth residual stress profile in different points of the target. Increasing the number of impacts, they found that a uniform state of in depth residual stress could be achieved in different points of target at particular number of shots. However, this particular number of shot impact is certainly a problem dependent parameter and would change for different peening conditions. More recently, a random location of shots in finite element model has been utilized to simulate shot peening [111,112]. Good agreement between simulated and experimentally measured residual stress distribution affirmed that random locations for shot can be a good alternative for simulation of more realistic shot peening process. Figure 5-1 summarizes the evolution of the shot peening finite element simulation.

A brief look on the way in which numerical simulation goes through as compared with that of practical shot peening, discloses a lack of straightforward terminological correlation between simulation and practice. Numerical simulators are presenting their own results in terms of shot velocity and size while shot peening industries are more interested in other parameters. There are two important practical parameters that have been universally accepted and adopted by engineers in order to ensure repeatability of the process: I) intensity and II) coverage. Intensity is an index of transferred kinetic energy from stream of shots to the target and coverage indicates the amount of target surface that is treated by shots. If a reliable selection of shot peening parameters to meet a given function is supposed to be a mission of numerical simulation, there is no escape but incorporation of intensity and coverage into numerical simulation of shot peening.

A procedure to relate the values of Almen-scale, which is indicator of intensity, to the residual stresses in metal parts have been established [41]. Such a correlation can guide the designer towards the optimal selection of process parameters while minimizing the cost of necessary experimental assessments. Such an incorporation however, for the other important parameter i.e. coverage has not been investigated yet. In fact most of the 3D multiple impact simulation models, recently developed, did not focus on coverage but on the general understanding of how the stress state develops during successive impacts.

Coverage, the most important measurable variable of shot peening, the most important parameter in the so called severe shot peening and one of the most affective parameters on fatigue life of treated parts, either improvement or deterioration, is at the same time the most missing one in the

finite elements simulations. It is therefore demanding to characterize a suitable random simulation to accommodate coverage.

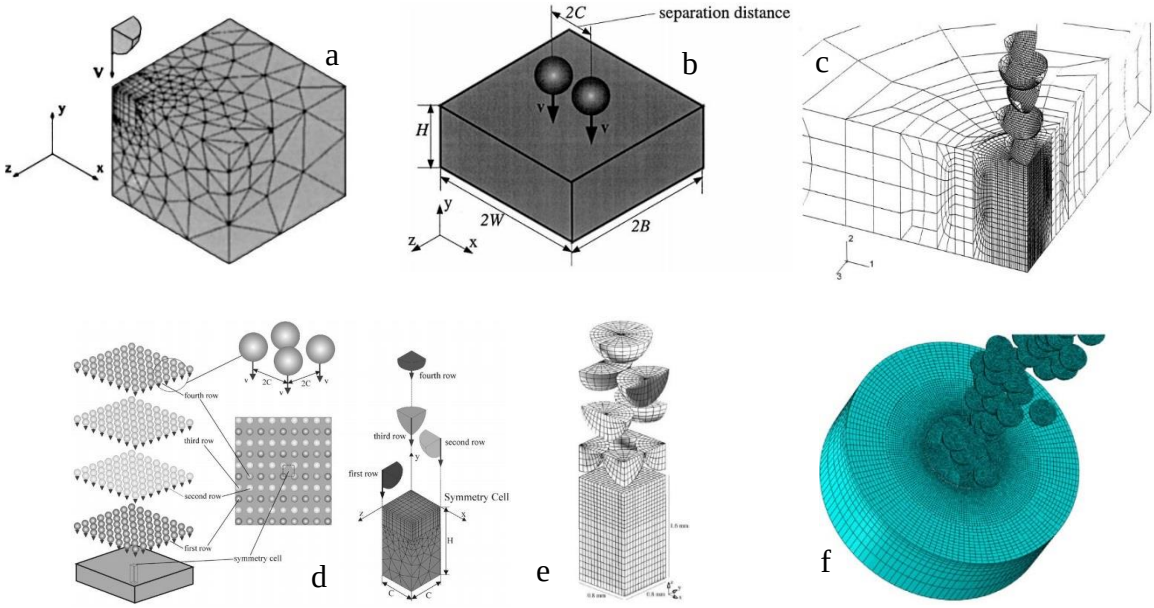

Figure 5-1. Evolution of shot peening finite element simulation a[101] , *b*[107] , *c*[41] , *d*[108] , *e*[110] , *f*[112].

5.3 FE Model of single impact

Two dimensional axisymmetric model of a target impinged upon by a single impact was constructed using the commercial finite element code Abaqus explicit 6.10-1 [113]. After some preliminary analysis the dimension of the target was chosen to be 5R×5R, where R is the shot radius, to ensure boundary conditions do not interfere with elasto-plastic deformation occurring in the surface layer. Only the lower half of the shot was modeled to save the computation time. However, its density was doubled such that it conveys the same kinetic energy of the full shot. CAX4R [113] which is a 4-node bilinear axisymmetric quadrilateral element with reduced integration and hourglass control, was used to discretize target and shot. Finer mesh was exploited in the contact region where higher deformation is expected. To simulate shot and target interface contact elements were introduced using the penalty algorithm with no limit on shear stress, infinite elastic slip stiffness and isotropic coulomb friction coefficient of 0.2. Axisymmetric boundary condition was applied to the corresponding axis of shot and target. Target's bottom was constrained against its all degree of freedom. Initial velocity was applied on

all finite element nodes that shot consists of. Figure 5-2 shows the finite element mesh along with the applied initial and boundary condition.

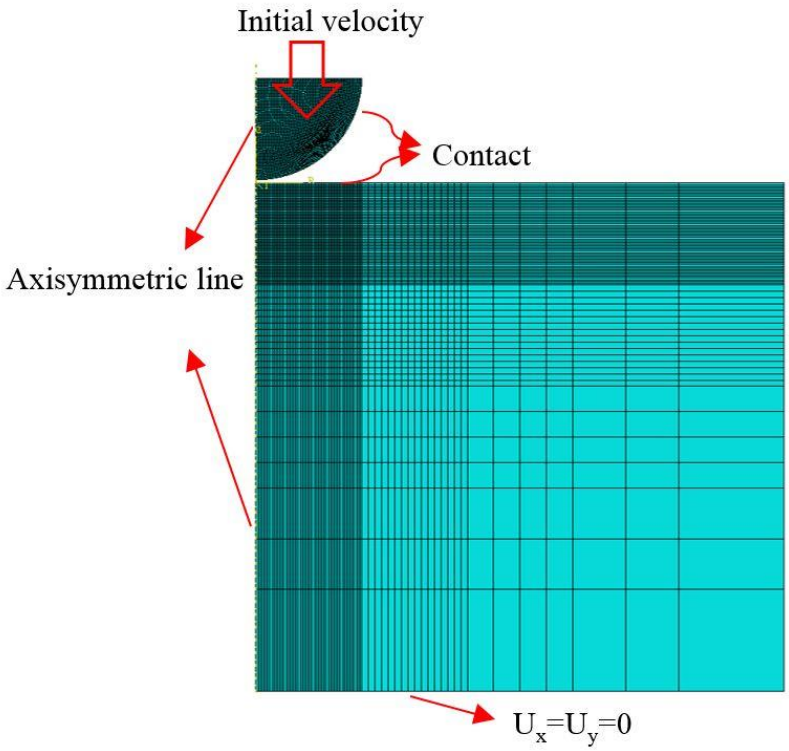

Figure 5-2. Finite element mesh along with applied initial and boundary condition.

5.3.1 Material behavior

5.3.1.1 Shot

Standard cast steel shot, S230, was employed in the experiment. Based on the general requirement that cast steel shot should conform to, its hardness should be in the range of 45-52 HRC [35] or 40-50 HRC [85]. Therefore, an elastic perfectly plastic behavior was considered to simulate shot behavior. Mass density ρ=7850 kg/m^3, Elastic modulus E=210 GPa and Poission's ratio υ=0.3 were used. Yield stress of cast steel shot was assumed to be approximated by its ultimate tensile strength (UTS). Based on the hardness range for cast steel and well-known hardness _UTS conversion, yield stress Y=1550 MPa was applied for the shot corresponding to the performed experiment. However, in order to study the effect of shot hardness on the refinement range of 1550-2500 MPa was also studied.

5.3.1.2 Target

The target is high strength low-alloy steel AISI 4340. High strain rate deformation (up to 10^5 1/s) occurs in shot peening. It was shown that strain rate plays a major role in dictating the level and distribution of the residual stress field and the induced plastic strains in shot peening [108]. Therefore, it is crucial to apply a constitutive behavior able to reflect a correct hardening not only as a function of plastic strain but also the strain rate to capture the rate sensitivity of the flow stress. Johnson-Cook constitutive equation [114] originally tested and proposed for metallic materials including 4340 steel was applied for the target. It expresses the flow stress as a function of equivalent plastic strain, strain rate and temperature by the following relation:

$$\sigma_y = \left[A + B\varepsilon_p^n\right]\left[1 + C\ln\frac{\dot{\varepsilon}_p}{\dot{\varepsilon}_0}\right]\left[1 - \left(\frac{T - T_{room}}{T_{melt} - T_{room}}\right)^m\right] \quad (5\text{-}1)$$

Where ε_p is equivalent plastic strain, $\dot{\varepsilon}_p$ and $\dot{\varepsilon}_0$ is the applied and reference deformation rate, T, T_{room} and T_{melt} are applied, reference and melting temperature, A is the initial yield stress, B and n are constants describing hardening coefficient and exponent respectively, C and m are also constants describing the flow stress sensitivity to strain arte and temperature. Table 5-1 represents the Johnson-Cook parameters for AISI 4340 [114]. It should be noted, as shot peening is widely accepted to be a cold working process the dependency of flow stress to temperature has been neglected in the present simulation.

Table 5-1. Johnson-Cook parameters for AISI 4340.

A (MPa)	B (MPa)	n	C	m	$\dot{\varepsilon}_0$ (1/s)	T_{melt} (K)
792	510	0.26	0.014	1.03	1	1793

5.3.2 Media size and velocity

Standard cast steel shot, S230, was employed in the experiment. Its nominal diameter is 0.6 mm. For the shot corresponding to the performed experiment the same diameter was applied. However, in order to study the effect of media size on the refinement, range of 0.2-1.2 mm was also studied. Experiment was conducted by shot velocity of 65 m/s. For the simulation corresponding to the performed experiment the same initial velocity was applied. Moreover, velocity range of 20-200 m/s was also simulated to study the effect of velocity on refinement.

5.3.3 Mesh sensitivity

Mesh convergence study was conducted to ensure the finite element result is not affected by the applied element size. Since equivalent plastic strain is the output of the FE simulation and the input for the subsequent dislocation density model, mesh convergence study was conducted on this parameter. In-depth variation of equivalent plastic strain (PEEQ) for different element size is shown Figure 5-3. The results are converged for 5 µm and smaller element size. Therefore, 5 µm was chosen as the element size in both target and shot in the contact region.

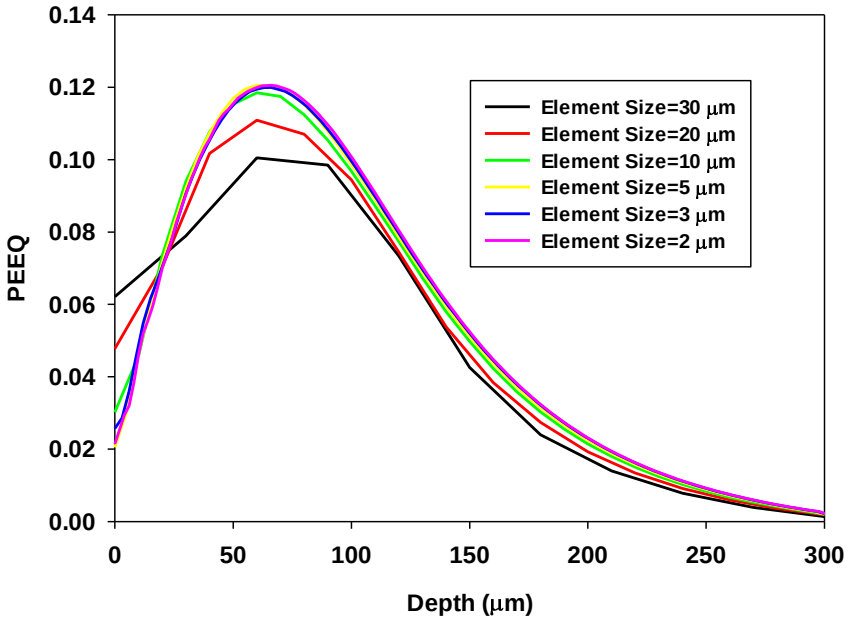

Figure 5-3. Mesh sensitivity analysis.

5.3.4 Damping

In order to prevent residual oscillations material damping was introduced into the model using equation (5-2) where C is damping matrix, M is mass matrix and K is stiffness matrix. Coefficient α was calculated by equation (5-3) where ω_0 is initial frequency and ζ is damping ratio (ζ <1). The value ζ =0.5 which is adequate for rapid damping of low frequency oscillations [108] was used in the model. ω_0 was estimated by equation (5-4) where E is the target's Young Modulus, ρ is its density and h is its height. After some trial runs it was observed that a mass proportional damping is satisfactory for vanishing residual oscillations. Therefore, the stiffness proportional damping factor, β was set to zero.

$$C = \alpha M + \beta K \qquad (5\text{-}2)$$

$$\alpha = 2\omega_0\zeta \quad (5\text{-}3)$$

$$\omega_0 = \frac{2\pi}{h}\sqrt{\frac{E}{\rho}} \quad (5\text{-}4)$$

5.4 FE Model of multiple impacts

The basic principles of 3D simulation, material behavior, initial and boundary condition and contact properties are similar to that of 2D simulation. The main difference is that a target area is going to be covered by shots. Accordingly the most important challenge in 3D simulation of multiple impacts or in another word simulation of an actual shot peening is to represent a realistic and yet not computationally demanding evolution of coverage. It was discussed in detail [112] that the available models of shot peening often fail to simulate a full coverage condition. Finding a reasonable strategy for shot positioning is of great importance to address this challenge. Two strategies were examined in the present work: Complete random and guided random positioning of shots.

5.4.1 Complete random positioning of shots

The correlation between the coverage and the ratio of the impacted area to the total area was proposed [46] to have and Avrami type [47] behavior. Coverage percent (C%) in this case is expressed as function of the ratio of the indented area to total (A_r) are by equation (5-5). A_r can be calculated by equation (5-6) where N is the number of impact, r is the radius of indentation by a single collision and R_{target} is the radius of the treated area that should be covered by shots.

$$C\% = 100\left(1 - e^{-A_r}\right) \quad (5\text{-}5)$$

$$A_r = \frac{N\pi r^2}{\pi R_{target}^2} \quad (5\text{-}6)$$

By adopting a complete random positioning of shots and varying the radius of treated area one can find how big the treated are should be in order to reflect a realistic evolution of coverage. Coverage evolution for three different radius of target area is shown in Figure 5-4 as function of impact number.

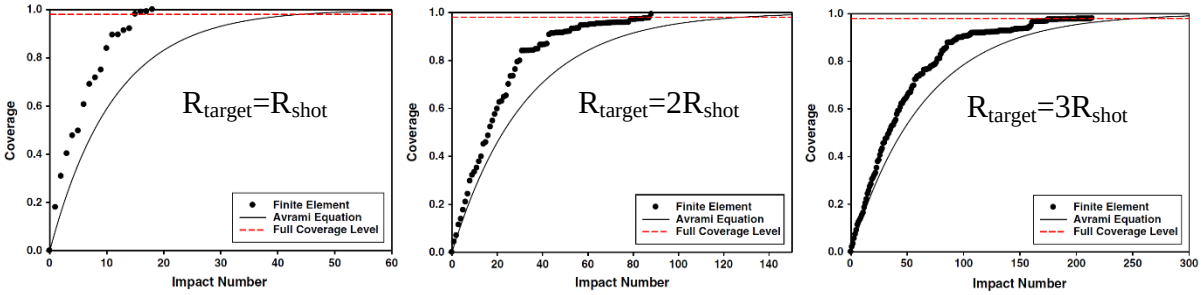

Figure 5-4. Coverage evolution for three different radius of target area.

The error between predicted number of impact for full coverage by Avrami equation and the one obtained by FE simulation was 66% for $R_{target}=R_{shot}$, 31% for $R_{target}=2R_{shot}$ and 16% for $R_{target}=3R_{shot}$. This suggests the amount of error would be less than 10% if the radius of $R_{target}=4R_{shot}$ is considered for the treated area. Expressing the finding in terms of indentation radius would be the radius of treated area should be at least 10 times larger than the radius of a single indentation in order to have a realistic evolution of coverage in the simulation. Referring to equation (5-5), this means the number of impact needed to reach full coverage would be around 400. The cost of computation will be very high, bearing in mind that this number of impact is needed only for full coverage. Therefore, in order to simulate high coverage peening which is the aim of this study, let's say for 1000% coverage, 4000 number of impact is needed. The bottom line is complete random positioning of shot might come up with a realistic evolution of coverage but computational cost would be extremely high.

5.4.2 Semi-random positioning of shot

In this strategy random positioning of shot is applied but somewhat in a steered manner. A constraint was added to the positioning such that the impact center of subsequent impact is not allowed to occur in the area that had been treated by the pervious impacts. That does not mean there is no overlap as for instance if the impact center of the incoming shot is randomly located close to the border of previously treated area there would be some area that is treated more than one before obtaining full coverage. However, the numerical effort needed to simulate decreases considerably. Yet, a reasonably realistic evolution of coverage is captured in the simulation. The issue that should be addressed in this approach is finding an appropriate size of the treated area. In order to do that the size of treated area was enlarged step by step and the semi-random positioning of shots was applied for peening simulation. Figure 5-5 shows in-depth distribution of compressive residual stress for different treated areas. Compressive residual stress in each depth is the nodal average of residual stress for all the nodes at that depth. It can be observed that residual stress distribution is converged for $R_{target}=5r_{single\ indentation}$. Full coverage in this approach was obtained by smaller treated area with respect to the complete random positioning of shots

and with considerably lower number of impacts (42 in this particular case). Finite element model of 3D simulation of shot peening is shown in Figure 5-6.

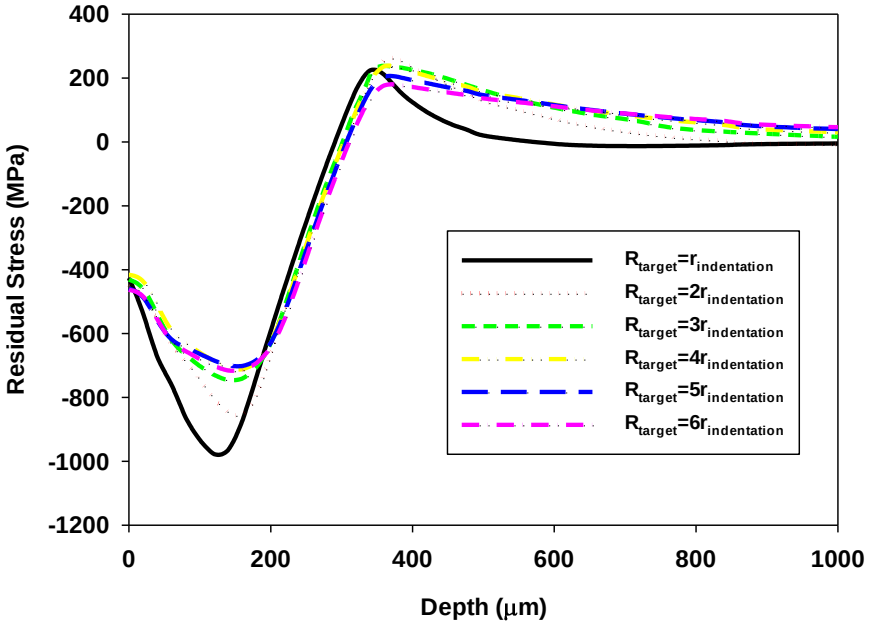

Figure 5-5. In-depth distribution of compressive residual stress for different treated areas.

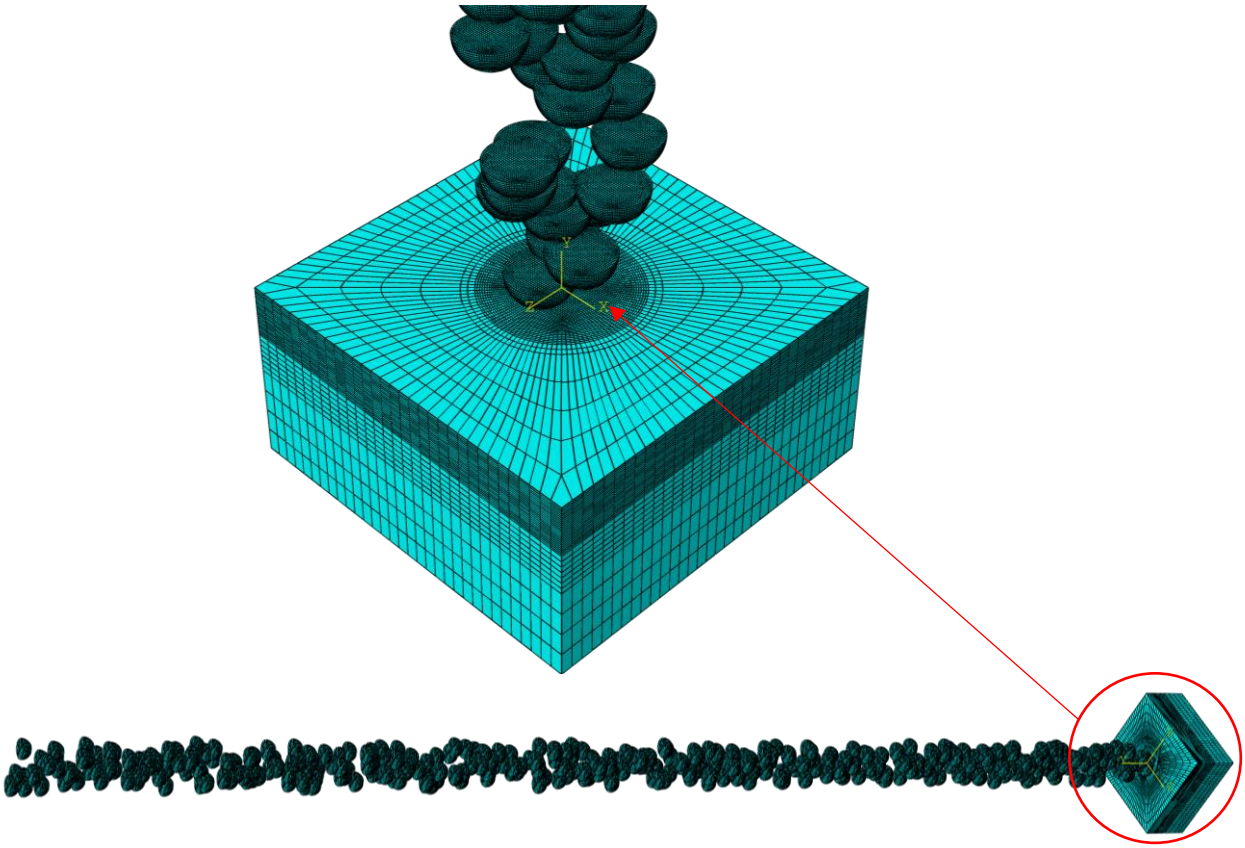

Figure 5-6. Finite element model of 3D simulation of shot peening.

5.5 Conclusion

A numerical methodology was proposed in this chapter to simulate severe shot peening. An important consideration for a successful simulation of severe peening is finding an appropriate method to accommodate coverage into the finite element model. In the proposed strategy radius of a single indentation is obtained by simulating one impact. It was demonstrated that in order to have a complete random positioning of shots and big enough target surface to capture multiple impacts effects, 4000 number of impact is needed for example for 1000% coverage. Computational cost is extremely high in this case. Therefore, semi-random positioning of shots was proposed. It was shown that this approach is able to decrease computational cost around 10 times and yet to represent a realistic severe shot peening process.

6 Dislocation density model

6.1 Introduction

The most commonly accepted type of models of grain refinement due to large strain, particularly under SPD conditions, are based on the notion that a dislocation cell structure, which forms already in the early stages of plastic deformation, gradually transforms to the final fine grain structure. This is believed to occur through continual decrease in the average grain size accompanied by accumulation of misorientation between neighboring dislocation cells [115]. The model used to reflect this mechanism is presented in this chapter. In section 6.2 the progressive attempts to establish the formulation of dislocation density model is reviewed. The formulation itself is given in detail in section 6.3. In section 6.4 the procedure used to adopt the material properties for the model is described.

6.2 An overview of dislocation density models

Kocks [116] and Mecking [117] described the deformation behavior of metals and alloys in terms of a single internal variable: the total dislocation density. Within this approach, the dislocation kinetics equation governing the evolution of the total dislocation density is represented in its simplest, yet rather general, way as:

$$\frac{d\rho}{d\varepsilon} = \frac{k_0}{bL} - k_2\rho \qquad (6\text{-}1)$$

Here, L corresponds to a characteristic length scale of the cell structure, e.g. the cell size, that determines the dislocation mean free path, k_0 is a constant or slowly varying quantity and k_2 is a mechanism-dependent phenomenological parameters sensitive to strain rate and temperature. The model was highly reliable in predicting stages II and III of strain hardening as Kocks pointed in [116] “work hardening rate decreases approximately linearly over a significant range of stress strain curve”. Work hardening by this model is shown in Figure 6-1. Rolling, torsion and compression tests by Zehetbauer [118] later, revealed that stages IV and V of strain hardening are predominant at large strain. Stage IV is characterized by a nearly constant hardening rate which is followed by an appreciable drop in the stage V. Figure 6-2 shows the experimentally determined work hardening coefficient at large strain. The linear descent of hardening is followed by a constant rate in stage IV and an eventual drop in stage V.

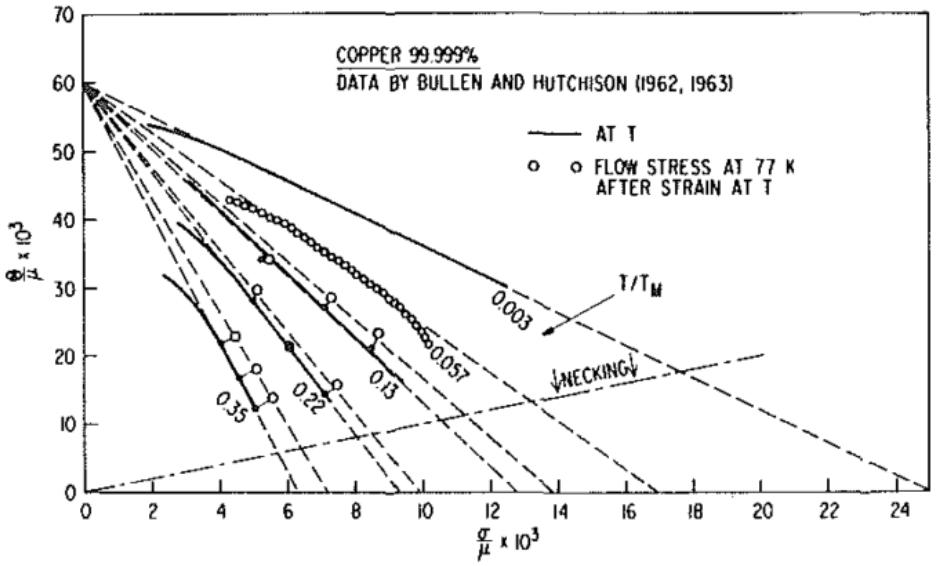

Figure 6-1. Variation of work hardening coefficient as flow stress increses [116].

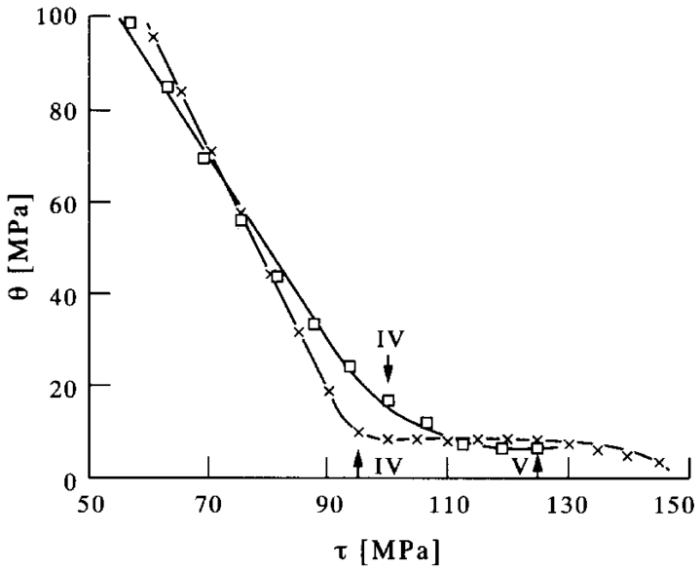

Figure 6-2. Stages IV and V were found to be predominate at large strain obtained by torsion (×) and compression (□) [27].

More detailed representation of the dislocation population is needed to reflect all stages of hardening. Mughrabi [119] presented the idea that a crystal can be considered as a composite consisting of hard dislocation walls of high local dislocation density which are separated by soft regions of low local dislocation density. Adopting the composite model, Prinz and Argon [120]

and Nix et al. [121] presented different kinetics equation for wall and cell dislocation densities able to capture stage IV and V of strain hardening. Estrin et al. [122] proposed 2D dislocation density model, sometimes called ETMB, based on Mughrabi's composite principle which consists of two coupled evolution differential equations for cell and wall dislocation taking their interaction into account. The model was generalized soon afterwards for 3D cases and arbitrary strain paths [123] and have become a useful framework to predict grain refinement in the last decade. This model is adopted in the present work to predict the grain refinement during severe shot peening.

6.3 Description of dislocation density model

Pronounced dislocation cell structure formed in the severely deformed Metallic materials is assumed to act as a pre-curser to a refined grain structure by continual reduction of its characteristic size i.e. dislocation cell size. The average dislocation cell size is assumed to be inversely proportional to the square root of total dislocation density by equation (6-2):

$$d = \frac{K}{\sqrt{\rho_t}} \qquad (6\text{-}2)$$

This form of proportionality has been shown in the early work of dislocation cell formation by Holt [124]. K is either assumed to be a constant [122–127] or an accumulated strain-dependent parameter [128,129] which, as shown by equation (6-3), quickly decreases from an initial to a saturated value with the accumulation of the total dislocation density. γ^r is the resolved shear strain.

$$K = K_\infty + (K_0 - K_\infty)\exp(-\beta\gamma^r) \qquad (6\text{-}3)$$

Owing to the assumption that the material consists of two phases of dislocation walls and dislocation cells, the total dislocation density can be expressed by equation(6-4) as weighted sum of dislocation density in the cell walls (subscript "w") and cell interior (subscript "c"). Here, f represents the volume fraction of dislocation walls. It is also assumed, as suggested by phenomenological equation (6-5), to have a decreasing approach from an initial to a saturated value as plastic strain increases. The parameter $\tilde{\gamma}$ represents the inverse of the rate of this variation as the plastic shear strain increases.

$$\rho_t = f\rho_w + (1-f)\rho_c \qquad (6\text{-}4)$$

$$f = f_\infty + (f_0 - f_\infty)\exp(\gamma^r / \tilde{\gamma}) \tag{6-5}$$

The evolution of the dislocation population through the course of straining is captured in a set of coupled differential equations (6-6) and (6-7) for the dislocation densities in the cell interior and cell walls under the Taylor-type assumption that the shear strain is the same in both phases.

$$\frac{d\rho_c}{dt} = \alpha^* \frac{1}{\sqrt{3}} \frac{\sqrt{\rho_w}}{b} \dot{\gamma}^r - \beta^* \frac{6\dot{\gamma}^r}{bd(1-f)^{1/3}} - k_c \left(\frac{\dot{\gamma}}{\dot{\gamma}_0} \right)^{-1/n_c} \rho_c \tag{6-6}$$

$$\frac{d\rho_w}{dt} = \frac{6\beta^* \dot{\gamma}^r (1-f)^{2/3}}{bdf} + \frac{\sqrt{3}\beta^* \dot{\gamma}^r (1-f)\sqrt{\rho_w}}{fb} - k_w \left(\frac{\dot{\gamma}^r}{\dot{\gamma}_0} \right)^{-1/n_w} \rho_w \tag{6-7}$$

The various terms in the right hand side of equations (6-6) and (6-7) represent the contribution from different dislocation mechanism. The first term in equation (6-6) represents the rate of dislocation generation in the cell interior due to activation of Frank-Read sources at the interface. The second term in equation (6-6) represent the fraction of dislocations the leave the cell interior towards the wall and become part of wall structure. The last term in equation (6-6) accounts for the mutual annihilation of dislocations in the cell associated with cross slip of screw dislocation or climb of edge dislocations. The first tem in equation (6-7) represents the accommodation of the dislocations in the wall corresponding to the loss of cell interior dislocations. The second term describes dislocation generation in the walls due to activation of frank-read source at the interface. Finally the last term in equation (6-7) accounts for annihilation of dislocation in the walls.

Here b is the magnitude of the Burgers vector and coefficient α*, β*, k_c and k_w, are numerical constants. The quantity $\dot{\gamma}_0$ is a reference shear rate. The exponents n_i and n_w can be taken to be inversely proportional to the absolute temperature. However, as shot peening is often introduced as a cold working process and no temperature rise has been involved in the finite element simulation, n_i and n_w have been considered constant here.

In order to link the dislocation interactions to the mechanical behavior of material, one can express the flow stress of the material as a sum of two terms:

$$\sigma = \sigma_1 + \sigma_2 \tag{6-8}$$

In equation (6-8), σ_1 represents a strain-independent contribution to the stress that originates from the resistance to dislocation glide (friction) not related to dislocation–dislocation interactions. This stress may be estimated from the yield stress of the un-deformed material

[126]. In fact this term plays the same role ‘A’ does in equation (5-1). The second term in equation (6-8), originates from dislocation-dislocation interactions and is strain and strain rate dependent. The resolved shear stress and the shear strain rate can be correlated to σ_2 and equivalent strain rate via Taylor factor:

$$\tau^r = \frac{\sigma_2}{M} \qquad (6\text{-}9)$$

$$\dot{\gamma}^r = M\dot{\varepsilon}$$

Resolved shear stress, describing the overall mechanical behavior of the cell-wall composite structure, could be correlated to the two developed resolved shear stresses in the cell and in the wall by rule of mixtures:

$$\tau^r = f\tau_w^r + (1-f)\tau_c^r \qquad (6\text{-}10)$$

Expressing resolved shear stress developed in cell and wall in terms of corresponding dislocation density by equations completes the set of equations.

$$\tau_w^r = \alpha G b\sqrt{\rho_w}\left(\frac{\dot{\gamma}^r}{\dot{\gamma}_0}\right)^{1/m} \qquad (6\text{-}11)$$

$$\tau_c^r = \alpha G b\sqrt{\rho_c}\left(\frac{\dot{\gamma}^r}{\dot{\gamma}_0}\right)^{1/m} \qquad (6\text{-}12)$$

Where, α is a constant, G is shear modulus and m the inverse strain rate sensitivity parameter. Dislocation evolutions have been linked to the variation of flow stress through the course of straining. It was shown that the model is able to successfully predict all stages of strain hardening at large strain [122,123], grain refinement under equal channel angular pressing [125,127], high pressure torsion [129] and Taylor impact test [126].

6.4 Material parameters

Having an appropriate set of material parameters in hand one can input the experienced strain and strain rate into the set of equations and get the resultant dislocation evolution, refinement and flow stress variation. In order to identify the appropriate parameter for the present material equations (6-2) to (6-12) were programmed in MATLAB. On the other hand, result of Johnson-Cook constitutive (equation (5-1)) for high strain rates (10^4,10^5,10^6) have been calculated. A

global minimization approach was applied using genetic algorithm. Dislocation density equations were solved starting from initial values while the target function was to minimize the difference between calculated flow stresses by dislocation density model the ones provided by Johnson-Cook equation. Table 6-1 summarizes 7 tuned parameters for AISI4340 as well as other constants used in the model.

Table 6-1. 7 tuned parameters for AISI4340 as well as other constants used in the model.

Tuned parameters							Other material parameters												
α^*	β^*	k_i	k_w	n_i	n_w	m	b (m)	M	α	G (GPa)	f_0	f_∞	$\dot{\gamma}_0$	K_0	K_∞	$\tilde{\gamma}$	β	$\rho_c^{(t=0)}$ (m^{-2})	$\rho_w^{(t=0)}$ (m^{-2})
0.154	0.078	18.6	32.8	89.8	90.3	60.8	2.48×10^{-10}	3.06	0.25	82	0.25	0.06	10^7	100	1	3.2	0.26	2.5×10^{13}	5×10^{13}

6.5 Conclusion

The most commonly accepted type of models of grain refinement due to large strain, particularly under SPD conditions, are based on the notion that a dislocation cell structure, which forms already in the early stages of plastic deformation, gradually transforms to the final fine grain structure. Dislocation generation, migration and annihilation are the main mechanisms that the presented refinement model is able to capture. The model in fact was linked to finite element simulation. Nodal values of plastic strain and strain rate are used as an input to the dislocation density model to simulate the evolution of dislocation density and dislocation cell size.

Part IV Result and Discussion

7 Finite element simulation of peening; from conventional to high coverage

7.1 Introduction

Result of finite element simulation of shot peening and its experimental verification are presented in this chapter. An important feature of the proposed technique to simulate shot peening with respect to available models in literature is its ability to capture and simulate high coverage. High coverage is a crucial parameter in the performed severe shot peening. In section 7.2 residual stress distribution after sever shot peening is presented. Comparison with experimental measurement is given in order to verify the model. In section 7.3 evolution of surface roughness in severe shot peening is discussed. Comparison of simulated and experimentally measured roughness is also given.

7.2 Residual stress

Figure 7-1 demonstrates the residual stress distribution after shot peening with 100% and 1000% coverage. Compressive state of residual stress at the surface and in the subsurface layer is developed in the process. Residual stress has been mainly distributed uniformly at different points of the subsurface layer. The value of compressive residual stress near the surface has not been considerably changed form 100% to 1000% coverage. However, the thickness of compressed layer has been increases by increasing coverage.

Comparison of XRD measurement and finite element simulation of in-depth residual stress distribution is given in Figure 7-2. It should be noted that value of residual stress at each depth has been calculated by averaging the streets values of all finite element nodes exist at that depth. It is a reasonable technique as XRD measurement of residual stress is in fact the average determination of residual stress in the irradiated area. The agreement between simulation and experiment is good; providing adequate verification of the model. An important feature of this model is its ability to capture a realistic evolution of coverage; thus its applicability to simulate severe shot peening with satisfactory agreement. This is a crucial step towards simulation of grain refinement during severe shot peening as the output of FE model will be used in the dislocation density model.

Figure 7-3 shows evolution of residual stress as coverage increases. It can be seen that significant evolution occurs during peening till full coverage is obtained (100%). Afterwards (form 100% to 1000%), depth of compressed layer gradually increases while the state of residual stress near the surface does not vary considerably.

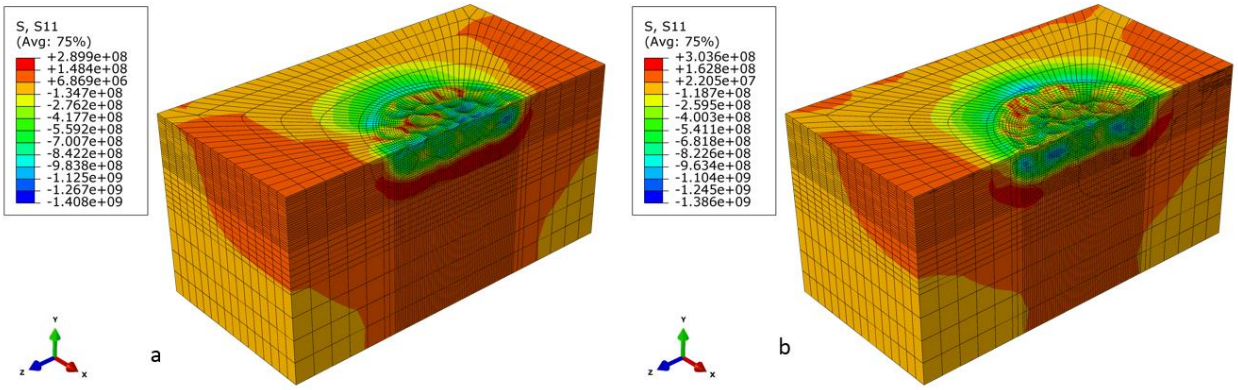

Figure 7-1. Residual stress distribution after shot peening with 100% and 1000% coverage.

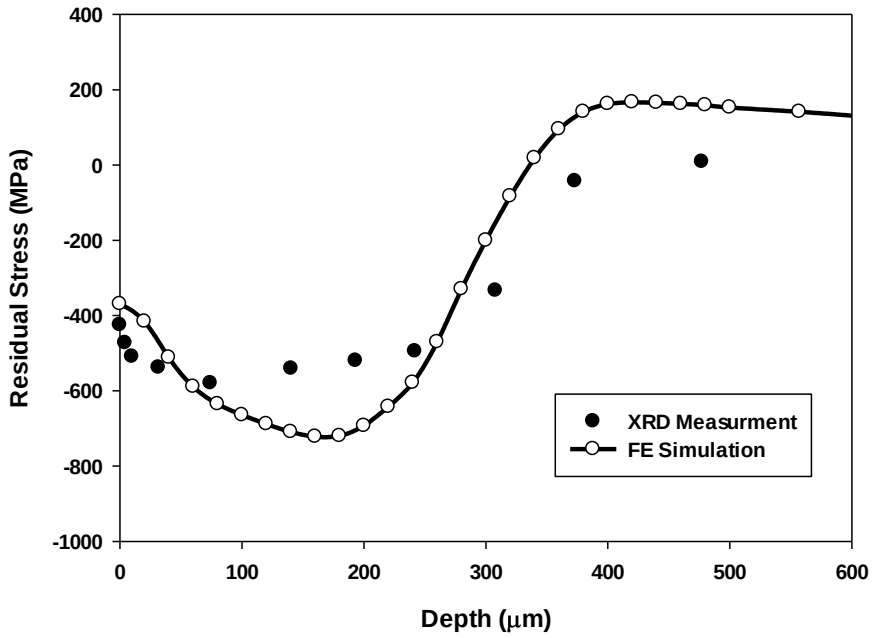

Figure 7-2. Comparison of XRD measurement and finite element simulation of in-depth residual stress distribution.

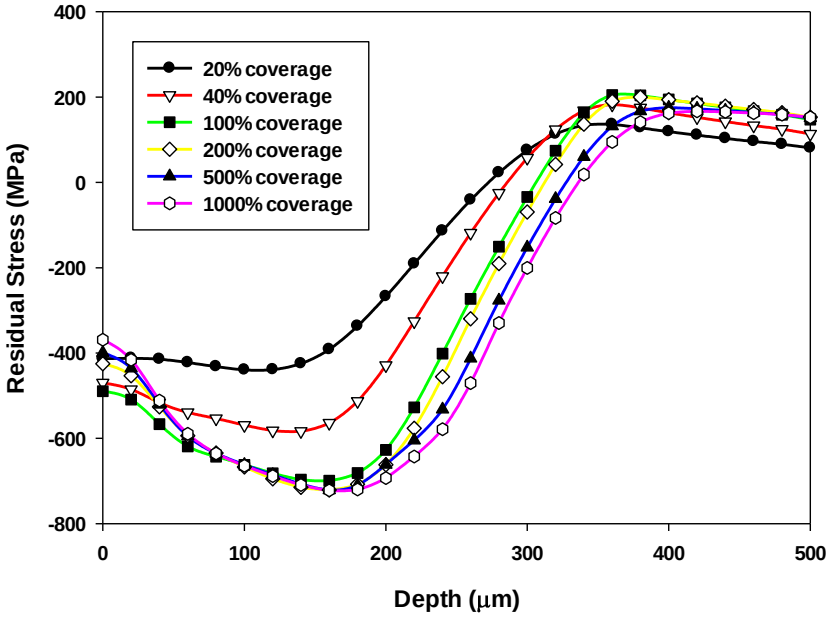

Figure 7-3. Evolution of residual stress as coverage increases.

7.3 Surface roughness

Figure 7-4 shows surface vertical displacement after shot peening with 1000% coverage. Uniform pattern of roughness is generated after peening. Having nodal values of vertical displacement one can easily calculate roughness parameters. Figure 7-5 shows roughness parameter evolution as coverage increases. Roughness sharply increases in early stage of peening till the coverage is 20%. The rate of increment then gradually decreases up to 200% coverage where it reaches to a saturation limit. Experimental measurements of roughness parameters have been also superimposed into the graph. Very good agreement can be seen between simulation and measurement. It again confirms that the proposed finite element simulation is able to capture the phenomena occurring at high coverage.

7.4 Conclusion

Residual stress and surface roughness evolution simulated by finite element technique were presented and compared with the experimental measurements. Good agreement between simulation and experiment demonstrate the model is reliable enough such that its output can be used input for the dislocation density models. After full coverage, depth of compressed layer gradually increases while the state of residual stress near the surface does not vary considerably.

Roughness sharply increases in early stage of peening till the coverage is 20%. In high coverage, however, roughness evolution shows a saturation behavior.

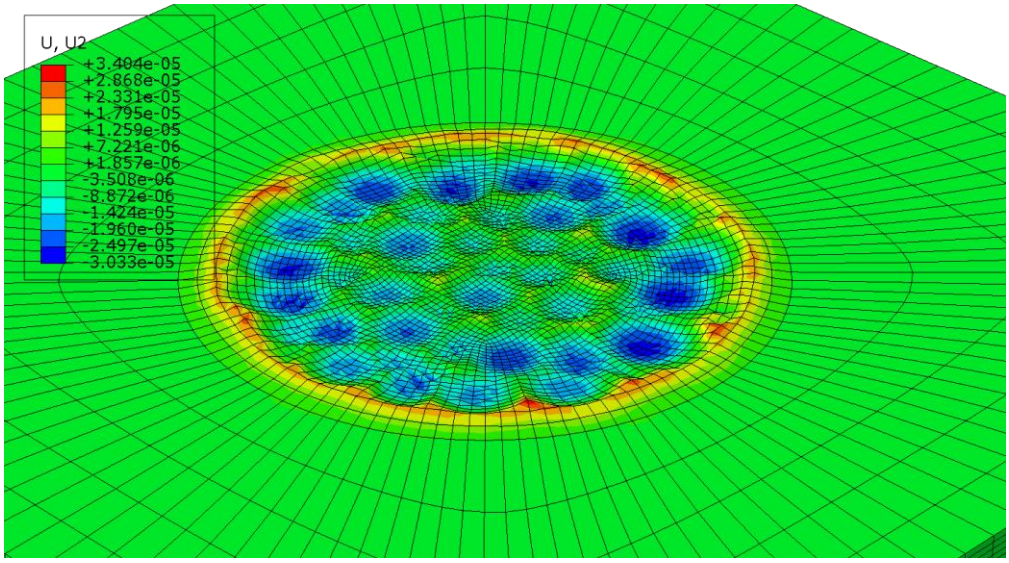

Figure 7-4. Distribution of surface vertical displacement after shot peening with 1000% coverage

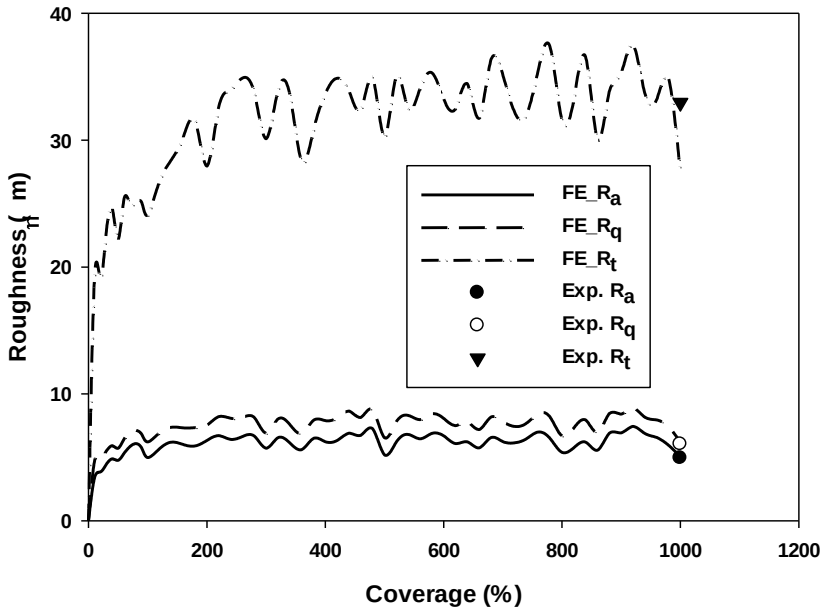

Figure 7-5. Roughness parameter evolution as coverage increases. Experimental measurements were also superimposed in the graph.

8 Surface nanocrystallization by severe shot peening

8.1 Introduction

The results of the dislocation density model and experimental observation of the refined structure are presented in this chapter. Evolution of plastic strain during severe shot peening is used to run the dislocation density model. Accumulation of dislocation density and refinement of dislocation cell size are calculated. In order to build the concept, the refinement after single impact is discussed in section 8.2. The effect of processing parameter on the resultant refinement is presented in section 8.3. Results of the simulation for the practical sever shot peening that involves multiple impacts are presented in section 8.4. TEM observation of refined structure and cell size measurement are given in section 8.5. Comparison of experimental measurement and numerical simulation is presented in the same section. The chapter is concluded by further discussion about two other phenomena occurring during surface nanocrystallization of the present material in section 8.6.

8.2 Single impact

Figure 8-1 shows distribution of residual stress, equivalent plastic strain, total dislocation density and dislocation cell size after single impact. Shot peening, as shown by lots of experimental observations [38,40,41], induces compressive residual stress at the surface and in the subsurface layers. Based on the finite element simulation, substantial compressive residual stress is developed in the subsurface layer after a single impingement. However, the state of residual stress right at surface is tensile. Analytical solutions based on Hertzian elastic contact theory [130] and simplified plastic behavior predicts compressive state at the surface [131]. Residual stress caused by static compression is approximately zero at the center of indentation and compressive near the center. These might seem contradictory with the result of present single indentation at the first glance. However, experimental comparison of static compression with dynamic impact by steel ball showed the surface residual stress caused by static compression is compressive near the center whereas surface tensile residual stress is created at the center of the indentation by dynamic impact and [100]. In this case compressive residual stress is created outside of the indentation. This experiment supports the resultant distribution of residual by finite element. What happens in a real peening process is that as dynamic impacts repeatedly occur around the first indentation and the density of indentations increase, compressive residual stress is created in the first indentation area [100].

Effective or equivalent plastic strain is a critical parameter in the severe plastic deformation processes. Depending on material and deformation techniques if it exceeds a critical range nanocrystalline structure will be formed [53,54]. Figure 8-1 b shows that the maximum plastic strain after a single impingement occurs in the immediate subsurface layer near the indentation edge where material piles up. As the plastic deformation is accommodated by generation and

rearrangement of dislocations, it is not surprising that the maximum dislocation density and the minimum cell size are both located at the same point with the maximum plastic strain. Umemoto et al. [53] experimentally observed that nanocrystalline layer is formed along the edge of the crater after 8 times of particle impact at the same point. This experimental observation can be explained by the present simulation that introduces the same point as the point of critical refinement after single impact. As demonstrated in Figure 8-1 c, dislocation density increased by 2 orders of magnitude after single impact, for instance from 3.1×10^{13} to 1.5×10^{15} at the most critical point. Based on the selected initial dislocation densities, the initial cell size was calculated to be approximately 18 µm. As illustrated in Figure 8-1 d dislocation cell size was refined from the 18 to 2.47 µm. This implies that significant refinement might occur in the first impact.

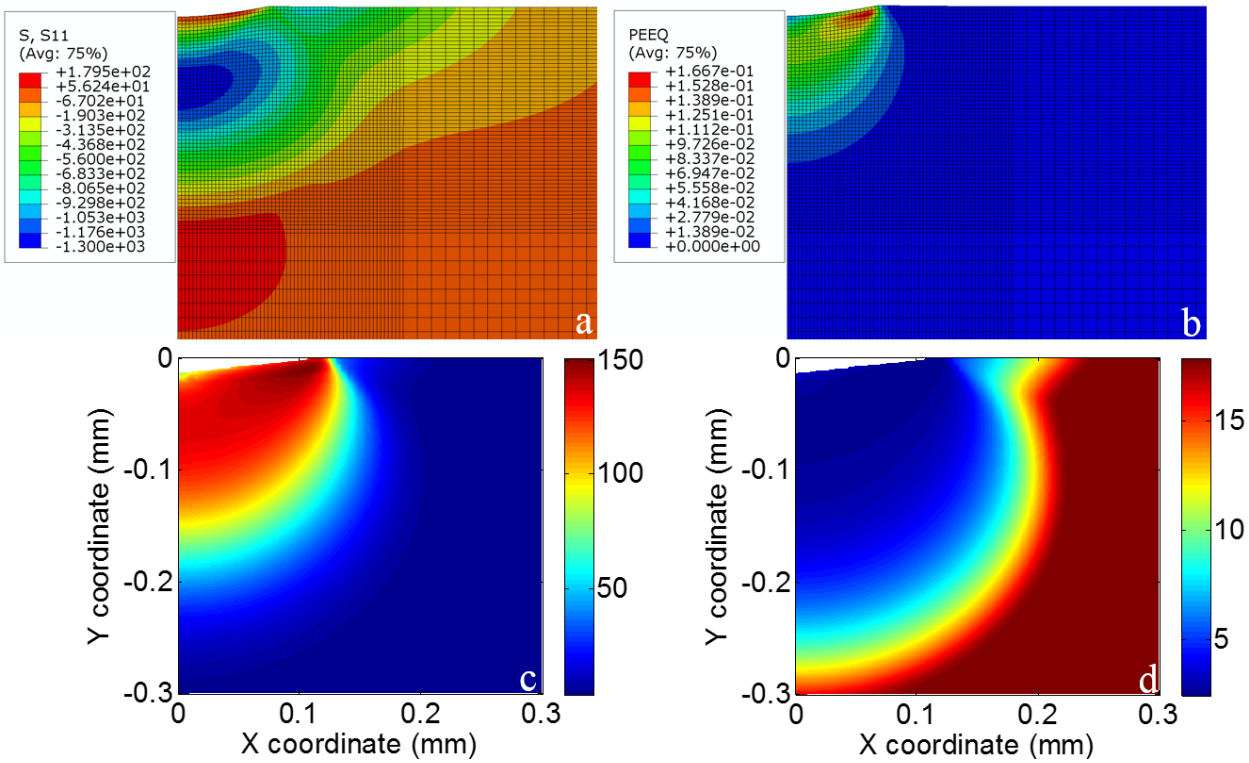

Figure 8-1. Distribution of a) residual stress (MPa), b) equivalent plastic strain, c) total dislocation density (10^{13} m^{-2}) and d) dislocation cell size (µm) after single impact.

8.3 Parametric study

Figure 8-2 summarizes the effect of processing parameters on the minimum cell size obtained by single impact. As shot velocity increases higher refinement in cell size can be obtained and the trend is ever-increasing. As shot hardness increases finer cell size can be obtained. However, the

amount of refinement tends to saturate for harder shots. As shot radius increases, no considerable change in the level of refinement can be observed. These results suggest that shot velocity is the most influential processing parameter as far as grain refinement and surface nanocrystallization is regarded in severe shot peening. There is good agreement between the results of the simulation and few experimental evidences from literature. For instance, High coverage air blast shot peening was applied on carbon steel using two types of media (0.05 mm and 0.8 mm in size) [56]. It was found that nano area can be formed in very short treatment times and the thickness and continuity of the nanolayer is enhanced. On the contrary, the nano-crystalline region is more difficult to synthesize when using large shot particles even though the deformed are is much thicker. Although bigger particles have higher energy, but the contact area also rise at same time, then the strain rate with bigger particles was mentioned to be smaller than that in the case of smaller particles. In another experimental study, the volume of NC region developed in the ABSP of carbon steel using 0.05 mm shots with 190 m/s velocity and 6000% coverage was larger than USSP of the same steel using 0.4 mm shots and with velocity of 20 m/s and 108000% coverage [52]. A simple calculation shows that the amount of kinetic energy transferred in USSP was by far higher than ABSP. However, ABSP came up with higher level of refinement which clearly affirms the important effect of shot velocity in micro-structural refinement. In another numerical study single impact of with 7.8 mm ball diameter and 5 m/s impact velocity was compared to a hypothetical high speed shot peening with 0.3 mm ball diameter and 670 m/s impact velocity using finite element simulation. Balls in both cases convey the same amount of kinetic energy before impact. However, higher maximum effective plastic strain was obtained in the case of higher velocity [132]. These all suggest that smaller balls are quicker in creating a nano-crystalline surface layer than larger balls for a given kinetic energy.

8.4 Multiple impacts; practical severe shot peening

Figure 8-3 shows the variation of surface dislocation density and cell size as coverage increases. Surface dislocation density increases during the process as more shots hit the surface. A sharp increase can be seen in the early stage of deformation where dislocation density exceeds 10^{15} m^{-2}. Then the rate of increment gradually decreases as dislocation density increases. The surface cell size accordingly follows the same trend and much more impact needed to refine the cell as it approaches 100 nm. The trend affirms that subdivision of cell into less than 100 nm is feasible at high coverage by severe shot peening. The trend of dislocation density evolution is also compatible with the argument on the limit of dislocation density and refinement in severely deformed iron which estimated the limit of dislocation density to lie in the order of 10^{16} m^{-2} [133]. Experimental measurement of yield stress of surface nano-crystallized low carbon steel by high energy shot peening showed pronounced increment of yield strength after HESP for 30 min while for further increasing the treatment time to 60, 90 and 180 min strength approached a saturated value [58]. As coverage and dislocation density are directly related to peening time and

strength respectively, one can speculate the trend obtained by modeling is in agreement with the reported experimental evidences.

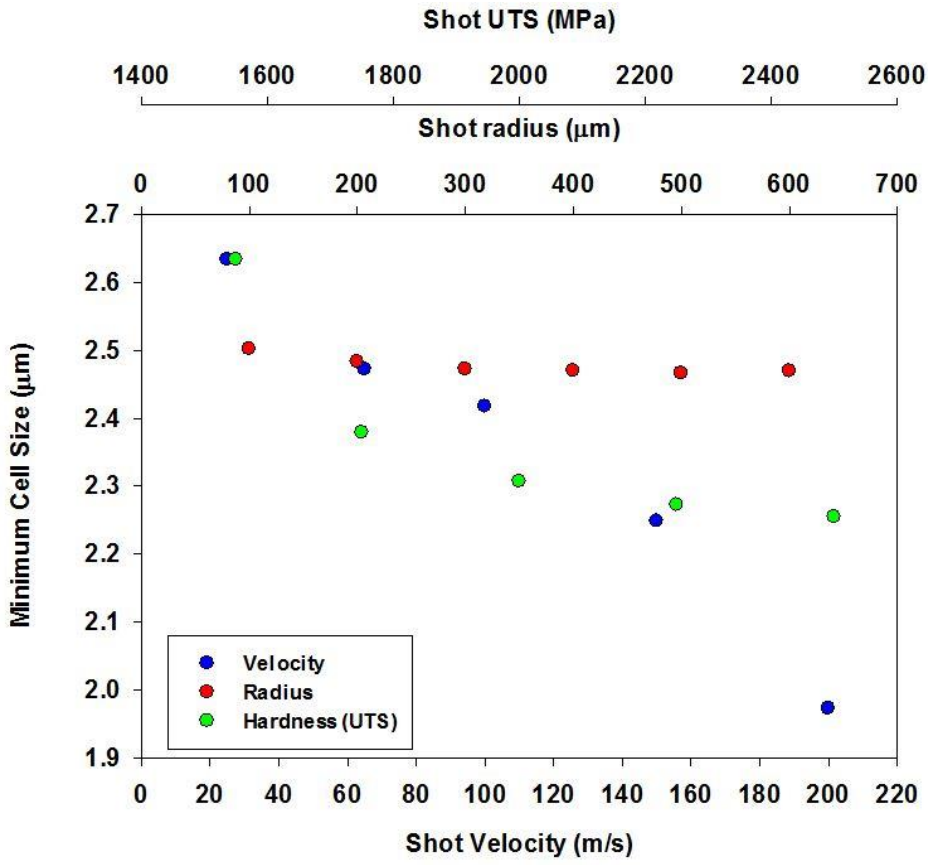

Figure 8-2. Effect of processing parameters on the minimum cell size obtained after single impact.

Figure 8-4 shows surface and in-depth distribution of plastic equivalent strain after shot peening with 100% coverage and severe shot peening with 1000% coverage. The maximum plastic strain after typical peening was simulated to be around 1 while it significantly increased to 7.8 after severe peening. The minimum amount of strain necessary for nanocrystallization was reported to be around 7-8 [53,54]. Therefore, the simulation suggests that nanostructured surface layers might be produced after the present severe peening experiment. Finite element simulation shows uniform distribution of plastic strain in various depths after peening. The maximum strain is induced on the surface and it gradually decreases as depth increases. The exact opposite trend is observed in grain/cell size supporting the existence of a meaningful connection between plastic strain and grain refinement.

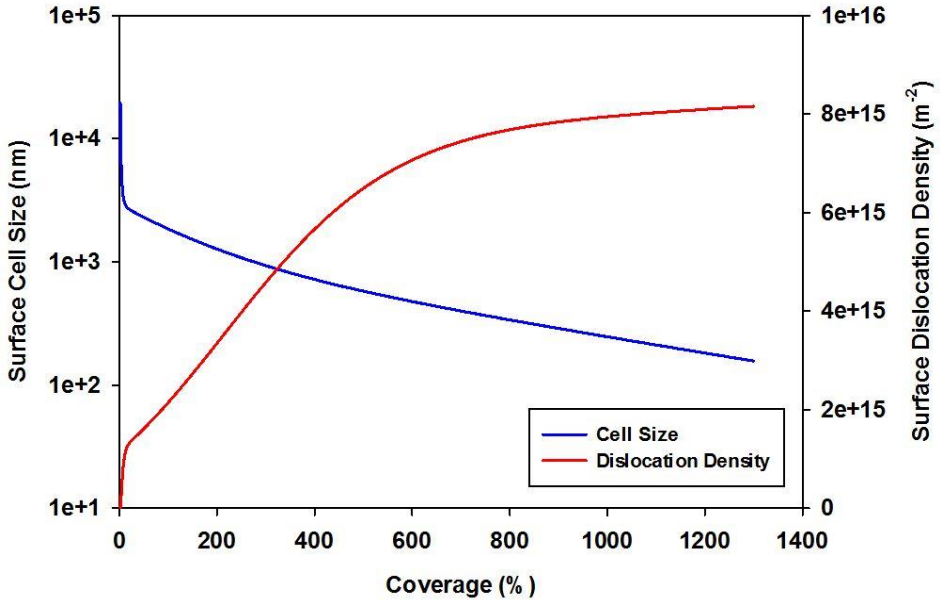

Figure 8-3. Variation of surface cell size and dislocation density with coverage.

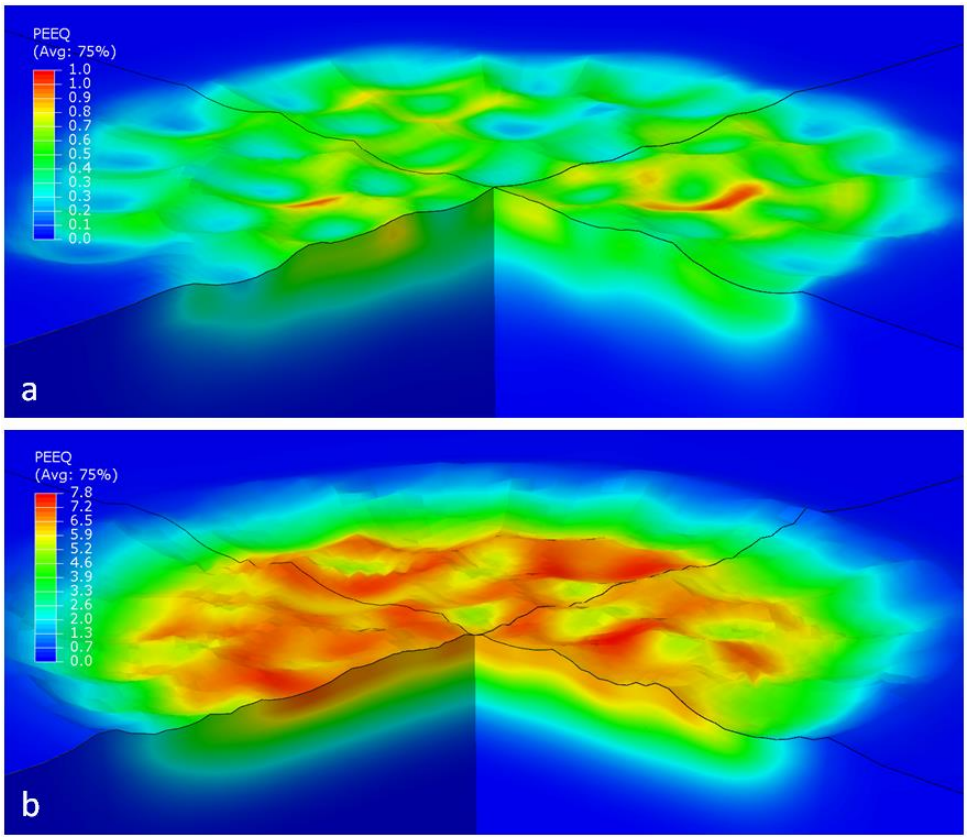

Figure 8-4. Surface and in-depth distribution of plastic equivalent strain after a) shot peening with 100% coverage and severe shot b) peening with 1000% coverage.

8.5 Experimental observation of the refined structure; verification of the numerical framework

Figure 8-5 shows the cross section SEM and TEM micrographs taken at different depths of treated specimen. Nano-sized grains are observed at the top surface of severely deformed specimen (1000% and 1300% coverage). For 650% coverage the surface grains are in the ultra-fine regime. The average grain sizes measured by TEM at the surface are 370, 160 and 130 nm for 650%, 1000% and 1300% respectively. TEM micrographs clearly affirm that the higher the coverage is the smaller the cell/grain size that is formed at the same depth of each specimen.

The form of the grains at the very top surface is equiaxed with random crystallographic orientation. The same observation have been also reported for similar mechanical treatments [33,55,57,58,61,63]. As one moves away from the surface, a duplex micro-structure appears. Equiaxed ultrafine cells and Lamellar-shaped cell are present. Lamellar-shaped cell structure with a width of around 250 nm near the surface, 500 nm far from the surface and length of few microns can be seen in Figure 8-5. Inside these lamellar structures, in some points, smaller equiaxed cell can be also observed. SEM image of 100% and 200% peened specimen show the initial micro-structure is sheaf shape bainite. As one moves from 200 μm in depth towards surface, SEM micrographs demonstrate the initial sheaf shape needle or plates are subdivided to finer needles and plates as a result of multiple impingements. These observations suggest the main refinement mechanism is that plastic strain induced by multidirectional impacts is accommodated by generation, accumulation and re-arrangement of dislocation in the form of lamella-shape cell and later in the form of dislocation array intersecting and cutting the original lamella. As plastic strain increases and in order to minimize the total energy of the system lamella walls and consecutively intersecting dislocation array transform into sub-boundaries. Further increasing plastic strain is accompanied by accumulation of misorientation between neighboring dislocation cells and gradually transform them to the final fine grain structure. This microstructural refinement can also be realized in the selective area electron diffraction (SAED) patterns shown in Figure 8-5. The streak spots of SAED pattern clearly show the evidence for which the nanostructure is developed on severely deformed top surface by shot peening. This refined structure is retained up to the depth of 100 μm in both 1000 and 1300% coverage condition (see the SAED patterns of 100 μm depth), but not in the peened sample with 650% coverage.

Figure 8-6 shows in depth distribution of cell size resulting from the numerical modeling as well as the ones experientially measured by SEM and TEM. The maximum refinement occurs at the surface. No considerable variation of cell size is observed in the top surface layer up to 50 μm in depth. This region in fact corresponds to the equiaxed nano-sized or ultrafine grains structure in severely peened specimens. The variation then is followed with gradual increment of cell size up

to around 200 μm where it encounters a sharp increment towards the cell size of the initial structure. The structure in 50 to 200 μm in depth is duplex structure containing both equiaxed and lamellar-shape cell. Similar trend has been experimentally observed where slight increase of cell size from surface to a certain depth is followed by a rapid increment to the micrometer regime in high energy peened carbon steel.

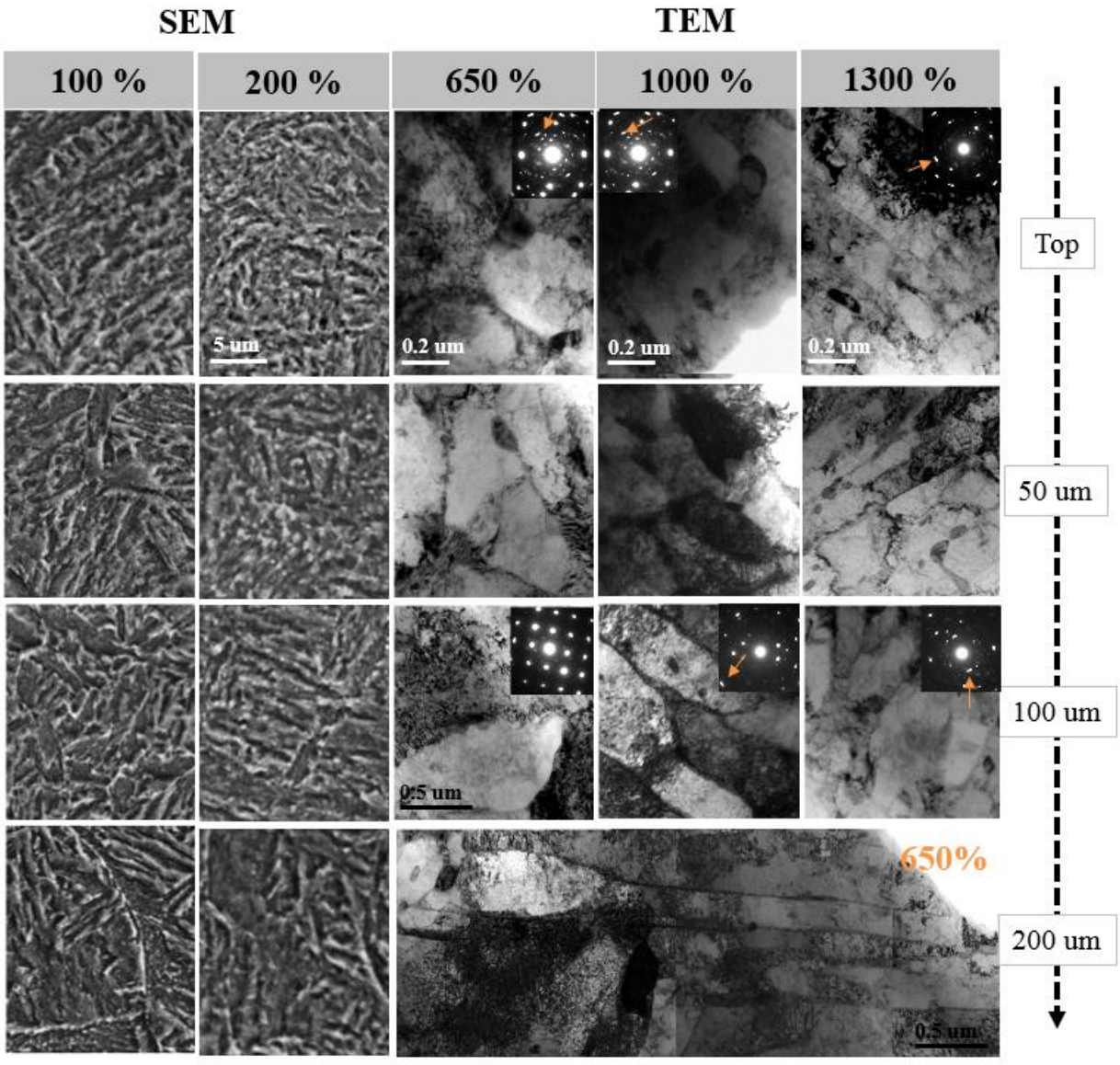

Figure 8-5. Cross section SEM and TEM micrographs taken at various depths of treated specimens.

It should be mentioned that typical initial dislocations of 2.5×10^{13} and 5×10^{13} m^{-2} were assumed for cell and wall respectively. The initial cell size accordingly was calculated to be around 18

μm. The initial dislocation densities in the studied material might have been higher in the present material as it contains bainite structure. Nevertheless, the resultant error due to starting with lower dislocation density has negligible effect on the final cell size near the surface as dislocation density rapidly increases by two orders of magnitude in the very initial stage of peening (demonstrated in Figure 8-3). It might produce deviation between simulation and experiment in the deeper region, say deeper than 300 μm, where cell size approaches to the size of initial structure. One should have the exact value of initial dislocation density in order to get the appropriate fit in deeper part too. Superimposed data from TEM and SEM measurements affirms that the numerical framework is able to correctly simulate the refinement. The agreement is very good in subsurface layer up to 100 μm. After that deviation appears between numerical and experimental results. As shown in Figure 8-5, for the case of peened sample with 650% coverage, the coarse bainite laths coexist with the refined cell size around 200 μm in depth. The lath sizes are larger 3 μm in the longitudinal direction and thus the corresponding TEM result might be underestimated due to the error related with counting statistics. Therefore, if the microstructure investigated consists of duplex microstructure in the range of the depth between 100 and 380 um, the detailed comparison between TEM and SEM results would be required to improve the reliability of experimental evaluation.

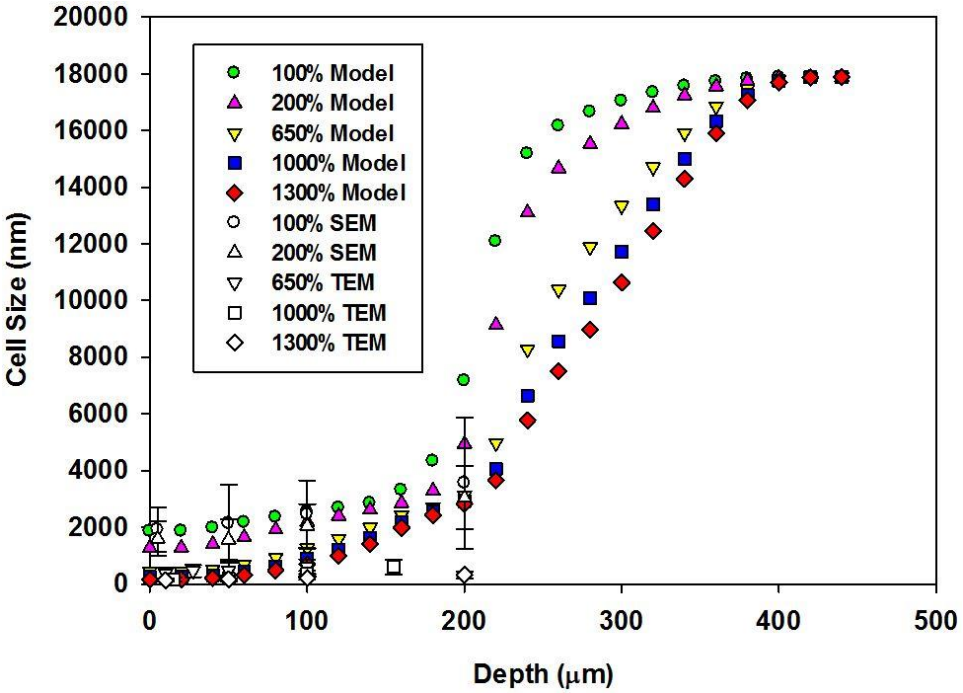

Figure 8-6. In depth variation of cell size.

Another important outcome of the numerical result depicted in Figure 8-6 is that as coverage increases the cell size in surface and subsurface layers decreases and the thickness of nono-crystallized or refined layer increases. However, the trend suggests that the thickness of refined layer is going to be saturated in very high coverage. Experimental observations demonstrate that the thickness of the nano-crystalline layer formed by high coverage shot peening initially increases with peening time [53] but eventually remains unchanged after a certain level of coverage [55,69]. However, measurement of the grain size after recrystallization at the 10 μm inner position revealed and ever decreasing trend as coverage increases [55].

8.6 Dissolution of cementite and nano-sized carbide precipitation during surface nanocrystallization

TEM images taken from the top surface and 200 μm in depth of peened specimen with 1300% coverage are shown in Figure 8-7. In general, M_3C-type cementite is distinguished from its orientation relationship and habit planes in the martensitic matrix [134]. Since the plate-like cementite has the Bagarystski orientation relationship with the martensite (ferrite) matrix; $\{110\}_a//(100)_{M3C}$, the plate-like M3C cementite has the {110} habit planes of the ferrite matrix. Hence, in a cube-oriented beam in the TEM, the M_3C cementite can be observed in two perpendicular <110> directions. Two interesting features can be observed on the top surface shown in Figure 8-7 a. The first is dissolution of cementite. This can be realized by the trace comprising of small particles (<100 nm) of spherical shape, which are entirely arrayed along a <110> direction, but not in each particle. Completely different feature, on the other hand, exist at 200 μm in depth region (Figure 8-7 b) where cementite can be observed with the size of approximately 200 nm within and in between of the plates. This suggests microstructural refinement by severe shot peening is also accompanied by dissolution of cementite. Dissolution of cementite in ferretic matrix in the nanocrystalline layer has been also reported in high coverage peened Fe–0.80C with initial spheroidite structure [53,54].

Another observation is that considerable nano-sized particles are precipitated at the top surface region as shown in Figure 8-8. Large amounts of particles are mainly M_2C-type carbides. Those particles were characterized using their intrinsic orientation relationship with matrix; the needle or rod-shaped M_2C carbide has the orientation relationship with the martensite matrix; $(110)_a//(0001)_{M2C}$, $[100]_a$ $//[2110]_{M2C}$. In other words, the M_2C carbide precipitation can be found in <100> cube directions of [100] zone-axis. This result is also confirmed by the SAED patterns shown in Figure 8-5. The diffraction spots with smaller distance from the direct beam at the surface are larger than that of 200 μm depth. This reflects the existence of other phase, especially carbides; differently from BCC matrix with lower upper limit in d-spacing, carbide phases have larger d-spacing (smaller spot radius). These microstructural findings suggest that the severe plastic deformation by shot peening can lead not only lead to the microstructural

refinement by introduction of large density of dislocations but also result in the dissolution of cementite and subsequent nano-sized carbide precipitation.

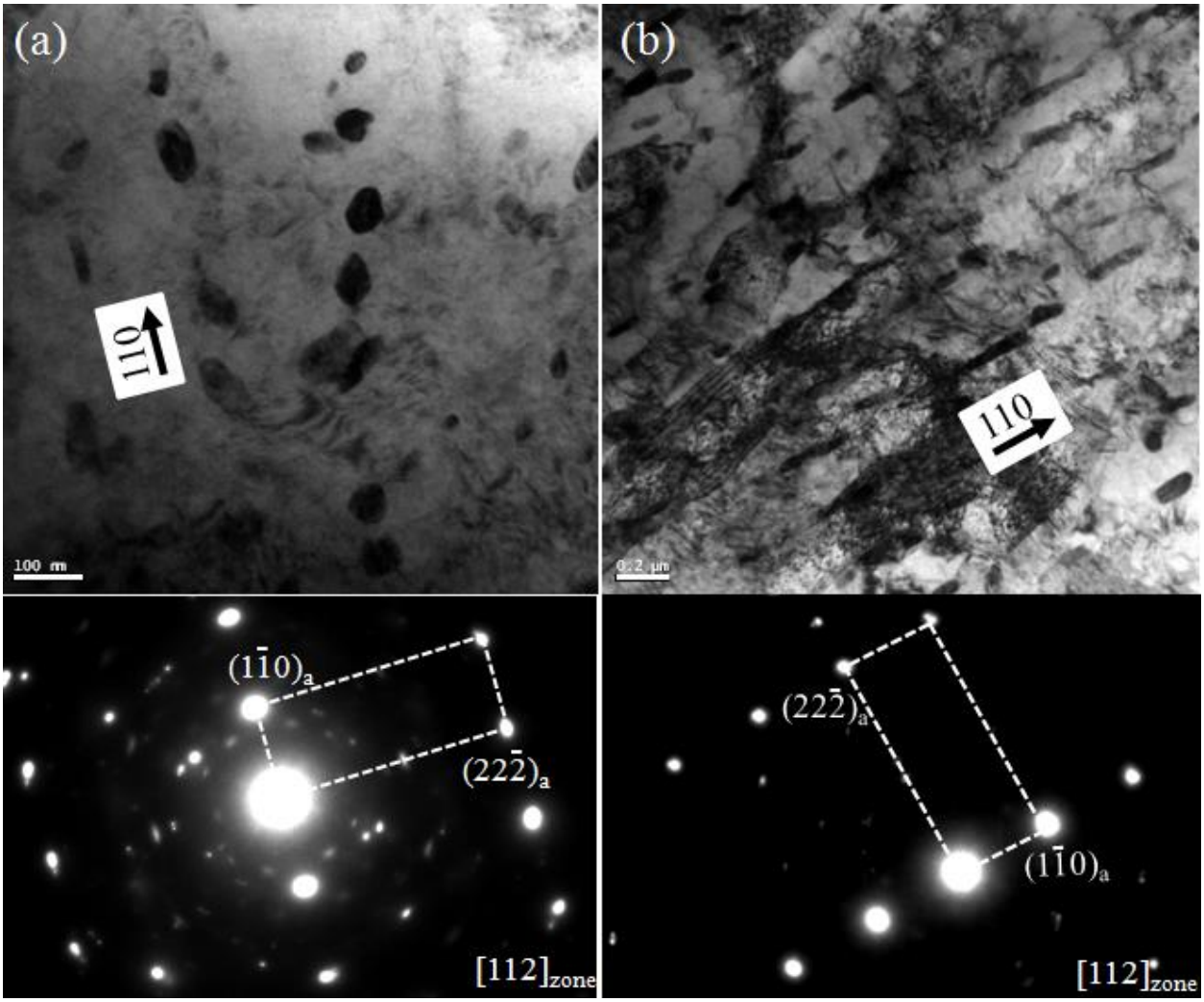

Figure 8-7. TEM images taken form a) top surface and b) 200 µm depth of peened specimen with 1300% coverage.

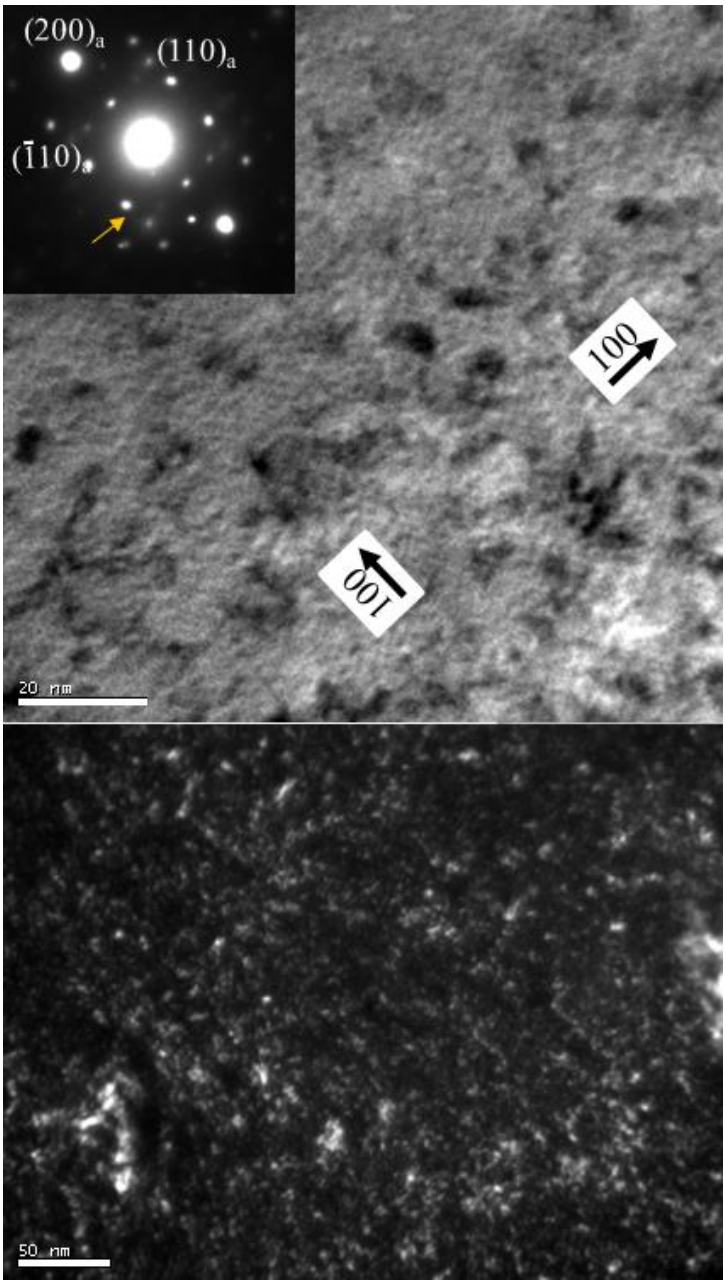

Figure 8-8. Bright and dark field TEM image taken for the top surface of peened specimen with 1300%.

8.7 Conclusion

A numerical framework was suggested in order to simulate the surface nanocrystallization of severe shot peening with the special attention on prediction of grain/cell size at the surface and its gradient toward the subsurface layer. It was found that the maximum plastic strain and critical refinement after a single impingement occurs in the immediate subsurface layer near the indentation edge where material piles up. Shot velocity was found to be the most influential

processing parameter for structural refinement as compared with media size or its hardness. A sharp increase of dislocation density and considerable refinement were found to occur at the early stages of peening. It was affirmed by numerical simulation that subdivision of cell into less than 100 nm is obviously feasible at high coverage by severe shot peening. Nano-sized grains are observed at the top surface of severely deformed specimen (1000% and 1300% coverage). For 650% coverage the surface grains are in the ultra-fine regime. The average grain sizes measured by TEM at the surface are 370, 160 and 130 nm for 650%, 1000% and 1300% respectively. TEM micrographs clearly affirm that the higher the coverage is the smaller the cell/grain size that is formed at the same depth of each specimen. Comparison of simulated and experimentally measured cell size clearly affirms that the proposed numerical framework is able to simulate surface nanocrystallization. It was shown that surface nanocrystallization in the present material is accompanied by dissolution of cementite and precipitation of nano-sized particle at the top surface.

9 Combination of severe shot peening and nitriding

9.1 Introduction

Generating compressive residual stress, increasing the hardness and reducing the grain size can greatly improve fatigue behaviour. Nitriding is a well-known thermo-chemical process to increase surface hardness. It was shown that severe shot peening can induce compressive residual stress and generate nano-structured layer. This justifies the interest in developing combined treatments, able to achieve all the just mentioned factors. This is the motivation that, the effect of combination of severe shot peening and nitriding on the fatigue limit and mechanical properties is investigated in this chapter. Micro-structural observations after hybrid treatment are given in section 9.2. The effect of hybrid treatment on hardening and residual stress will be discussed in section 9.3 and 9.4. Results of fatigue test and fractography of the fractured surface are given in section 9.6 and 9.7. The chapter is conclude by a critical discussion using local fatigue strength approach to justify the experimental observations in section 9.8

9.2 Micro-structure

As demonstrated in Figure 9-1, from the overall view of the cross section by optical microscopy three distinct regions can be recognized for all nitrided specimens. A very thin white (compound) layer of few microns was formed on the top surface. The composition of this hard and brittle layer is dependent on nitriding processing parameters. However, with the conventional processing parameters it is usually a combination of ϒ' (Fe_4N) and ε ($Fe_{2-3}N$) phases [135]. Beneath the compound layer the so-called diffusion zone with dispersed needle shape precipitates of ϒ' in ferritic matrix as well as the solid solution of nitrogen in ferrite exists. Compound and diffusion layer are considered as hardened case after nitriding. Below the diffusion layer, substrate without any evidences of microstructural change can be observed. No microstructural change can be observed for severe shot peened specimen by means of optical microscopy.

Figure 9-2 illustrates scanning electron microscopy of the cross section of the treated specimens. Formation of compound layer after nitriding is more evident here (Figure 9-2 a). Depth of compound layer was measured to be in the range of 4-6 μm after nitriding. A precise look at the top surface of the nitrided specimen demonstrates that pores have been formed up to 1-2 μm within the compound layer (shown with arrows).

Subsequent severe shot peening suppressed the porous structure at the top of the compound layer (Figure 9-2 c). The rest of compound layer, on the other hand, survived after peening. Nonetheless, it was highly damaged and lots of micro-cracks (shown with arrows) were formed. Formation of micro-cracks can be explained by considering high brittleness of compound layer and high coverage applied for shot peening. Bearing in mind that 1000% coverage, theoretically,

means each part of the surface has been treated ten times with steel shots. When such a hard and brittle layer is subjected to repeated impingements, possibility of micro-crack formation increases.

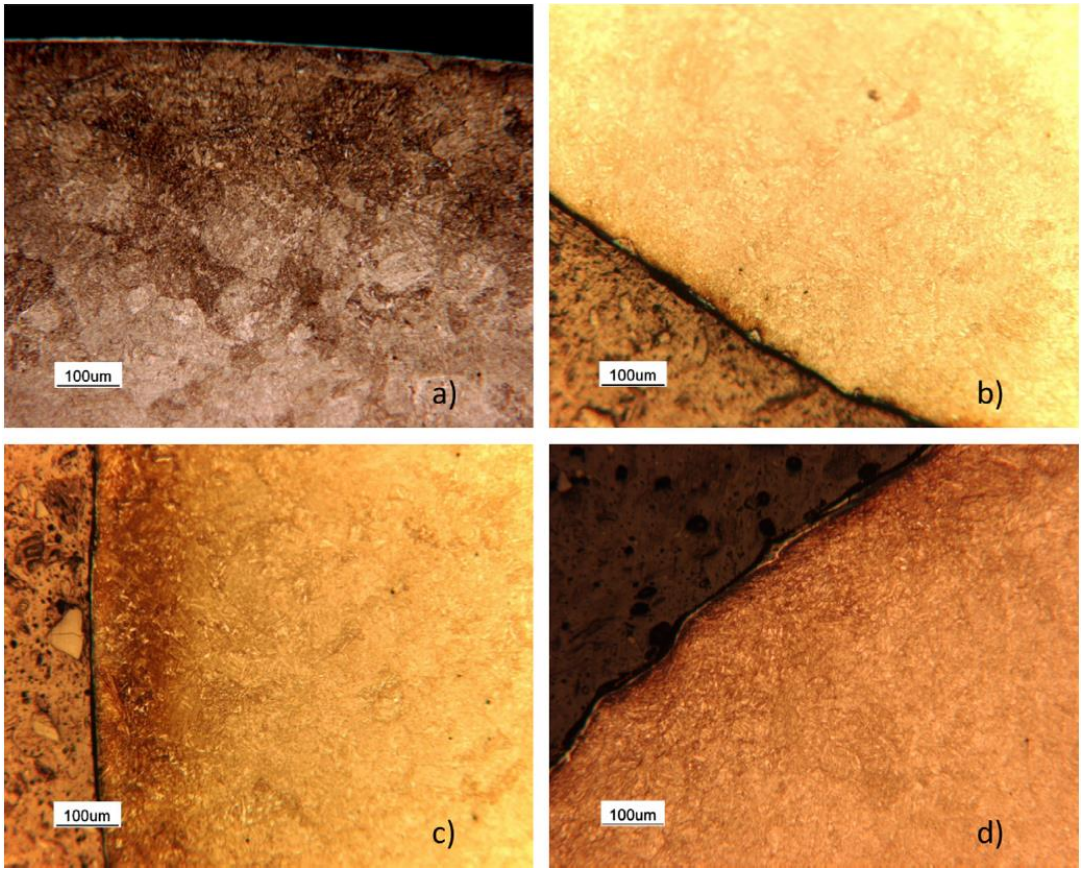

Figure 9-1. Cross sectional optical microscopy of a) N, b) SSP, c) N+SSP and d) SSP+N specimens.

Performing severe shot peening prior to nitriding caused up to three times deeper compound layer (Figure 9-2 d) with respect to the only nitrided specimen. This is due to the very dense structure and fine-grained surface layer generated by severe plastic deformation during severe shot peening (Figure 9-2 b). By severe shot peening much more defects and interfaces are generated in surface layers through repeating impingements. With the proceeding of collisions, some areas approach to the critical condition of nanocrystallization and grain fragmentation below 100 nm occurs [35]. In fact, in conventional nitriding of coarse-grained steel, nitrogen diffusion in the Fe lattice dominates. In the nano-crystalline structures, on the other hand, nitrogen mostly diffuses along grain boundaries with much faster diffusivity because of a much smaller activation energy (approximately half) compared with that for the lattice diffusion [82]. It is also worth mentioning here that the compound layer in this case is not as dense as nitrided or

nitrided plus severe shot peened specimen and more porosity and even some discontinuity can be observed in the upper part of the compound layer.

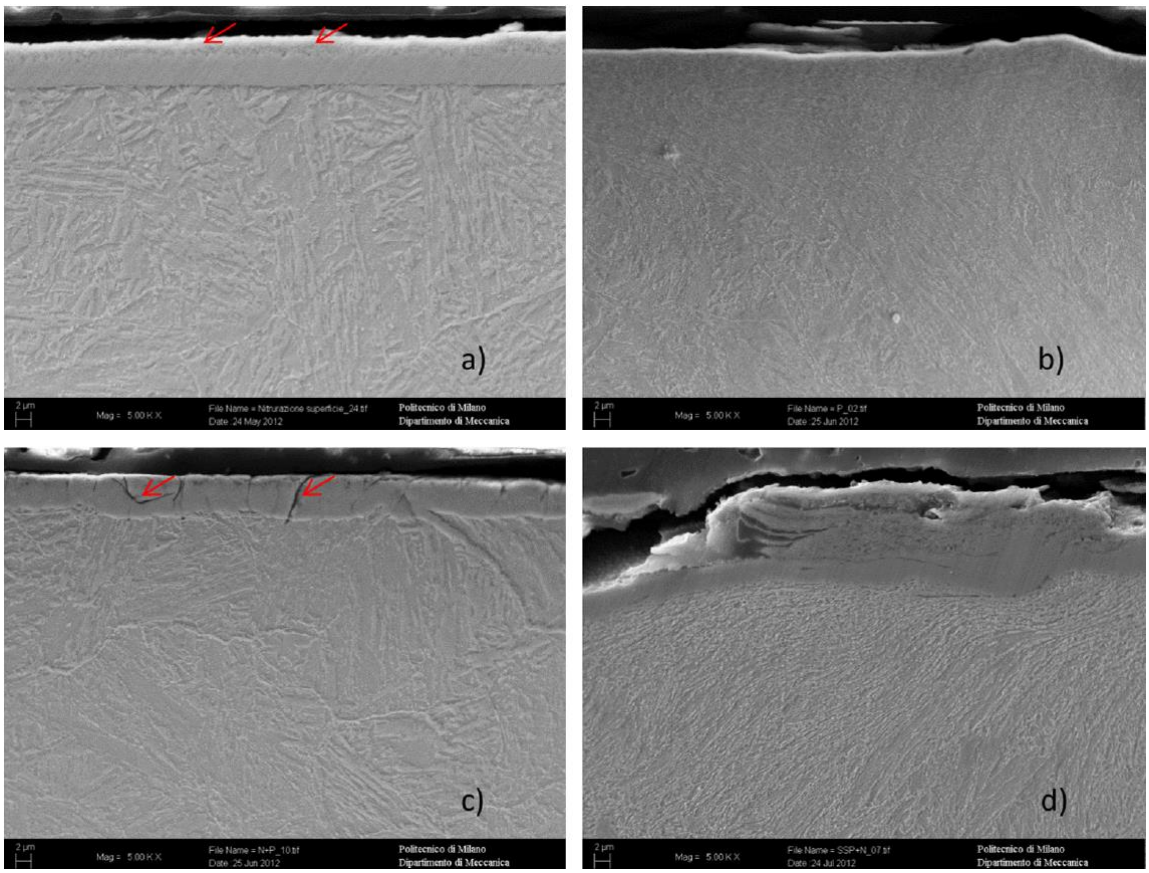

Figure 9-2. Cross sectional scanning microscopy of a) N, b) SSP, c) N+SSP and d) SSP+N specimens.

9.3 Hardening

Figure 9-3 depicts the variation of micro-hardness from the treated surface to the bulk material. Maximum value of micro-hardness was measured at the surface of all treated specimens and then it gradually decreased to core value. It is worth to notice that hardness improvement by severe shot peening, even if it is a severe plastic deformation, was by far smaller than nitriding.

Case depth after nitriding is a matter of convention. Technically it is defined to be the depth at which the hardness is 100 HV more than core hardness [136]. A hardness value of 10% above the core hardness has been also used in the literature to characterize the case depth after nitriding when the fatigue characteristics are regarded [137,138]. Therefore, this amount was also superimposed in the graph of Figure 9-3. According to this criterion the case depth after nitriding was measured to be approximately 500 μm. The combination of nitriding and severe shot

peening, regardless of the sequence, did not change the hardened layer depth. Nonetheless, this combination did improve the micro-hardness from surface up to 80 μm in depth. The maximum surface hardness is obtained when sever shot peening is performed after nitriding.

It was proven that the width of the diffraction peak at half of the maximum (FWHM) measured by XRD is able to reflect more aspects of surface work hardening which cannot be revealed by micro-hardness values [44,139]. FWHM appears to interest the only layer where the measurement is done. On the contrary, micro-hardness involves a finite thickness of material, and the results are an average value on the thickness of material where the indentation has been done. FWHM is related to the grain distortion, to the dislocation density and grain size. It is also assumed as an index of hardening of the material.

The in-depth FWHM distribution of all treated specimens is illustrated in Figure 9-4. The estimated depth of hardened layer by FWHM distribution is in a good agreement with that of obtained by micro-hardness distribution. Contrary to micro-hardness, near surface (up to 25 μm in depth) FWHM for Severe shot peened specimen is higher than nitrided specimen. The reason is that severe shot peening can drastically deform surface layers and accumulate plastic strain due to repeated impingements.

The beneficial effect of severe shot peening and nitriding combination to generate harder surface layer can be realized from FWHM distribution. In the case of severe shot peening prior to nitriding this improvement might be attributed to facilitated nitrogen diffusion through dense structure and fine grained layers generated after severe plastic deformation. The most enhanced FWHM occurred in the reverse treatment (N+SSP), however. This is due to the fact that a very hard target has been subjected to severe peening.

9.4 Residual stress

In depth residual stress distribution of all treated specimens is depicted in Figure 9-5. It should be mentioned that both longitudinal and circumferential residual stresses were measured. For all treated specimen the state of stress was quiet equi-biaxial. Thus one component of residual stress (longitudinal) was plotted here. Severe shot peening generated more compressive residual stress than nitriding. Indeed, both processes increase hardness and generate compressive residual stress. However, based on the result of this study, nitriding is mostly benefitted by increasing the hardness while shot peening is mostly benefited by generating compressive residual stress.

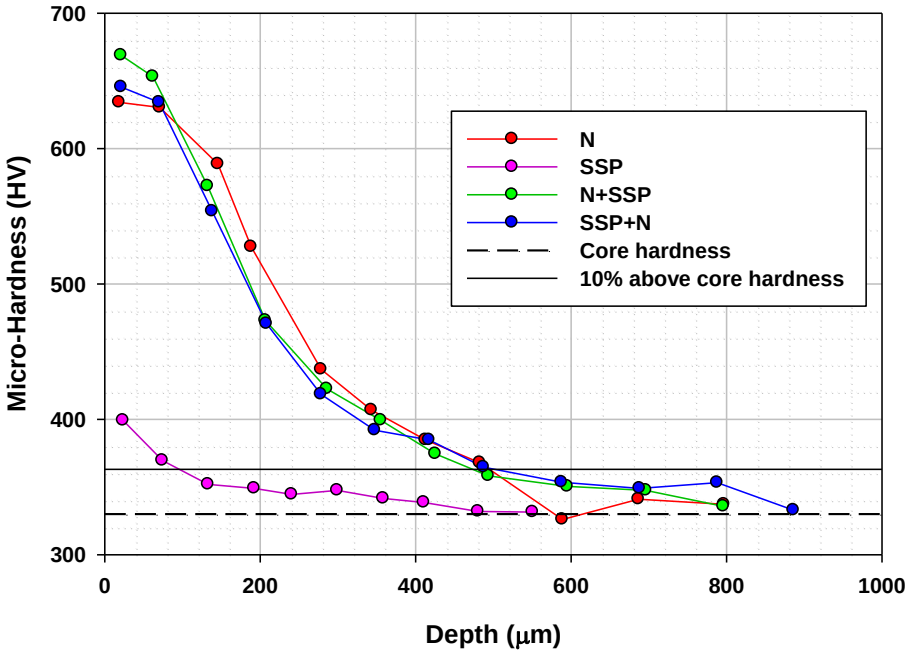

Figure 9-3. In depth micro-hardness distribution of all treated specimens.

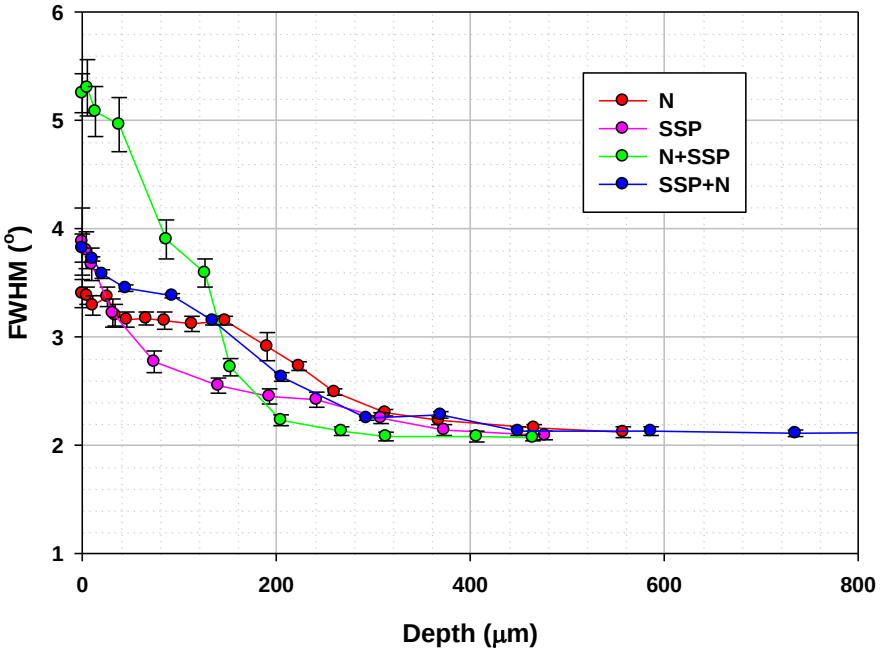

Figure 9-4. In depth FWHM distribution of all treated specimens.

The combination of nitriding and shot peening can be advantageous in terms of residual stress distribution. In the case of severe shot peening prior to nitriding, deeper compressed layer is produced as compared to the only nitriding. In the case of severe shot peening after nitriding, on the other hand, remarkable augmentation is achieved for surface and maximum compressive residual stress. Distribution of residual stress then is followed by a steeper reduction in this case with respect to the nitrided specimen.

9.5 Surface roughness

Table 9-1 shows the surface roughness parameters of all treated specimens. The parameters are based on the definition of ISO 4287 [90]. The arithmetic-mean value (R_a) can be considered as the representative parameter of surface roughness. It is interesting to note even if nitriding is not a mechanical treatment, it increased the roughness. This increment in the nitrided specimen can be attributed to the formation of pores at the top of the compound layer.

As shown in Table 9-1, severe shot peening has considerably increased the roughness. This is a well-recognized side effect of the shot peening process. Surface roughness of peened plus nitrided specimen is a little bit more than the roughness of peened specimen. This again affirms that nitriding alters the surface roughness. Surface roughness for nitrided plus peened specimen is not as high as the only peened specimen. This is due to the fact that in the latter case very hard nitrided layer is subjected to sever shot peening. Therefore, less deformation and eventually less surface roughness was generated.

9.6 Fatigue limit

Figure 9-6 shows the fatigue limit for as-received and all surface treated specimens. Fatigue limit of as-received specimen was 491 MPa. Severe shot peening increased the fatigue limit of specimens by 11.6 %. Surface roughness alteration, generating of compressive residual stresses and slight improvement of hardness were the main effects induced by severe shot peening. It seems that the detrimental effect of surface roughness masked part of the potential improvement that could be resulted by severe shot peening.

Nitriding was able to significantly increase the fatigue limit by 51.3%. It will be shown in the next section that fatigue crack initiated form the subsurface layer of nitrided specimens. The difference between shot peening and nitriding improvement could be related to harder and much less rough surface of the nitrided specimen that caused the fatigue crack to be shifted to the subsurface where the applied stress is less than surface.

It is worth to notice that the fatigue limit of the combined shot peened and nitrided specimens, regardless of sequence, was almost the same as the fatigue limit of nitrided specimen. Despite

the initial expectation of having a synergistic effect of the combination of these surface treatments, no further improvement in fatigue limit was obtained with respect to the only nitrided specimen. A justification is presented in the following sections.

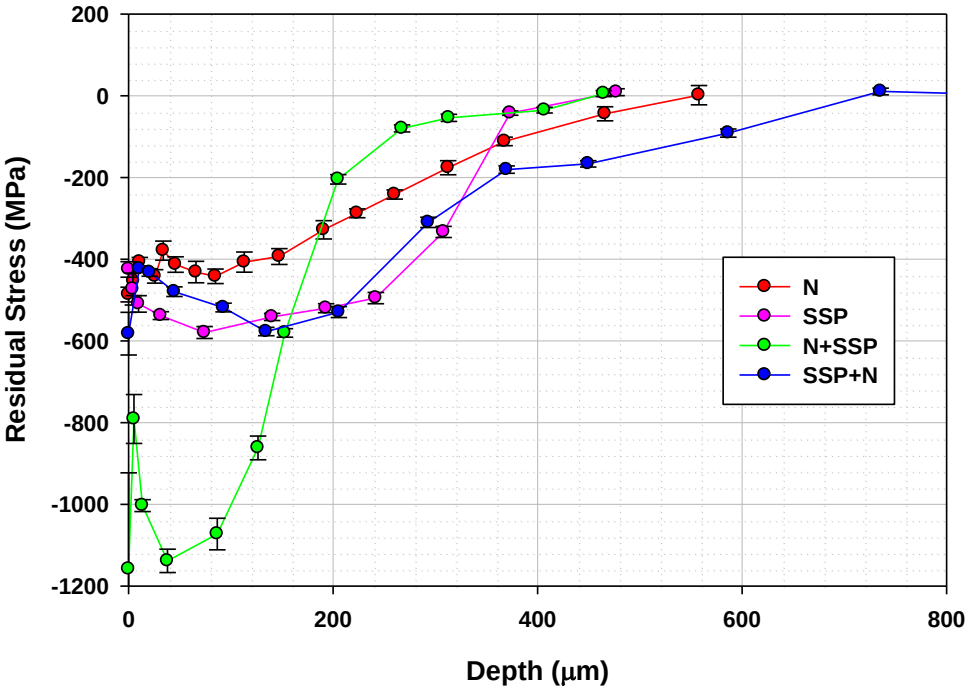

Figure 9-5. In depth residual stress distribution of all surface treated specimens.

Table 9-1. Surface roughness parameters of all treated specimens.

Treatment	I_r(mm)	I_n(mm)	R_a(μm)	R_q(μm)	R_z(μm)	R_t(μm)
AR	0.8	4	0.07	0.10	0.62	0.82
N	0.8	4	0.59	0.76	4.37	5.04
SSP	0.8	4	4.93	6.02	23.82	32.96
N+SSP	0.8	4	1.49	1.87	7.05	9.88
SSP+N	0.8	4	5.23	6.5	25.49	33.22

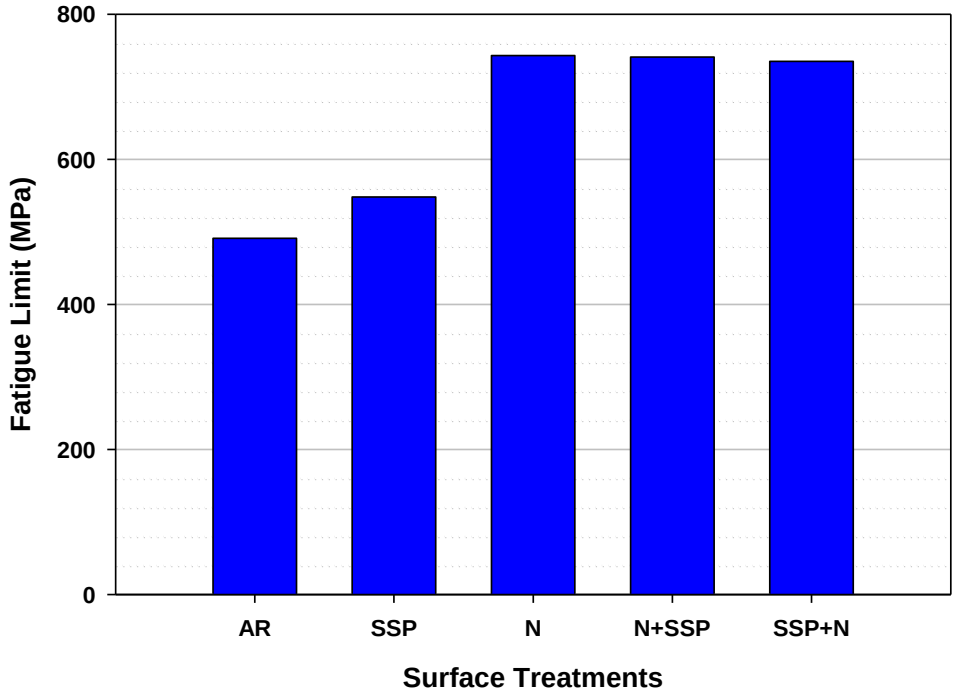

Figure 9-6. Fatigue limit of as-received and surface treated specimens.

9.7 Fractography

The fractured surface of all treated specimens was examined by SEM observation to assess the effect of different surface treatments on fatigue crack initiation and propagation. Figure 9-7 a shows the fractured surface of a nitrided specimen. The final fracture resulted from initiation and propagation of a subsurface, so called “fish eye” crack. It should be noted that fish eye crack feature has been observed in all broken nitrided specimens. The same fracture mechanism for nitrided specimen has been also reported elsewhere [140,141]. Bearing in mind that specimens were subjected to rotating bending loading condition, surface layers were exposed to higher applied stress than subsurface layers. However, fatigue crack has not originated from the surface. Indeed, crack initiation site was below the hardened layer produced by nitriding. Depth of hardened layer measured by micro-hardness test was around 500 μm and depth of compressed layer measured by XRD was approximately 550 μm. The depth of crack initiating site for nitrided specimens was extended up to 762 μm. This observation confirms that high hardness and compressive residual stress generated by nitriding put a great delay in surface crack initiation. It is well accepted that extrusion and intrusion pile up is responsible for crack initiation on the surface. However, in nitrided specimen extrusion and intrusion process is very limited by surrounding hard material and they could not be easily piled up [142].

The same fish eye crack feature, as illustrated in Figure 9-7 b and c was observed for both combinations of shot peening and nitriding, in all broken specimens except one SSP+N specimen. The depth of crack initiation sites for N+SSP and SSP+N were in the range of 565-819 μm and 521-847 μm respectively. It is the result of interest that notwithstanding the presence of surface micro crack in the compound layer of N+SSP and high surface roughness as well as some discontinues in the compound layer of SSP+N, the fatigue crack still originated from the subsurface layers. Indeed, the high compressive residual stress field prevented micro cracks and discontinuities to be further propagated.

For the severe shot peened specimens, on the other hand, fatigue crack initiated from the surface (Figure 9-7 d). Considering the existence of ultra-fine grained layer and high compressive residual stresses in the surface layers, the crack was also in this case expected to initiate from subsurface layers. Nonetheless, it seems that the deteriorating effect of high surface roughness on fatigue resistance has masked partly the beneficial effect of ultra-fine grained structures containing high compressive residual stress. Fractured surface of severe shot peened specimens also revealed that cracks initiated from more than one point on the surface. This is a typical feature of fatigue fracture not in smooth but in notched specimens. Bearing in mind that the tested specimens were smooth, it can be concluded that high surface roughness induced by severe shot peening acted like a notch during the fatigue test.

9.8 Local fatigue strength

Hardness and residual stress are two important parameters governing the fatigue behavior of steel. Local fatigue strength approach correlates the local fatigue strength to the hardness and residual stress distribution. This approach is most often applied for surface hardened material [84,143,144]. Local fatigue approach proposed by Kloos et al. [145] is implemented in this study but similar results are obtained if other local fatigue limit formulations are used. Local fatigue (σ_w), is considered to be a function of base fatigue limit (σ_{w0}), ultimate tensile strength (R_m), induced micro-hardness (HV), residual stress (σ_{res}), mean applied stress (σ_m), as well as applied relative stress gradient (X^*) by following relationships:

$$R_m = 3.29HV - 47 \qquad HV \leq 445 \qquad (9\text{-}1)$$

$$R_m = 4.02HV - 374 \qquad HV \succ 445 \qquad (9\text{-}2)$$

$$\sigma_{w0} = 1.27HV + 150 \qquad HV \leq 500 \qquad (9\text{-}3)$$

$$\sigma_{w0} = 785 \qquad HV \succ 500 \qquad (9\text{-}4)$$

$$X^* = \frac{1}{\sigma_{\max}} \cdot \frac{d\sigma}{dx} \qquad (9\text{-}5)$$

$$\sigma_w = \sigma_{w0}\left(1-\frac{\sigma_m+\sigma_{res}}{R_m}\right)\left(1+\sqrt{\frac{1600}{HV^2}X^*}\right) \qquad (9\text{-}6)$$

The local fatigue strength curves of all treated specimens are depicted in Figure 9-8. Straight lines represent different levels of applied bending stress. The intersection of applied stress with local fatigue curve represents the predicted site of crack initiation and the corresponding surface value indicates the predicted nominal fatigue limit by this method. It can be seen that theoretically fatigue cracks are most likely to initiate at the depth of 500-800 μm for all treated specimens. This is in a good agreement with experimental observation for N, N+SSP and SSP+N series. However, for severe shot peened specimens, unlike the prediction, all fatigue cracks initiated from the surface. This is due to high surface roughness induced by severe shot peening. It should be mentioned that surface roughness values are almost the same for SSP and SSP+N series. Nonetheless, fatigue crack initiated from the surface in the former case and from the subsurface layer in the latter case. This observation affirms the capability of the nitriding process to delay fatigue crack initiation phase by increasing surface hardness. The calculated fatigue limits are also in a good agreement with the measured ones for N, N+SSP and SSP+N series.

The fact that despite the increment in compressive residual stress and work hardening, subsequent or prior severe shot peening has not improved the fatigue limit of nitrided specimens can be clearly explained by distribution of local fatigue limit shown in Figure 9-8. High Improvement due to subsequent severe shot peening occurred at the surface and subsurface layers up to approximately 200 μm in depth. In the case of prior severe shot peening, major improvement occurred at subsurface layers up to the depth of 300 μm. Notwithstanding the crack initiation in the depth of 500 μm or even deeper, these improved regions were safe regions where the intersection of applied stress and local fatigue curve does not occur. Accordingly, for the smooth specimens to achieve further fatigue life improvement, nitriding should be combined with a treatment that is able to affect deeper than nitrided hardened layer. It is worth mentioning that in the case of notched specimens where stress gradient exists, fatigue cracks are most likely to initiate from the surface. Thus fatigue limit improvement can be expected when nitriding and severe shot peening is combined.

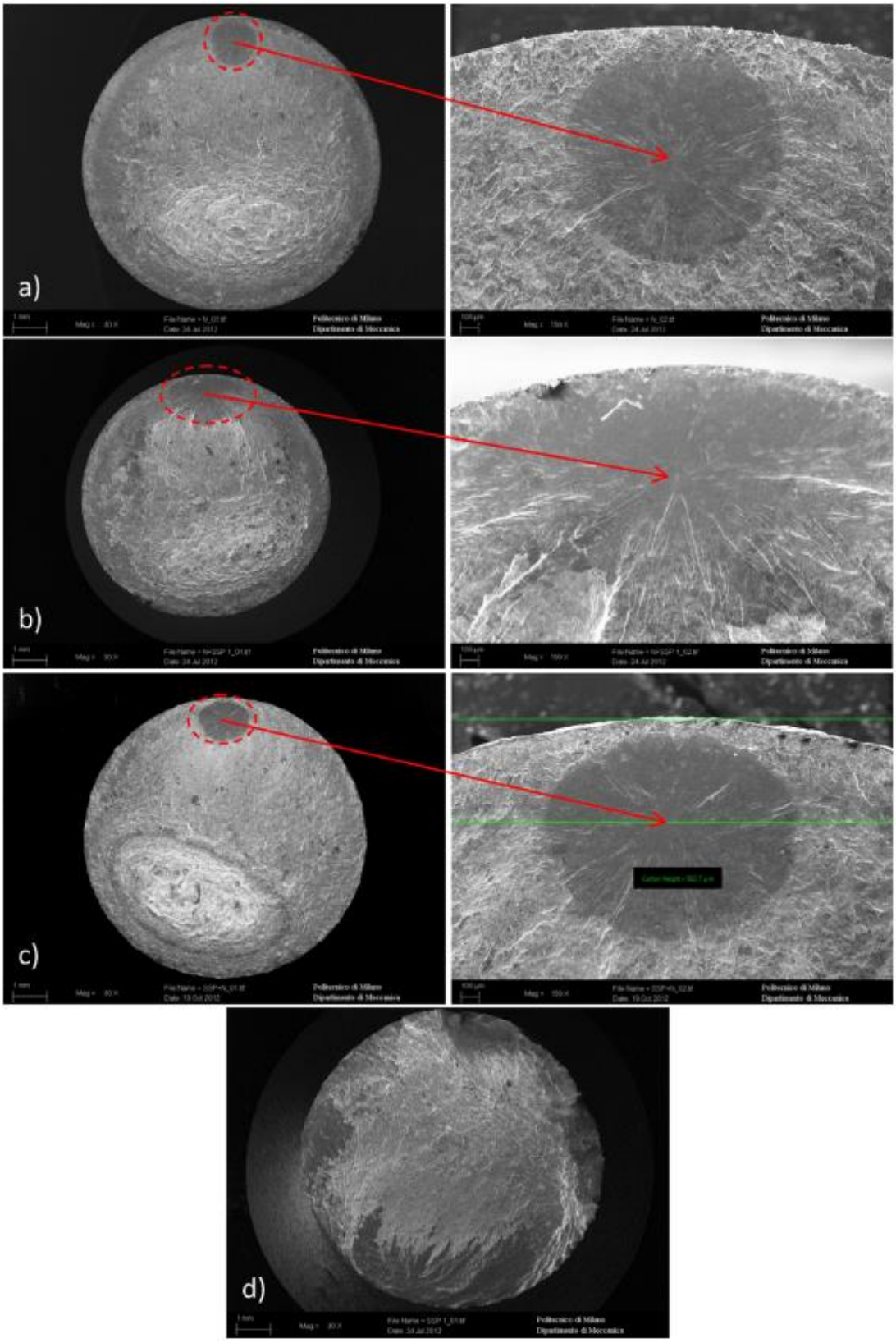

Figure 9-7. SEM fractography of surface treated samples: a) N, b) N+SSP, c) SSP+N and d) SSP.

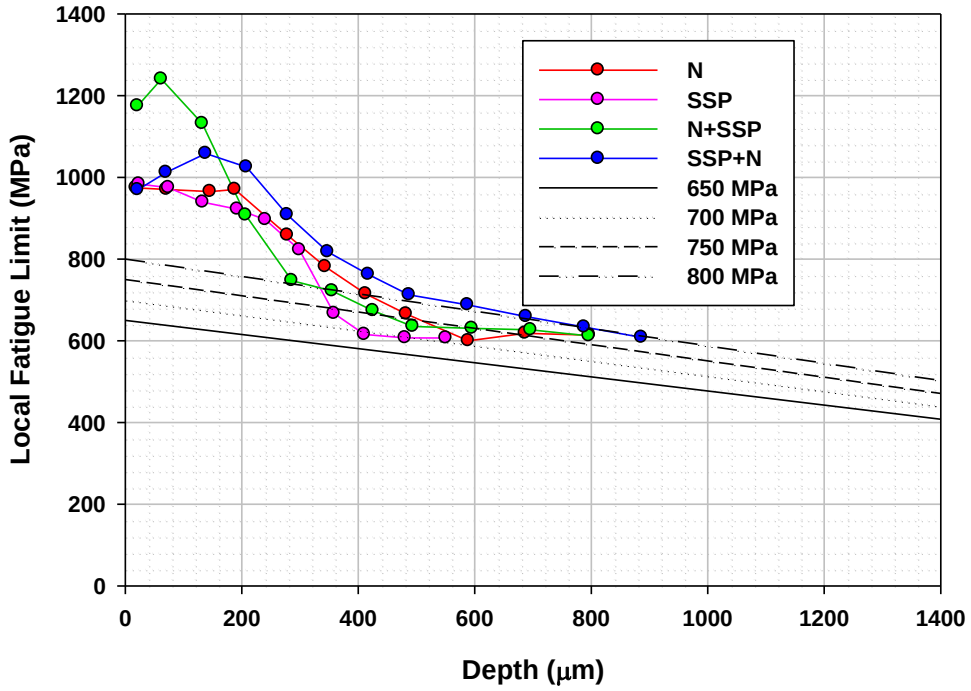

Figure 9-8. Local fatigue strength of surface treated specimens.

9.9 Conclusion

The effect of severe shot peening, nitriding and their combination considering both sequences (severe shot peening + nitriding and vice versa) on micro-structure, hardening, residual stress, surface roughness and fatigue limit of steel alloy was investigated. The following conclusions can be drawn on the basis of obtained results:

Subsequent severe shot peening suppressed the porous structure at the top of the compound layer formed after nitriding. The rest of compound layer, on the other hand, survived after peening. Nonetheless, it was damaged and some micro-cracks were formed. Performing severe shot peening prior to nitriding caused up to three times deeper compound layer with respect to the only nitrided specimen. This is due to the very dense structure and fine grained surface layer generated by severe plastic deformation during severe shot peening. The combination of nitriding and severe shot peening, regardless of the sequence, did not change the hardened layer depth. Nonetheless, this combination did improve the micro-hardness from surface up to 80 μm in depth. The maximum surface hardness is obtained when sever shot peening is performed after nitriding. Notwithstanding the high surface roughness, severe shot peening improved the fatigue limit by 11.6 %. Nitriding improved the fatigue limit by 51.3%. No further improvement was

obtained by the combination of severe shot peening and nitriding. For nitrided series (N, N+SSP, SSP+N) fatigue crack originated from sub-surface layers below the hardened layer. Fatigue crack initiation from the surface of severe shot peened specimens is attributed to the high induced surface roughness. Subsequent nitriding was able to displace the crack initiation site to the subsurface layers despite the presence of high surface roughness. With respect to only nitrided specimens, the combination of severe shot peening and nitriding enabled to improve local fatigue limit up to 200 μm in depth for N+SSP and 300 μm for SSP+N. However, since almost all fatigue cracks were likely to initiate at the depth of 500-800 μm, this combination did not succeed to improve the final fatigue limit.

10 Nitriding duration reduction

10.1 Introduction

Most studies on the application of a severe plastic deformation prior to nitriding were done on stainless steel. In chapter 9 the effect of combination of severe shot peening and nitriding on the fatigue limit of a high strength low alloy (HSLA) steel was investigated. The study was accomplished to shed light first on the applicability of this combination on HSLA steel and more importantly to find whether fatigue limit can be benefitted by this combination as much as surface hardness and case depth most often can. Based on the result, although prior severe shot peening caused up to three times deeper compound layer and produced deeper compressed layer, it was not able to further improve the fatigue limit of nitrided specimen. Local fatigue strength calculation revealed that the combination did improve the local fatigue strength up to 300 µm in depth. However, since fatigue cracks initiated below the hardened case (below 500 µm), the improvement was not seen in the final fatigue behaviour of the specimen. Therefore, the present study was designed to affirm even if the improvement did not contribute in the fatigue behaviour of smooth specimen; it exists and can be exploited in the form of nitriding duration reduction. Notwithstanding the high temperature required to perform nitriding, its duration reduction without affecting resultant mechanical characteristic and fatigue behaviour would be of great technical and scientific importance. To this end severe shot peened plus 7.5 h nitrided specimens are examined and compared with 15 h nitriding from the previous study. The results will be given under the label of SSP+N-7.5h for the present samples. The corresponding results of nitriding on the same sample and in the same atmosphere and temperature but for 15 h from the previous section were also added under the label of N-15h to affirm the improvement that can be obtained by prior severe shot peening.

10.2 Micro-structure

Overall view of the cross section by OM in Figure 10-1 shows formation of a very thin compound or white layer of few microns on the top surface. The constituents of this hard and brittle layer are ϒ’ (Fe_4N) and ε ($Fe_{2-3}N$) phases [135]. Beneath the compound layer the so-called diffusion zone with dispersed needle shape precipitates of ϒ’ in ferritic matrix as well as the solid solution of nitrogen in ferrite exists.

Formation of compound layer is more evident from the SEM image of the cross section shown in Figure 10-2. Depth of compound layer was measured to be in the range of 4-6 µm after nitriding with 15 h duration. Performing severe shot peening prior to nitriding caused the same deep compound layer to be created even if the subsequent nitriding duration was shortened to 7.5 h. This is due to the very dense structure and fine grained surface layer generated by severe plastic deformation during severe shot peening. This can be realized by the SEM image taken from the surface of severe shot peened specimen, illustrated in Figure 10-3. By severe shot peening much more defects and interfaces are generated in surface layers through repeating impingements.

With the proceeding of collisions, some areas approach to the critical condition of nanocrystallization and grain fragmentation below 100 nm occurs.

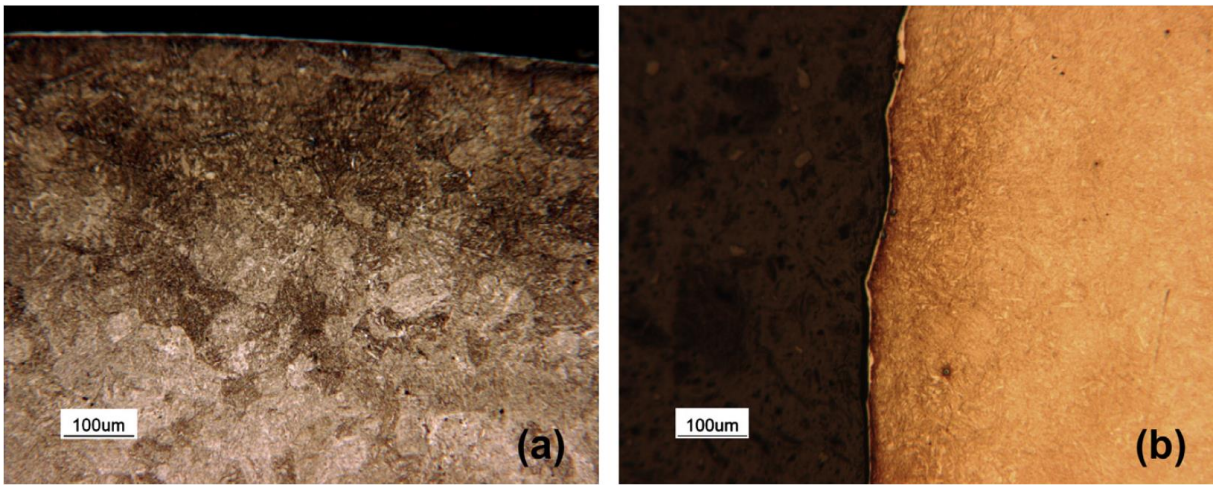

Figure 10-1. Cross sectional optical microscopy of a) N-15h, b) SSP+N-7.5h specimens.

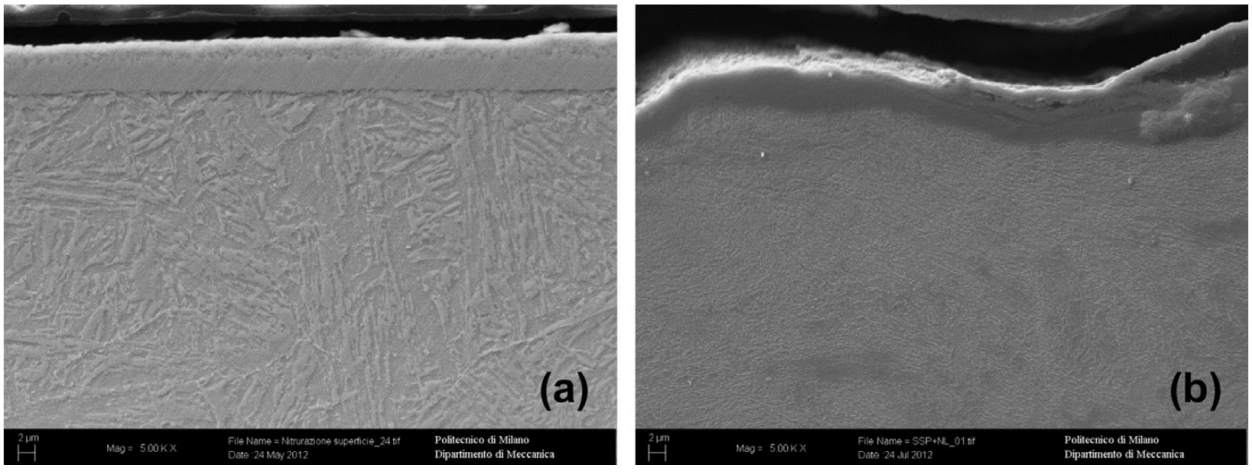

Figure 10-2. Cross sectional scanning microscopy of a) N-15h, b) SSP+N-7.5h specimens.

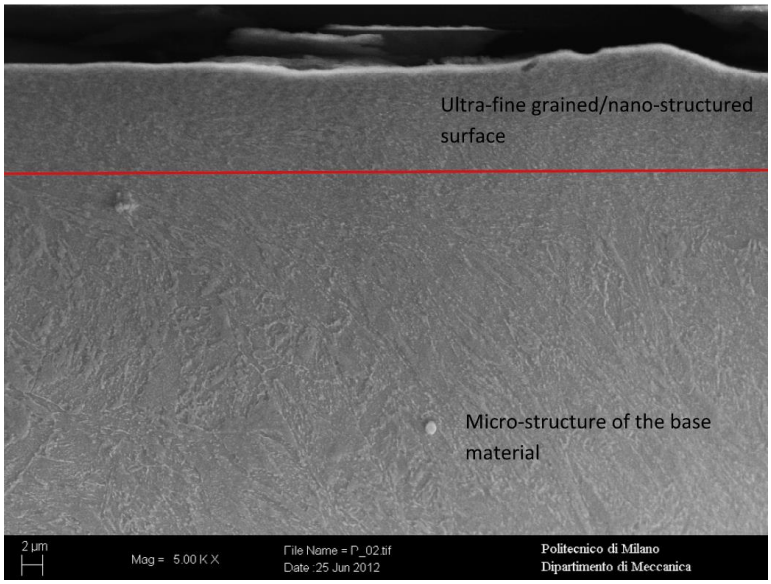

Figure 10-3. Cross sectional scanning microscopy of severe shot peened specimen.

10.3 Hardening

Figure 10-4 depicts the variation of micro-hardness from the treated surface to the bulk material. Maximum value of micro-hardness was measured at the surface of both treated specimens and then it gradually diminished to micro-hardness of the base material. Definition of case depth after nitriding is a matter of convention. Technically it is defined to be the depth at which the hardness is 100 HV more than core hardness [136]. A hardness value of 10% above the core hardness has been also used in the literature to characterize the case depth after nitriding when the fatigue characteristics are regarded [137,138]. Therefore, both values were superimposed in the graph. According to the first criterion the case depth produced after nitriding at 15 h was measured to be approximately 500 µm, while the case depth after severe shot peening and nitriding at 7.5 h is approximately 400 µm. According to the second criterion the case depth nitriding at 15 h is approximately 290 µm, while the case depth after severe shot peening and nitriding at 7.5 h is approximately 200 µm. It is clear that regardless of the convention, the case depth of SSP+N-7.5h is not as deep as the case depth of N-15h. However, it is interesting to note that the same surface micro-hardness was obtained for both treatments.

The width of the diffraction peak at half of the maximum (FWHM), measured by XRD, can be also assumed as an index of hardening. FWHM is able to reflect more aspects of surface work hardening which cannot be revealed by micro-hardness values [44,139]. The in-depth FWHM distribution of both treated specimens is illustrated in Figure 10-5. It is clear from the distribution that both treatments are able to produce hardened layers. The amount of FWHM at the surface of SSP+N-7.5h specimen is appreciably higher than the corresponding surface value of the N-15h specimens, even if shorter time was applied in the former case. This is due to ultra-fine

grained/nano-structured surface layers generated after severe deformation and accumulation of plastic strains by repeated impingements during severe shot peening.

The effectiveness of excellent properties generally induced by surface nanocrystallization processes highly depends on the thermal stability of the generated ultra-fine grained/nano-structured layers. By increasing the temperature, grain coarsening might happen which in turn tends to decrease the hardness. The higher level of surface FWHM for SSP+N-7.5h specimens, clearly affirm that ultra-fine grained structure generated by severe shot peening was quite stable after being subjected to 510° C for 7.5 h during subsequent nitriding.

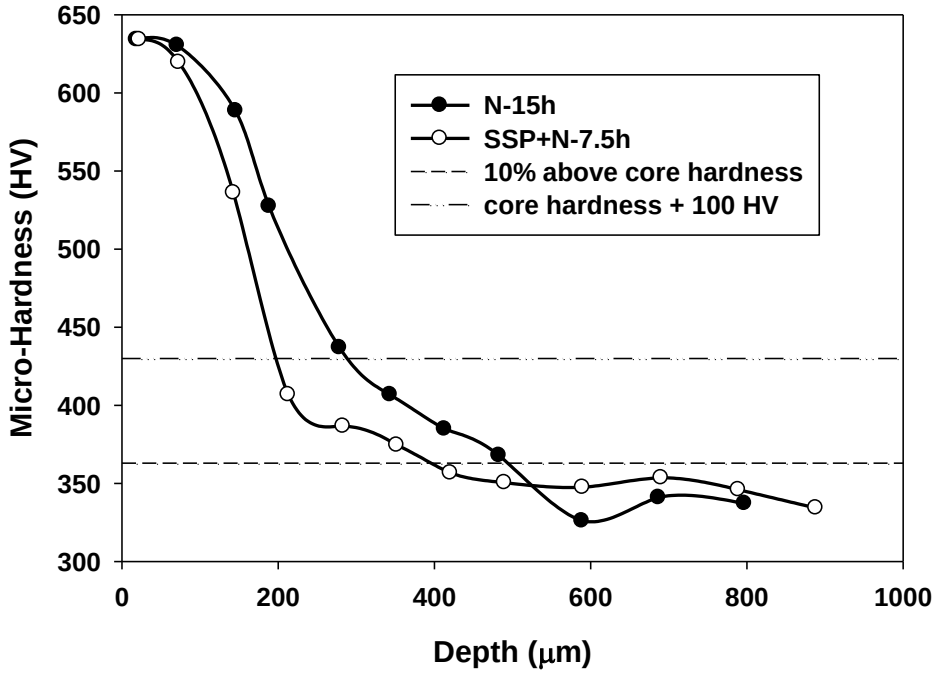

Figure 10-4. In depth micro-hardness distribution of the treated specimens.

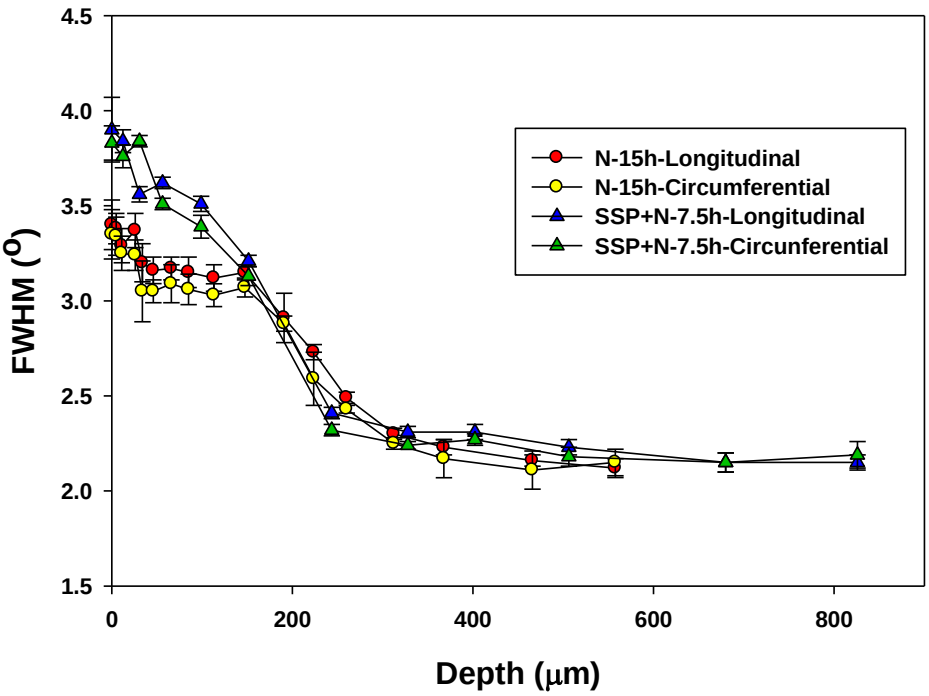

Figure 10-5. In depth FWHM distribution of the treated specimens.

10.4 Residual stress

In depth longitudinal and circumferential residual stress distribution of both treated specimens is depicted in Figure 10-6. Nitriding and its combination with severe shot peening generated equi-biaxial compressive residual stress state. From the surface up to 150 μm in depth, slightly higher compressive residual stresses were developed for the SSP+N-7.5h treated specimens with respect to the N-15h treated specimen. The increment of compressive residual stress for the hybrid treatments is more evident below 150 μm in depth up to to 680 μm where it vanishes. For instance, the increment of compressive residual stress by application of prior severe shot peening at the depth of 245 μm is nearly 65%. It is also worth noticing that the by application of prior severe shot peening depth of compressed layer increased by 22% even if the nitriding duration had been shortened by 50%.

10.5 Surface roughness

Table 10-1 shows the surface roughness parameters of all treated specimens. The parameters are based on the definition of ISO 4287 [90]. The arithmetic-mean value (R_a) is most often considered as the representative parameter of surface roughness. Nitriding increased the R_a value

of as-received specimens from 0.07 to 0.59 μm. The roughness increment by nitriding can be attributed to the formation of pores at the top of the compound layer which can be seen from Figure 10-2 a. The R_a value for the case of SSP+N-7.5h is eight times bigger than the corresponding value for the only nitrided specimen. This is a well-recognized side effect of the shot peening process especially when severe parameters are applied. The rough surface generated by severe shot peening can be clearly observed in the OM and SEM image shown in Figure 10-1 b and Figure 10-2 b respectively.

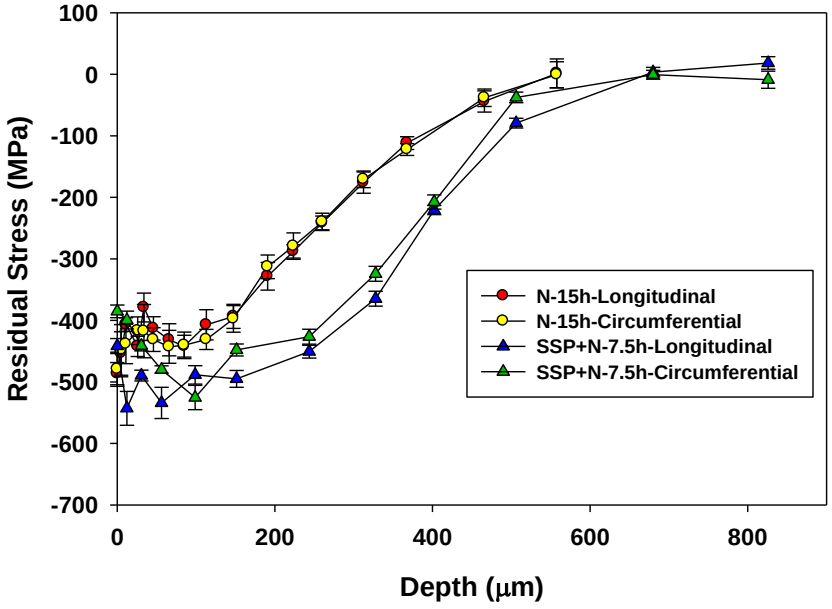

Figure 10-6. In depth residual stress distribution of all surface treated specimens.

Table 10-1. Surface roughness parameters of as-received and surface treated specimens.

Treatment	I_r(mm)	I_n(mm)	R_a(μm)	R_q(μm)	R_z(μm)	R_t(μm)
AR	0.8	4	0.07	0.10	0.62	0.82
N-15h	0.8	4	0.59	0.76	4.37	5.04
SSP+N-7.5h	0.8	4	4.72	5.93	23.67	32.96

10.6 Fatigue limit

Figure 10-7 shows the fatigue limit for as-received and both surface treated specimens. Fatigue limit of as-received specimen was 491 MPa. Nitriding significantly increased the fatigue limit of specimens by 51.3 %. It is interesting to note that severe shot peening plus nitriding,

notwithstanding the 50% duration reduction, was able to come up with the same level of fatigue limit or even with some slight improvement (54.7% with respect to the fatigue limit of the as-received specimens).

10.7 Fractography

The fractured surface of both treated specimens was examined by SEM observation to assess the effect of different surface treatments on fatigue crack initiation and propagation. Figure 10-8 a and b show the fractured surface of a nitrided and severe shot peened plus nitrided specimen respectively. The final fracture in both cases resulted from initiation and propagation of a subsurface, so-called "fish eye" crack. It should be noted that fish eye crack feature has been observed in all broken specimens. The same fracture mechanism for nitrided specimen has been also reported elsewhere [140,141]. Although in rotating bending loading condition, surface layers are exposed to higher levels of applied stress than the subsurface layers, fatigue crack has not originated from the surface but beneath the hardened layer produced by nitriding.

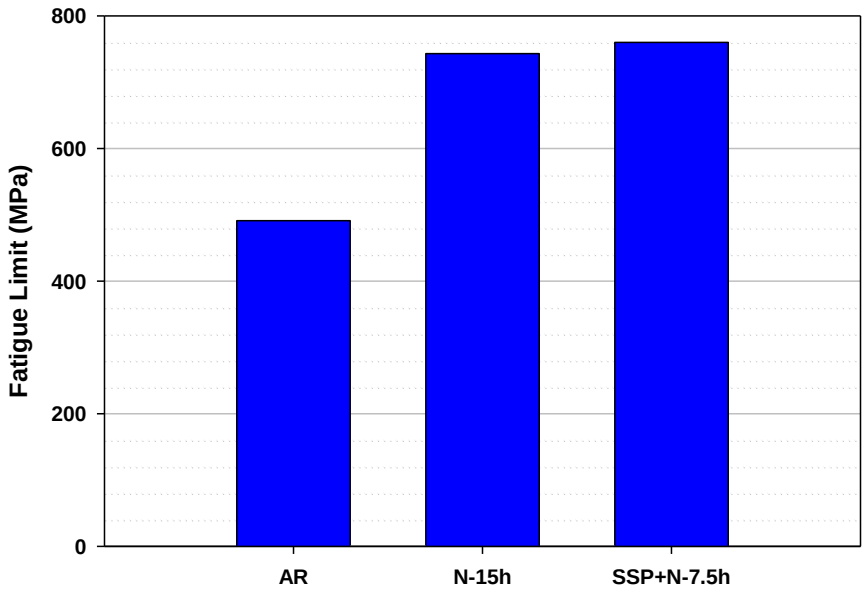

Figure 10-7. Fatigue limit of as-received and surface treated specimens.

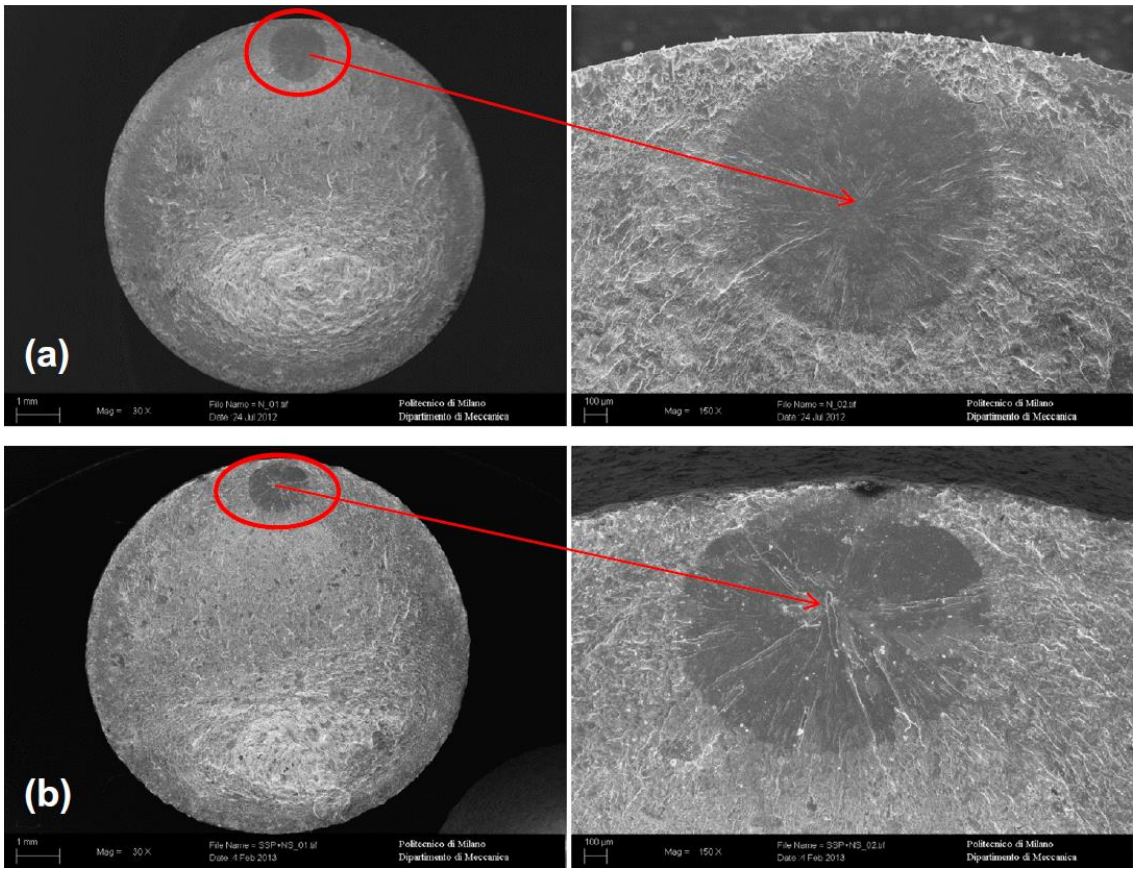

Figure 10-8. SEM fractography of surface treated samples: a) N-15h, b) SSP+N-7.5h.

10.8 Discussion

Kikuchi et al. [84] applied fine particle peening prior to gas nitriding of austenitic stainless steel and showed that hybrid treatment could further improve the fatigue strength as compared to nitriding only. Based on the result of chapter 9 nitriding at 15 h improved the fatigue limit by 51.3%. No further improvement in fatigue limit was obtained by the combination of severe shot peening and nitriding at 15 h. The two conclusions at the first glance may seem contradictory. But it is worth noticing that improvement in the former case occurred for notched specimen while no change in the latter case was found for smooth specimen. It was demonstrated that the combination did improve the local fatigue strength in the subsurface layer up to 300 µm. But since the critical site of crack initiation was located at the depth of 500 µm or even deeper, the local fatigue strength improvement could not contribute to increase the fatigue limit. If the same experiment was applied for notched specimens an increase in fatigue limit would have been expected. Because the critical site of initiation for notched specimens is always on the surface where, as shown, is benefitted by the hybrid treatment. In the present study combination of severe shot peening with nitriding at 7.5 h was assessed. 50% reduction of duration was

deliberately decided to affirm the fact that even for smooth specimens the improvement by hybrid treatment can be actively exploited and indeed it is in the form of duration reduction. According the available reports on the effect of nitriding duration on fatigue limit [146,147], an absolute progress in fatigue limit is obtained with prolonging nitriding. The reason is that effective depth increases with the process time. A deep nitrided case helps to move the crack initiation site further toward the core, thus a higher bending stress at the surface is required to create a sufficiently high stress in the subsurface to initiate a fatigue crack [138]. What was shown here by comparing the results for N-15h and SSP+N-7.5h is that 50% duration reduction did not come up with less fatigue limit as expected in the literature. This is absolutely due to the beneficial effect of prior severe shot peening.

In conventional nitriding of coarse-grained steel, nitrogen diffusion in the Fe lattice dominates. In the nano-crystalline structures, on the other hand, nitrogen mostly diffuses along grain boundaries with much faster diffusivity because of a much smaller activation energy (approximately half) compared with that for the lattice diffusion [82]. A clear and well-defined micro-structure change can be observed from the SEM image illustrating the surface of severe shot peened specimen (Figure 10-3). Ultrafine grained/nano-structured surface layers up to 10-12 µm was produced after sever shot peening. Such a micro-structure provides facilitated nitrogen diffusion through dense structure and generated fine grained layers during subsequent nitriding. There is generally a direct correlation between nitrogen concentration and increased surface micro-hardness in the nitriding process and micro-hardness profiling scaled fairly well with the nitrogen concentration [148–150]. A precise look at the micro-hardness distribution (Figure 10-4) affirms that the resultant micro-hardness at the very top surface for N-15h and SSP+N-7.5h is quite the same. Furthermore, the depth of compound layer, shown in the SEM image of Figure 10-2 is quite the same for both specimens. These two confirm that the ultrafine grained/nano-structured surface layers generated after sever shot peening increased the kinetic of nitrogen diffusion in such a way that the nitriding with 50% time reduction ended up with the same micro-hardness and thus nitrogen concentration in the affected zone. Micro-hardness difference for both treated specimens is not appreciable up to 70 µm. A clear deviation between the two micro-hardness distributions appears, nonetheless, by going further in depth. This is due to the fact that severe shot peening was able to refine the micro-structure up to a limited depth after which the advantages of refined micro-structure cannot be taken in the subsequent nitriding. Eventually, as can be seen in the micro-hardness distribution, the hardened layer in the N-15h specimens is deeper than SSP+N-7.5h specimens. This is also affirmed by the OM observation shown in Figure 10-1.

Rotating bending fatigue tests demonstrated that the same level of improvement can be obtained by application of severe shot peening before nitriding while nitriding duration is reduced. In both N-15h and SSP+N-7.5h specimens, fatigue cracks initiated form the sub-surface layers below 500 µm in depth for all broken specimens. It is well accepted that extrusion and intrusion pile up is responsible for crack initiation on the surface during fatigue. However, in both treated

specimen extrusion and intrusion process is very limited by surrounding hard material and they could not be easily piled up [142]. This behavior is even more interesting in the case of severely peened specimens where surface roughness is 8 times bigger than only nitrided specimens. The surface micro-hardness increased sufficiently by subsequent nitriding that despite the presence of high surface roughness and potential sites of crack initiation, the initiation site shifted to the sub-surface layers. Furthermore, highly distorted structure of surface layer of severely peend and nitride specimens in comparison with only nitrided ones, which can be clearly realized from the FWHM distribution and SEM image, could play a positive role to prevent the initiation of fatigue cracks from the surface.

Crack initiation most likely occurs where applied stress exceeds the local fatigue strength which generally lies in the sub-surface layers below the hardened case. Local fatigue strength is a function of compressive residual stress and micro-hardness for a given material. In the present work, although the depth of hardened layer is not exactly the same for both specimens, the same average crack initiation depth was found in both cases. This can be attributed to the fact that, as shown in Figure 10-6, deeper compressive residual stress was created for SSP+N7.5h. In another word, slightly shallower hardened layer of SSP+N7.5h was compensated by slightly deeper compressed layer so that the final crack initiation site and fatigue limit was the same for both specimens.

10.9 Conclusion

The effect of surface nanocrystallization by prior severe shot peening aimed to shorten subsequent nitriding on micro-structure, hardening, residual stress, surface roughness, fatigue and fracture behavior of low alloy steel was investigated. The following conclusions can be drawn on the basis of obtained results: Ultrafine grained/nano-structured surface layers up to 10-12 µm was successfully generated by sever shot peening. Such a structure provided facilitated nitrogen diffusion through dense structure and generated fine grained layers during subsequent nitriding. In comparison with the only nitrided specimen, performing severe shot peening prior to nitriding caused the same deep compound layer to be created; even if the nitriding duration was shortened by 50%. In comparison with the only nitrided specimen, the same surface micro-hardness was obtained by application of prior severe shot peening despite 50% reduction of subsequent nitriding duration. The higher level of surface FWHM for severe shot peened plus nitrided specimens with respect to only nitrided ones, clearly affirms that ultra-fine grained structure generated by severe shot peening was quite stable after being subjected to 510° C for 7.5 h during subsequent nitriding. Nitriding at 15h significantly increased the fatigue limit of steel specimens by 51.3 %. It is interesting to note that severe shot peening plus nitriding, notwithstanding the 50% duration reduction, was able to come up with the same level of fatigue limit or even with some slight improvement to 54.7%. Based on the results demonstrated in this

paper, nitriding duration can be successfully reduced without losing improvements in mechanical characteristics and fatigue behavior if a suitable prior severe shot peening is performed.

Part V Conclusion

11 Conclusion and future work

In spite of evidences of successful surface nanocrystallization by peening, reported in literature, the knowledge cannot be used yet in order to engineer the surface and design a desired nanostructure. This is mainly due to lack of systematic studies and lack of a numerical framework enabling to predict and simulate the process of grain refinement during severe peening. To address these issues, a systematic study of surface nanocrystallization by air blast severe shot peening was designed in the present work. Different coverage was adopted to span different classes of peening i.e. conventional and severe shot peening. TEM observation and measurement of grain/cell size affirms that grain refinement to less than 100 nm is certainly feasible by air blast severe shot peening. The following conclusions can be drawn:

- A numerical framework was proposed to simulate all aspects of peening, i.e. surface roughness evolution, generation of compressive residual stress and simulation of grain refinement with the special attention on prediction of grain/cell size at the surface and its gradient towards the subsurface layer. The first two have been simulated using finite element method. To simulate grain refinement, a dislocation density model was linked to finite element model.
- Residual stress and surface roughness evolution simulated by finite element technique were presented and compared with the experimental measurements. Good agreement between simulation and experiment demonstrates the model is reliable enough such that its output can be used as an input for the dislocation density models.
- After full coverage, depth of compressed layer gradually increases while the state of residual stress near the surface does not vary considerably. Roughness sharply increases in early stage of peening till the coverage is 20%. In high coverage, however, roughness evolution shows a saturation behavior.
- Maximum plastic strain and critical refinement after a single impingement occurs in the immediate subsurface layer near the indentation edge where material piles up. Shot velocity was found to be the most influential processing parameter for structural refinement as compared with media size or media hardness.
- A sharp increase of dislocation density and considerable refinement were found to occur at the early stages of peening. It was affirmed by numerical simulation that subdivision of cell into less than 100 nm is obviously feasible at high coverage by severe shot peening.
- Nano-sized grains are observed at the top surface of severely deformed specimen (1000% and 1300% coverage). For 650% coverage the surface grains are in the ultra-fine regime. The average grain sizes measured by TEM at the surface are 370, 160 and 130 nm for 650%, 1000% and 1300% coverage respectively.
- TEM micrographs clearly affirm that the higher the coverage is the smaller the cell/grain size that is formed at the various depths of the treated specimens.

- Comparison of simulated and experimentally measured cell size clearly affirms that the proposed numerical framework is able to simulate surface nanocrystallization. This is the first numerical framework of its kind to simulate surface nanocrystallization by severe shot peening.
- Surface nanocrystallization in the present material is accompanied by dissolution of M_3C cementite from more than 200 nm long plate to small particles (less than 50 nm) of spherical shape. Precipitation of nano-sized particle, M_2C type carbides, was also found to occur during surface nanocrystallization by severe shot peening. Both phenomena could contribute to improve the mechanical properties of the nano-structured surface.

It is well known that while the use of mechanical treatments is able to generate an effective field of compressive residual stresses and, if severe parameters are used, to cause grain refinement, thermochemical treatments are able to increase the surface hardness. This justifies the interest in developing combined treatments, able to achieve all the just mentioned factors. The second line that is followed by the present research is to affirm and to exploit the benefits of nano-structured surface, given the fact that diffusion along nano-sized grains is much more enhanced in comparison with the diffusion through coarse grains. Therefore, the effect of severe shot peening, nitriding and their combination considering both sequences (severe shot peening + nitriding and vice versa) on micro-structure, hardening, residual stress, surface roughness and fatigue limit of steel alloy was investigated. The following conclusions can be drawn on the basis of obtained results:

- Subsequent severe shot peening suppressed the porous structure at the top of the compound layer formed after nitriding. The rest of compound layer, on the other hand, survived after peening. Nonetheless, it was damaged and some micro-cracks were formed.
- Performing severe shot peening prior to nitriding caused up to three times deeper compound layer with respect to the only nitrided specimen. This is due to the very dense structure and fine grained surface layer generated by severe plastic deformation during severe shot peening.
- Hardness improvement by severe shot peening, even if it is a severe plastic deformation, was by far smaller than nitriding.
- Contrary to micro-hardness, near surface (up to 25 μm in depth) FWHM for severe shot peened specimen is higher than nitrided specimen.
- The estimated depth of hardened layer by FWHM distribution is in a good agreement with that of obtained by micro-hardness distribution.
- In the case of severe shot peening prior to nitriding, deeper compressed layer is produced as compared to the only nitriding. In the case of severe shot peening after nitriding, on the

other hand, remarkable augmentation is achieved for surface and maximum compressive residual stress.

- Even if nitriding is not a mechanical treatment, it increased the surface roughness (R_a) of as-received sample from 0.07 μm to 0.59 μm and roughness of the peened sample from 4.93 μm to 5.23 μm. Severe shot peening tremendously raised surface roughness.
- Notwithstanding the high surface roughness, severe shot peening improved the fatigue limit by 11.6 %.
- Nitriding improved the fatigue limit by 51.3%. No further improvement was obtained by the combination of severe shot peening and nitriding.
- The combination of nitriding and severe shot peening, regardless of the sequence, did not change the hardened layer depth. Nonetheless, this combination did improve the micro-hardness from surface up to 80 μm in depth. The maximum surface hardness is obtained when sever shot peening is performed after nitriding.
- For nitrided series (N, N+SSP, SSP+N) fatigue crack originated from sub-surface layers below the hardened layer. Fatigue crack initiation from the surface of severe shot peened specimens is attributed to the high induced surface roughness. Subsequent nitriding was able to displace the crack initiation site to the subsurface layers despite the presence of high surface roughness.
- With respect to only nitrided specimens, the combination of severe shot peening and nitriding enabled to improve local fatigue limit up to 200 μm in depth for N+SSP and 300 μm for SSP+N. However, since almost all fatigue cracks were likely to initiate at the depth of 500-800 μm, this combination did not succeed to improve the final fatigue limit. In order to achieve further improvement on the fatigue limit of nitrided smooth specimen, this is a key factor, that nitriding should be combined with another surface treatment enabling to affect deeper than the hardened layer produced by nitriding.
- Although the local fatigue strength improvement by combination of severe shot peening and 15 h nitriding could not eventually contribute in further increasing the fatigue limit of high strength low alloy steel smooth specimens as compared to only 15 h nitriding; combination of severe shot peening with nitriding at 7.5 h affirmed that improvement by hybrid treatment can be actively exploited in the form of duration reduction.
- Ultrafine grained/nano-structured surface was successfully generated by sever shot peening. Such a structure provided facilitated nitrogen diffusion through dense structure and generated fine grained layers during subsequent nitriding. In comparison with the only nitride specimen, performing severe shot peening prior to nitriding caused the same deep compound layer to be created even if the nitriding duration was shortened by 50%.
- In comparison with the only nitrided specimen, the same surface micro-hardness was obtained by application of prior severe shot peening despite 50% reduction of subsequent nitriding duration.

- The higher level of surface FWHM for severe shot peened plus nitrided specimens with respect to only nitrided ones, clearly affirm that ultra-fine grained structure generated by severe shot peening was quite stable after being subjected to 510° C for 7.5 h during subsequent nitriding.
- Nitriding and its combination with severe shot peening generated equi-biaxial compressive residual stress state. Higher compressive residual stresses and deeper compressed layer were developed for the combined severe shot peened and nitrided specimens with respect to the only nitrided specimen.
- Nitriding at 15h significantly increased the fatigue limit of specimens by 51.3 %. It is interesting to note that severe shot peening plus nitriding, notwithstanding the 50% duration reduction, was able to come up with the same level of fatigue limit or even with some slight improvement to 54.7%.
- Diffusion layer for nitriding at 15h was deeper than severe shot peening plus nitriding at 7.5h. This is due to the fact that severe shot peening was able to refine the micro-structure up to a limited depth after which the advantages of refined micro-structure cannot be taken in the subsequent nitriding. This deficiency, however, was completely compensated by deeper compressed layer in the combined treatment and eventually fatigue behavior was almost identical.
- Based on the results demonstrated in this paper, nitriding duration can be successfully reduced without losing improvements in mechanical characteristics and fatigue behavior if a suitable prior severe shot peening is performed.

This work has, hopefully, opened new doors to further investigation of severe shot peening process and its combination with nitriding. The following items are suggested as future steps, which can be taken in order to broaden the horizon of the knowledge in the field:

- It was shown that surface nanocrystallization in the present material is accompanied by dissolution of M_3C cementite and precipitation of nano-sized particle. As both phenomena could contribute to improve the mechanical properties of the nano-structured surface mechanical characterization of the top surface layer by nano-indentation could be an interesting subject for further investigation. Both detected phenomena could potentially contribute to increase hardness and delay fatigue crack initiation. Further investigation, however, is needed to gather enough evidences in order to distinguish the benefit coming from grain refinement with the benefit coming from dissolution of cementite and precipitation of nano-sized particles.
- Numerical framework developed in the present research aims at predicting residual stress, roughness and cell size evolution during severe shot peening. Another interesting micro-structural parameter is misorientation. Accumulation of misorientation causes dislocation cells transform to new grains. An extension to the numerical framework in order to predict misorientation could be of great interest.

- The combination of severe shot peening and nitriding enabled to improve local fatigue limit, it was able to reduce nitriding duration without sacrificing fatigue limit and mechanical characteristics. However, further improvement in fatigue limit of nitride specimens was not obtained. In order to achieve further improvement on the fatigue limit of nitrided smooth specimen, it is suggested that nitriding to be combined with another surface treatment enabling to affect deeper than the hardened layer produced by nitriding. One example could be deep rolling. Combination of deep rolling and nitriding could be an interesting subject for further investigation.

Bibliography

[1] Gleiter H. Nanocrystalline materials. Prog Mater Sci 1989;33:223–315.

[2] Kumar KS, Van Swygenhoven H, Suresh S. Mechanical behavior of nanocrystalline metals and alloys. Acta Mater 2003;51:5743–74.

[3] Meyers MA, Mishra A, Benson DJ. Mechanical properties of nanocrystalline materials. Prog Mater Sci 2006;51:427–556.

[4] Haas V, Gleiter H, Birringer R. Synthesis of nanostructured materials by the use of a thermophoretic forced flux system. Scr Metall Mater 1993;28:721–4.

[5] Sanders PG, Fougere GE, Thompson LJ, Eastman JA, Weertman JR. Improvements in the synthesis and compaction of nanocrystalline materials. Nanostructured Mater 1997;8:243–52.

[6] Suryanarayana C. Mechanical alloying and milling. Prog Mater Sci 2001;46:1–184.

[7] Eckert J, Holzer III JC, Krill CE, Johnson WL. Structural and thermodynamic properties of nanocrystalline fcc metals prepared by mechanical attrition. J Mater Res 1992;7:1751–61.

[8] Shen YF, Lu L, Lu QH, Jin ZH, Lu K. Tensile properties of copper with nano-scale twins. Scr Mater 2005;52:989–94.

[9] Erb U. Electrodeposited nanocrystals: Synthesis, properties and industrial applications. Nanostructured Mater 1995;6:533–8.

[10] Lu K. Nanocrystalline metals crystallized from amorphous solids: Nanocrystallization, structure, and properties. Mater Sci Eng R Reports 1996;16:161–221.

[11] Lu K, Wang JT, Wei WD. A new method for synthesizing nanocrystalline alloys. J Appl Phys 1991;69:522–4.

[12] Nicolaus MM, Sinning H-R, Haessner F. Crystallization behaviour and generation of a nanocrystalline state from amorphous Co33Zr67. Mater Sci Eng A 1992;150:101–12.

[13] Tong HY, Wang JT, Ding BZ, Jiang HG, Lu K. The structure and properties of nanocrystalline Fe78B13Si9 alloy. J Non Cryst Solids 1992;150:444–7.

[14] Valiev RZ, Estrin Y, Horita Z, Langdon TG, Zehetbauer MJ, Zhu YT. Producing bulk ultrafine-grained materials by severe plastic deformation. JOM 2006;58:33–9.

[15] Valiev RZ, Langdon TG. Principles of equal-channel angular pressing as a processing tool for grain refinement. Prog Mater Sci 2006;51:881–981.

[16] Segal VM. Materials processing by simple shear. Mater Sci Eng A 1995;197:157–64.

[17] Zhilyaev AP, Langdon TG. Using high-pressure torsion for metal processing: Fundamentals and applications. Prog Mater Sci 2008;53:893–979.

[18] Saito Y, Utsunomiya H, Tsuji N, Sakai T. Novel ultra-high straining process for bulk materials development of the accumulative roll-bonding (ARB) process. Acta Mater 1999;47:579–83.

[19] Chen J, Lu L, Lu K. Hardness and strain rate sensitivity of nanocrystalline Cu. Scr Mater 2006;54:1913–8.

[20] Dao M, Lu L, Asaro RJ, De Hosson JTM, Ma E. Toward a quantitative understanding of mechanical behavior of nanocrystalline metals. Acta Mater 2007;55:4041–65.

[21] Trelewicz JR, Schuh CA. The Hall-Petch breakdown in nanocrystalline metals: A crossover to glass-like deformation. Acta Mater 2007;55:5948–58.

[22] Ma E. Instabilities and ductility of nanocrystalline and ultrafine-grained metals. Scr Mater 2003;49:663–8.

[23] Youssef KM, Scattergood RO, Murty KL, Horton JA, Koch CC. Ultrahigh strength and high ductility of bulk nanocrystalline copper. Appl Phys Lett 2005;87.

[24] Schwaiger R, Moser B, Dao M, Chollacoop N, Suresh S. Some critical experiments on the strain-rate sensitivity of nanocrystalline nickel. Acta Mater 2003;51:5159–72.

[25] Valiev RZ, Alexandrov I V, Zhu YT, Lowe TC. Paradox of strength and ductility in metals processed by severe plastic deformation. J Mater Res 2002;17:5–8.

[26] Wang YM, Ma E. Three strategies to achieve uniform tensile deformation in a nanostructured metal. Acta Mater 2004;52:1699–709.

[27] Wang YM, Ma E. On the origin of ultrahigh cryogenic strength of nanocrystalline metals. Appl Phys Lett 2004;85:2750–2.

[28] Hanlon T, Kwon Y-N, Suresh S. Grain size effects on the fatigue response of nanocrystalline metals. Scr Mater 2003;49:675–80.

[29] Hanlon T, Tabachnikova ED, Suresh S. Fatigue behavior of nanocrystalline metals and alloys. Int J Fatigue 2005;27:1147–58.

[30] Suresh S. Fatigue crack deflection and fracture surface contact: Micromechanical models. Metall Trans A 1985;16:249–60.

[31] Han Z, Lu L, Lu K. Dry sliding tribological behavior of nanocrystalline and conventional polycrystalline copper. Tribol Lett 2006;21:45–50.

[32] Bellemare S, Dao M, Suresh S. The frictional sliding response of elasto-plastic materials in contact with a conical indenter. Int J Solids Struct 2007;44:1970–89.

[33] Tao NR, Sui ML, Lu J, Lua K. Surface nanocrystallization of iron induced by ultrasonic shot peening. Nanostructured Mater 1999;11:433–40.

[34] Lu K, Lu J. Surface nanocrystallization (SNC) of metallic materials-presentation of the concept behind a new approach. J Mater Sci Technol 1999;15:193–7.

[35] Baiker S, McIntyre P. Shot peening: a dynamic application and its future. Metal finishing news; 2009.

[36] Almen JO, Black PH. Residual stresses and fatigue in metals. McGraw-Hill; 1963.

[37] Marsh KJ, Services EMA. Shot Peening: Techniques and Applications. Engineering Materials Advisory Services Limited; 1993.

[38] Farrahi GH, Lebrun JL, Couratin D. Effect of shot peening on residual stress and fatigue life of a spring steel. Fatigue Fract Eng Mater Struct 1995;18:211–20.

[39] Kobayashi M, Matsui T, Murakami Y. Mechanism of creation of compressive residual stress by shot peening. Int J Fatigue 1998;20:351–7.

[40] Wang S, Li Y, Yao M, Wang R. Compressive residual stress introduced by shot peening. J Mater Process Technol 1998;73:64–73.

[41] Guagliano M. Relating Almen intensity to residual stresses induced by shot peening: A numerical approach. J Mater Process Technol 2001;110:277–86.

[42] Torres MAS, Voorwald HJC. An evaluation of shot peening, residual stress and stress relaxation on the fatigue life of AISI 4340 steel. Int J Fatigue 2002;24:877–86.

[43] Miller KJ. Metal fatigue. Past, current and future. Proc Inst Mech Eng Part C J Mech Eng Sci 1991;205:291–304.

[44] Fernandez Pariente I, Guagliano M. About the role of residual stresses and surface work hardening on fatigue ΔKth of a nitrided and shot peened low-alloy steel. Surf Coatings Technol 2008;202:3072–80.

[45] SAE Standard J2277 Shot Peening Coverage, Developed by Surface Enhancement 660 Committee. 2003.

[46] Kirk D, Abyaneh M. Theoretical basis of shot peening coverage control. 5th Int. Conf. shot Peen., 1993, p. 183–90.

[47] Avrami M. Kinetics of phase change. I: General theory. J Chem Phys 1939;7:1103–12.

[48] Wang XY, Li DY. Mechanical and electrochemical behavior of nanocrystalline surface of 304 stainless steel. Electrochim Acta 2002;47:3939–47.

[49] Wang XY, Li DY. Mechanical, electrochemical and tribological properties of nano-crystalline surface of 304 stainless steel. Wear 2003;255:836–45.

[50] Wang L, Li DY. Mechanical, electrochemical and tribological properties of nanocrystalline surface of brass produced by sandblasting and annealing. Surf Coatings Technol 2003;167:188–96.

[51] Jiang XP, Wang XY, Li JX, Li DY, Man C-S, Shepard MJ, et al. Enhancement of fatigue and corrosion properties of pure Ti by sandblasting. Mater Sci Eng A 2006;429:30–5.

[52] Todaka Y, Umemoto M, Tsuchiya K. Comparison of Nanocrystalline Surface Layer in Steels Formed by Air Blast and Ultrasonic Shot Peening. Mater Trans 2004;45:376–9.

[53] Umemoto M, Todaka Y, Tsuchiya K. Formation of nanocrystalline structure in steels by air blast shot peening. Mater Trans 2003;44:1488–93.

[54] Umemoto M. Nanocrystallization of Steels by Severe Plastic Deformation. Mater Trans 2003;44:1900–11.

[55] Todaka Y, Umemoto M, Watanabe Y, Yamazaki A, Wang C, Tsuchiya K. Formation of surface nanocrystalline structure in steels by shot peening and role of strain gradient on grain refinement by deformation. ISIJ Int 2007;47:157–62.

[56] Liu JL, Umemoto M, Todaka Y, Tsuchiya K. Formation of a nanocrystalline surface layer on steels by air blast shot peening. J Mater Sci 2007;42:7716–20.

[57] Tao NR, Wang ZB, Tong WP, Sui ML, Lu J, Lu K. An investigation of surface nanocrystallization mechanism in Fe induced by surface mechanical attrition treatment. Acta Mater 2002;50:4603–16.

[58] Liu G, Wang SC, Lou XF, Lu J, Lu K. Low carbon steel with nanostructured surface layer induced by high-energy shot peening. Scr Mater 2001;44:1791–5.

[59] Wang ZB, Tao NR, Li S, Wang W, Liu G, Lu J, et al. Effect of surface nanocrystallization on friction and wear properties in low carbon steel. Mater Sci Eng A 2003;352:144–9.

[60] Li D, Chen HN, Xu H. The effect of nanostructured surface layer on the fatigue behaviors of a carbon steel. Appl Surf Sci 2009;255:3811–6.

[61] Liu G, Lu J, Lu K. Surface nanocrystallization of 316L stainless steel induced by ultrasonic shot peening. Mater Sci Eng A 2000;286:91–5.

[62] Zhang HW, Hei ZK, Liu G, Lu J, Lu K. Formation of nanostructured surface layer on AISI 304 stainless steel by means of surface mechanical attrition treatment. Acta Mater 2003;51:1871–81.

[63] Tao N, Zhang H, Lu J, Lu K. Development of Nanostructures in Metallic Materials with Low Stacking Fault Energies during Surface Mechanical Attrition Treatment (SMAT). Mater Trans 2003;44:1919–25.

[64] Lin Y, Lu J, Wang L, Xu T, Xue Q. Surface nanocrystallization by surface mechanical attrition treatment and its effect on structure and properties of plasma nitrided AISI 321 stainless steel. Acta Mater 2006;54:5599–605.

[65] Wang K, Tao NR, Liu G, Lu J, Lu K. Plastic strain-induced grain refinement at the nanometer scale in copper. Acta Mater 2006;54:5281–91.

[66] Wu X, Tao N, Hong Y, Xu B, Lu J, Lu K. Microstructure and evolution of mechanically-induced ultrafine grain in surface layer of AL-alloy subjected to USSP. Acta Mater 2002;50:2075–84.

[67] Lu K, Lu J. Nanostructured surface layer on metallic materials induced by surface mechanical attrition treatment. Mater Sci Eng A 2004;375-377:38–45.

[68] Lu JZ, Luo KY, Zhang YK, Sun GF, Gu YY, Zhou JZ, et al. Grain refinement mechanism of multiple laser shock processing impacts on ANSI 304 stainless steel. Acta Mater 2010;58:5354–62.

[69] Li JG, Umemoto M, Todaka Y, Tsuchiya K. Role of strain gradient on the formation of nanocrystalline structure produced by severe plastic deformation. J Alloys Compd 2007;434-435:290–3.

[70] ASM Handbook Volume 04: Heat Treating. ASM International; 1991.

[71] Pye D. Practical Nitriding and Ferritic Nitrocarburizing. ASM International; 2003.

[72] Freddi A, Veschi D, Bandini M, Giovani G. Design of experiments to investigate residual stresses and fatigue life improvement by a surface treatment. Fatigue Fract Eng Mater Struct 1997;20:1147–57.

[73] Croccolo D, Cristofolini L, Bandini M, Freddi A. Fatigue strength of shot-peened nitrided steel: Optimization of process parameters by means of design of the experiment. Fatigue Fract Eng Mater Struct 2002;25:695–707.

[74] Gao YK. Influence of deep-nitriding and shot peening on rolling contact fatigue performance of 32Cr3MoVA steel. J Mater Eng Perform 2008;17:455–9.

[75] Batista AC, Dias AM, Lebrun JL, Le Flour JC, Inglebert G. Contact fatigue of automotive gears: Evolution and effects of residual stresses introduced by surface treatments. Fatigue Fract Eng Mater Struct 2000;23:217–28.

[76] Ohue Y, Matsumoto K. Sliding-rolling contact fatigue and wear of maraging steel roller with ion-nitriding and fine particle shot-peening. Wear 2007;263:782–9.

[77] Terres MA, Laalai N, Sidhom H. Effect of nitriding and shot-peening on the fatigue behavior of 42CrMo4 steel: Experimental analysis and predictive approach. Mater Des 2012;35:741–8.

[78] Ferkel H, Glatzer M, Estrin Y, Valiev RZ. RF plasma nitriding of a severely deformed high alloyed steel. Scr Mater 2002;46:623–8.

[79] Ji SJ, Wang L, Sun JC, Hei ZK. The effects of severe surface deformation on plasma nitriding of austenitic stainless steel. Surf Coatings Technol 2005;195:81–4.

[80] Shen L, Wang L, Wang Y, Wang C. Plasma nitriding of AISI 304 austenitic stainless steel with pre-shot peening. Surf Coatings Technol 2010;204:3222–7.

[81] Hashemi B, Rezaee Yazdi M, Azar V. The wear and corrosion resistance of shot peened-nitrided 316L austenitic stainless steel. Mater Des 2011;32:3287–92.

[82] Tong WP, Tao NR, Wang ZB, Lu J, Lu K. Nitriding iron at lower temperatures. Science (80-) 2003;299:686–8.

[83] Tong WP, Liu CZ, Wang W, Tao NR, Wang ZB, Zuo L, et al. Gaseous nitriding of iron with a nanostructured surface layer. Scr Mater 2007;57:533–6.

[84] Kikuchi S, Nakahara Y, Komotori J. Fatigue properties of gas nitrided austenitic stainless steel pre-treated with fine particle peening. Int J Fatigue 2010;32:403–10.

[85] SAE Manual on Shot Peening. Warrendale: 2001.

[86] Vander Voort GF. Metallography, Principles and Practice. ASM International; 1984.

[87] Walton WH. Feret's statistical diameter as a measure of particle size [2]. Nature 1948;162:329–30.

[88] Prevey P. X-RAY DIFFRACTION RESIDUAL STRESS TECHNIQUES. 1986.

[89] http://www.mahr.de (last accessed Oct. 2012) n.d.

[90] ISO 4278. Geometrical product specifications (GPS) – surface texture: profile method- terms, definitions and surface texture parameters. 1st ed.; 1997. n.d.

[91] Sinclair G, Dolan T. Effect of Stress Amplitude on Statistical Variability in Fatigue Life of 75S-T6 Aluminum Alloy. Trans Am Soc Mech Eng 1953;75:867–72.

[92] Sobczyk K, Spencer BFJ. Random fatigue: from data to theory. Academic Press, Incorporated; 1992.

[93] WJ D, Mood A. A Method for Obtaining and Analyzing Sensitivity Data. J Am Stat Assoc 1948;43:109–26.

[94] Dixon W. The Up-and-Down Method for Small Samples. J Am Stat Assoc 1965;60:967–78.

[95] Little R. Estimating the Median Fatigue Limit for Very Small Up-and-Down Quantal Response Tests and for S-N Data with Runouts. ASTM Spec Tech Publ 1971:29–42.

[96] Little R, Jebe E. Statistical Design of Fatigue Experiments. New York: John Wiley & Sons; 1975.

[97] Al-Hassani STS. Mechanical aspect of residual stress development in shot peening. first Int. Conf. shot Peen. ICSP1, Paris: 1981, p. 14–7.

[98] Al-Obaid YF. Rudimentary analysis of improving fatigue life of metals by shot-peening. J Appl Mech Trans ASME 1990;57:307–12.

[99] Al-Obaid YF. Shot peening mechanics: experimental and theoretical analysis. Mech Mater 1995;19:251–60.

[100] Kobayashi M, Matsui T, Murakami Y. Mechanism of creation of compressive residual stress by shot peening. Int J Fatigue 1998;20:351–7.

[101] Meguid SA, Shagal G, Stranart JC. Finite element modelling of shot-peening residual stresses. J Mater Process Technol 1999;92-93:401–4.

[102] Schiffner K, Droste Gen. Helling C. Simulation of residual stresses by shot peening. Comput Struct 1999;72:329–40.

[103] Meo M, Vignjevic R. Finite element analysis of residual stress induced by shot peening process. Adv Eng Softw 2003;34:569–75.

[104] Frija M, Hassine T, Fathallah R, Bouraoui C, Dogui A. Finite element modelling of shot peening process: Prediction of the compressive residual stresses, the plastic deformations and the surface integrity. Mater Sci Eng A 2006;426:173–80.

[105] Hong T, Ooi JY, Shaw BA. A numerical study of the residual stress pattern from single shot impacting on a metallic component. Adv Eng Softw 2008;39:743–56.

[106] Hong T, Ooi JY, Shaw B. A numerical simulation to relate the shot peening parameters to the induced residual stresses. Eng Fail Anal 2008;15:1097–110.

[107] Meguid SA, Shagal G, Stranart JC, Daly J. Three-dimensional dynamic finite element analysis of shot-peening induced residual stresses. Finite Elem Anal Des 1999;31:179–91.

[108] Meguid SA, Shagal G, Stranart JC. 3D FE analysis of peening of strain-rate sensitive materials using multiple impingement model. Int J Impact Eng 2002;27:119–34.

[109] Kim T, Lee JH, Lee H, Cheong S -k. An area-average approach to peening residual stress under multi-impacts using a three-dimensional symmetry-cell finite element model with plastic shots. Mater Des 2010;31:50–9.

[110] Majzoobi GH, Azizi R, Alavi Nia A. A three-dimensional simulation of shot peening process using multiple shot impacts. J Mater Process Technol 2005;164-165:1226–34.

[111] Miao HY, Larose S, Perron C, Lévesque M. On the potential applications of a 3D random finite element model for the simulation of shot peening. Adv Eng Softw 2009;40:1023–38.

[112] Gangaraj SMH, Guagliano M, Farrahi GH. An approach to relate shot peening finite element simulation to the actual coverage. Surf Coatings Technol 2012.

[113] Dassault Systemes, ABAQUS 6.10-1 User's manual. 2010.

[114] Johnson GR, Cook WH. Fracture characteristics of three metals subjected to various strains, strain rates, temperatures and pressures. Eng Fract Mech 1985;21:31–48.

[115] Estrin Y, Vinogradov A. Extreme grain refinement by severe plastic deformation: A wealth of challenging science. Acta Mater 2013;61:782–817.

[116] Kocks UF. LAWS FOR WORK-HARDENING AND LOW-TEMPERATURE CREEP. J Eng Mater Technol Trans ASME 1976;98 Ser H:76–85.

[117] Mecking H, Kocks UF. Kinetics of flow and strain-hardening. Acta Metall 1981;29:1865–75.

[118] Zehetbauer M, Seumer V. Cold work hardening in stages IV and V of F.C.C. metals-I. Experiments and interpretation. Acta Metall Mater 1993;41:577–88.

[119] Mughrabi H. Dislocation wall and cell structures and long-range internal stresses in deformed metal crystals. Acta Metall 1983;31:1367–79.

[120] Prinz FB, Argon AS. The evolution of plastic resistance in large strain plastic flow of single phase subgrain forming metals. Acta Metall 1984;32:1021–8.

[121] Nix WD, Gibeling JC, Hughes DA. Time-dependent deformation of metals. Metall Trans A 1985;16:2215–26.

[122] Estrin Y, Tóth LS, Molinari A, Bréchet Y. A dislocation-based model for all hardening stages in large strain deformation. Acta Mater 1998;46:5509–22.

[123] Tóth LS, Molinari A, Estrin Y. Strain hardening at large strains as predicted by dislocation based polycrystal plasticity model. J Eng Mater Technol Trans ASME 2002;124:71–7.

[124] Holt DL. Dislocation cell formation in metals. J Appl Phys 1970;41:3197–201.

[125] Baik SC, Estrin Y, Kim HS, Hellmig RJ. Dislocation density-based modeling of deformation behavior of aluminium under equal channel angular pressing. Mater Sci Eng A 2003;351:86–97.

[126] Lemiale V, Estrin Y, Kim HS, O'Donnell R. Grain refinement under high strain rate impact: A numerical approach. Comput Mater Sci 2010;48:124–32.

[127] McKenzie PWJ, Lapovok R, Estrin Y. The influence of back pressure on ECAP processed AA 6016: Modeling and experiment. Acta Mater 2007;55:2985–93.

[128] Lapovok R, Dalla Torre FH, Sandlin J, Davies CHJ, Pereloma E V, Thomson PF, et al. Gradient plasticity constitutive model reflecting the ultrafine micro-structure scale: The case of severely deformed copper. J Mech Phys Solids 2005;53:729–47.

[129] Estrin Y, Molotnikov A, Davies CHJ, Lapovok R. Strain gradient plasticity modelling of high-pressure torsion. J Mech Phys Solids 2008;56:1186–202.

[130] Johnson K. Contact Mechanics. Cambridge University Press; 1987.

[131] Li JK, Mei Y, Duo W, Renzhi W. Mechanical approach to the residual stress field induced by shot peening. Mater Sci Eng A 1991;147:167–73.

[132] Dai K, Shaw L. Comparison between shot peening and surface nanocrystallization and hardening processes. Mater Sci Eng A 2007;463:46–53.

[133] Takaki S. Limit of dislocation density and ultra-grain-refining on severe deformation in iron. Mater Sci Forum 2003;426-432:215–22.

[134] Kwon H, Kim CM, Lee KB, Yang HR, Lee JH. Effect of alloying additions on secondary hardening behavior of Mo-containing steels. Metall Mater Trans A Phys Metall Mater Sci 1997;28 A:621–7.

[135] Hassani-Gangaraj SM, Guagliano M. Microstructural evolution during nitriding, finite element simulation and experimental assessment. Appl Surf Sci 2013;271:156–63.

[136] UNI 11153-2, Measurement of thickness of hardened surface layers on ferrous parts, Nitriding and ferritic nitrocarburizing 2006.

[137] Ashrafizadeh F. Influence of plasma and gas nitriding on fatigue resistance of plain carbon (Ck45) steel. Surf Coatings Technol 2003;174-175:1196–200.

[138] Bell T, Loh NL. The fatigue characteristics of Plasma Nitrided three Pct Cr-Mo steel. J Mater Eng Perform 1982;2:232–7.

[139] Farrahi GH LJ. Surface hardness measurement and micro-structural characterisation of steel by X-ray diffraction profile analysis. J Eng 1995;8:159–67.

[140] Guagliano M, Vergani L. Effect of nitriding on low-cycle fatigue properties. Int J Fatigue 1997;19:67–73.

[141] Limodin N, Verreman Y, Tarfa TN. Axial fatigue of a gas-nitrided quenched and tempered AISI 4140 steel: Effect of nitriding depth. Fatigue Fract Eng Mater Struct 2003;26:811–20.

[142] Hussain K, Tauqir A, Ul Haq A, Khan AQ. Influence of gas nitriding on fatigue resistance of maraging steel. Int J Fatigue 1999;21:163–8.

[143] Komotori J, Shimizu M, Misaka Y, Kawasaki K. Fatigue strength and fracture mechanism of steel modified by super-rapid induction heating and quenching. Int J Fatigue 2001;23:S225–S230.

[144] De La Cruz P, Odén M, Ericsson T. Effect of laser hardening on the fatigue strength and fracture of a B-Mn steel. Int J Fatigue 1998;20:389–98.

[145] Kloos K, Velten E. No Title. Konstruction 1984;36:181–8.

[146] Li CX, Sun Y, Bell T. Shot peening of plasma nitrided steel for fretting fatigue strength enhancement. Mater Sci Technol 2000;16:1067–72.

[147] Genel K, Demirkol M, Çapa M. Effect of ion nitriding on fatigue behaviour of AISI 4140 steel. Mater Sci Eng A 2000;279:207–16.

[148] Corredor LH, Chornik B, Ishizaki K. Correlation study of hardness and nitrogen concentration in nitrided steel by Auger electron spectroscopy. Scr Metall 1981;15:195–9.

[149] Alphonsa I, Chainani A, Raole PM, Ganguli B, John PI. A study of martensitic stainless steel AISI 420 modified using plasma nitriding. Surf Coatings Technol 2002;150:263–8.

[150] Zagonel LF, Figueroa CA, Droppa Jr. R, Alvarez F. Influence of the process temperature on the steel microstructure and hardening in pulsed plasma nitriding. Surf Coatings Technol 2006;201:452–7.